DEPARTMENT OF OPTOELECTRONICS

University of Ulm

Oberer Eselsberg
D-89069 Ulm, Germany

Phone : 0049-(0)731 / 502 60 50
Facsimile: 0049-(0)731 / 502 60 49

ANNUAL REPORT 1995

Contents

From the Editor

With this annual report, the Department of Optoelectronics at the University of Ulm gives an overwiew of its research activies. The opening article *Continuing Progress* characterizes the work at the Department over the last year.

The annual report consists of 19 articles followed by a list of Ph.D. and diploma theses, publications, talks and conference contributions in 1995.

I like to thank Dr. Jürgen Mähnß for writing a LaTeX style which allowed simple handling of graphics for this report. Additionally, I want to thank Prof. Dr. Peter Unger who thoroughly refereed the manuscript and in so doing contributed to its final form. Also I like to thank all the authors who contributed their work to the report.

Finally, I wish to all my colleagues a successful and fruitful work in the year 1996.

Arthur Pelzmann

Continuing Progress

The year 1995 was another successful one for the Department of Optoelectronics. Research concentrated in the four main areas: vertical-cavity surface-emitting laser diodes (VCSELs), optical interconnect systems, wide bandgap semiconductors and high power laser diodes. Outstanding results were obtained in the VCSEL group, where 47 % electrical-to-optical conversion efficiency, more than 50 mW maximum cw output power and laser operation from -90 °C to 120 °C were demonstrated. The systems group for the first time world-wide applied VCSELs for transmission in optical interconnects at data rates of 10 Gbit/s. The wide-bandgap semiconductor group now existing for about one year has produced state-of-the-art GaN using both gas-source molecular beam epitaxy (GSMBE) or newly-installed metal-organic vapor-phase epitaxy (MOVPE). The high power laser diode group has made steady progress in improving device performance now achieving more than 1 Watt cw output power in non heat sinked devices.

During spring, Prof. Kowalsky's former group (mainly involved in organic semiconductors) finally moved to Braunschweig. Meanwhile, this severe loss has been more than compensated by the nice activities in high-power lasers, nanolithography, and dry etching by Peter Unger who in his second year in the Department not only was extremely active in research but also introduced a very popular course on nanostructures and technology. In October, Torsten Wipiejweski rejoined the Department after a two-year postdoc time at the University of California, Santa Barbara. He is going to strengthen the activities in long-wavelength VCSELs and wafer fusion. The textbook K.J. Ebeling, Integrated Optoelectronics, Springer 1993, was newly listed in the distinguished Book Club of the Optical Society of America.

In total, there have been 15 semester theses and 18 diploma theses completed in 1995 in the Department. Four members of the Department, Eberhard Zeeb, Bernd Moeller, Andreas Fricke, and Christoph Rompf received their Ph.D. degrees and now hold attractive positions in industry or as in the case of Christoph are in a postdoc position at the Technical University of Braunschweig. The 13 reasearch projects of the Department are generously supported by the German Science Foundation, the Federal Ministery for Research and Technology, the ACTs Program of the European Community, the NEDO Program of the Japanese Ministery of International Trade and Industry, the Volkswagenstiftung, German Telekom and Daimler-Benz Research, which is gratefully acknowledged. Summaries of the activities are found in the following articles.

The year 1995 has been an evolutionary period for the Department with some important extensions in the areas of high-power laser diodes and GaN based devices. The Head of the Department has finished his duties as the Dean of the Faculty of Electrical Engineering but has been elected to now serve as the Vice-President of the University responsible for research. The Department is looking forward to an exciting year 1996.

Karl Joachim Ebeling
Ulm, January 1996

Digital Video Transmission Using Top-Emitting VCSELs

Peter Schnitzer

Digital video transmission is a suitable application for VCSELs. Data rates of up to 270 Mbit/s per channel require high-speed transmitters with low bit error rates. Though there are no cheap digital video components available yet, the digital era has already begun with the Astra 1E satellite being in service for several months now.

1. Introduction

Ever since television was invented television signals have been broadcasted in composite analogue form. When color TV was first introduced, the need to retain compatibility with monochrome TV sets led to encoding the color information into a composite signal. Though it was recognized that encoding and decoding reduce the picture quality, these were negligible compared to transmission errors in these pioneer years of television. More recently, some TV stations have upgraded their equipment to use component analogue signals in order to achieve higher picture quality. In particular, this is very important to realize noise-free multigeneration recording. Therefore, the 4:2:2 component signal has been chosen for several digital formats such as D-1.

2. Digital Video Formats

Name	Type	Tape	Bits	Comments
D-1	Component 4:2:2	3/4" (19 mm)	8 - 10	High end post Cost prohibitive
D-2	Composite $4f_{sc}$	3/4" (19 mm)	8	Broadcast workhorse
D-3	Composite $4f_{sc}$	1/2" (13 mm)	8	Answer to D-2

Table 1: Established DVTR formats [1].

Digital TV signals demand digital video tape recorders (DVTR). The first commercially available DVTRs recorded 8-bit component 4:2:2 signals [1], and the format became known as D-1. The outstanding advantage of the D-1 format is, that it uses the same 13.5-MHz sampling frequency for both 525- and 625-line television signals. This does not mean that a signal that has been recorded on one standard may be played back on the other, but that the hardware is identical for both. The composite based digital formats such as D-2 and D-3 have chosen $4f_{sc}$ (4 times the subcarrier) signals and require different hardware for 525- and 625-signals. Sometimes the hardware compatibility is less important than inexpensively noise-free multigeneration recording. Therefore, the D-2 and D-3 standards have been established. An overview of these standards is given in Tab. 1. About two years ago some other less expensive standards were introduced

into the marketplace - DCT, Digital Betacam and D-5. All are component DVTRs. DCT and Digital Betacam use compression, while D-5 uses no compression and is compatibel with D-3. None of these new tape formats are compatible with each other as can be seen in Tab. 2.

Name	Type	Tape	Bits	Comments
DCT	Component 4:2:2	3/4" (19 mm)	8	Uses compression
Digital Betacam	Component 4:2:2	1/2" (13 mm)	10	Some models play Betacam Uses compression
D-5	Component 4:2:2	1/2" (13 mm)	10	Compatible with D-3 No compression

Table 2: New DVTR formats [1].

3. Signal Formats

When a signal is sampled at 4:2:2, a 10-bit word (1024 levels) is written by taking a sample across all three channels Y, R-Y, B-Y or Y, U, V [1]. This is called a co-sited sample and is referred as Y, Cr, Cb. A sample of the Y channel alone is then taken and then another co-sited sample, and so on, alternating between Y and Y, Cr, Cb. These samples are taken at a frequency of 13.5 MHz for the Y channel and 6.75 MHz for the color-difference channels R-Y and B-Y. When multiplexed, the resultant sample frequency is 27 MHz. When a signal is sampled at $4f_{sc}$, a 10-bit word is written at a rate of 14.3 MHz in NTSC and 17.73 MHz in PAL [2]. The entire signal is sampled, including the horizontal and vertical blanking intervals, containing sync pulses and the color burst. Tab. 3 shows the parallel clock rates and serial data rates of the different formats.

Format	Parallel Clock Rate	Serial Data Rate
$4f_{sc} - NTSC$	14.3 MHz	143 Mbit/s
$4f_{sc} - PAL$	17.7 MHz	177 Mbit/s
4:2:2	27 MHz	270 Mbit/s

Table 3: Sampling and serial rates [1].

4. Experimental Setup

In order to demonstrate the capability of surface emitters we have chosen the studio quality D-1 standard demanding the highest data rate of 270 Mbit/s. The experimental setup of the transmission line is illustrated in Fig. 1. Since there are no cheap digital video sources available yet, we use a common VTR which delievers a FBAS signal. A converter is used to transform this composite signal to a component YUV signal that is fed to an A/D converter and then multiplexed. The biased laser is modulated with the resultant D-1 signal shown in Fig. 2. The surface emitter is butt coupled to a multi-mode fiber while a coupling efficiency of 90% can be

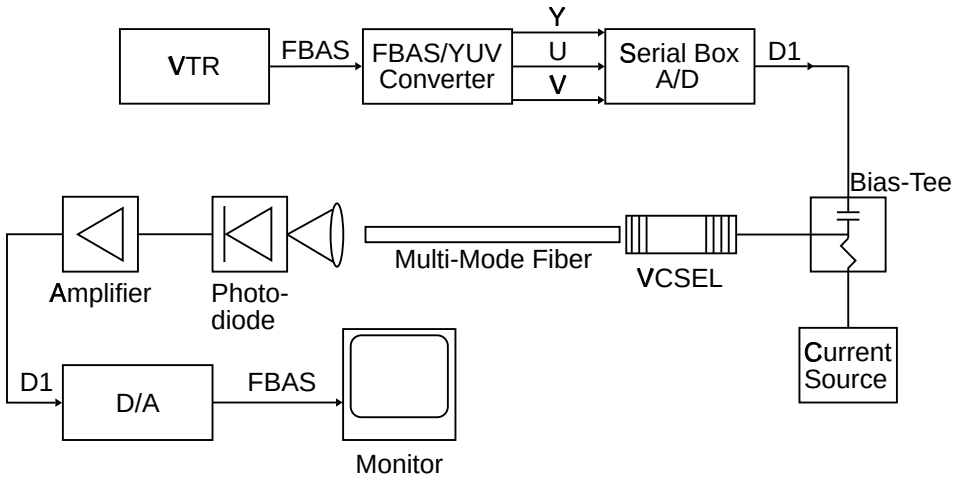

Fig. 1: Experimental setup.

achieved [3]. The optical D-1 signal is detected with a Si-APD then amplified and fed to a demultiplexer. A D/A converter transforms the incoming digital signal to an analogue composite FBAS signal again. Finally, this FBAS signal is displayed on a common video monitor.

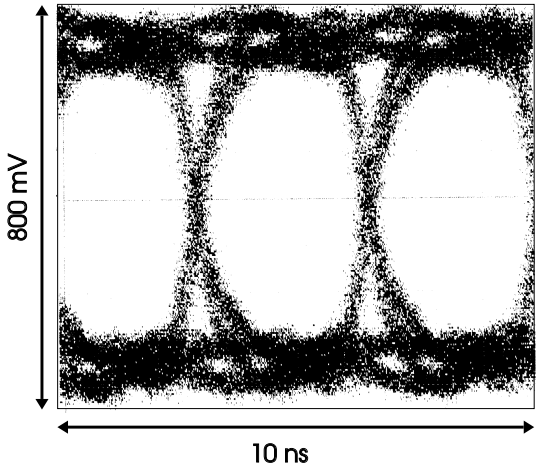

Fig. 2: Eye diagram of the electrical D-1 signal the surface emitter is modulated with.

5. Outlook

According to the 10 Gbit/s data transmission at a bit error rate of less than 10^{-11} demonstrated earlier [4], vertical-cavity lasers are suitable for fiber-based digital video broadcasting. Theoretically, a VCSEL can simultanously transmit up to 37 D-1 channels or, even more impressive, up to 156,250 64 kbit/s ISDN channels for video conferences [5]. It has yet to be shown what bit error rate is acceptable for practically error-free digital video transmission.

References

[1] D. Strachan, R. Conrod, M. Proulx, "Serial Video Basics," *SMPTE Journal*, pp. 254-257, May 1995.

[2] B. Tichit, "Mehrjährige Erfahrungen mit seriell-digitaler Fernsehtechnik," *Fernseh- und Kinotechnik*, Nr. 4, pp. 248-253, 1993.

[3] U. Fiedler, K.J. Ebeling, "Design of VCSEL's for Feedback Insensitive Data Transmission and External Cavity Active Mode-Locking," *IEEE Journal of Selected Topics in Quantum Electronics*, vol. 1, no. 2, pp. 442-450, June 1995.

[4] U. Fiedler, B. Möller, G. Reiner, P. Schnitzer and K.J. Ebeling, "10 Gbit/s data transmission using top emitting VCSELs with high sidemode suppression," *Electronics Letters*, vol. 31 no. 19, pp. 1664-1665, September 1995.

[5] U. Reimers, "Digitale Fernsehtechnik," *Springer Verlag*, pp. 68-73, 1995.

Delayed Self-Heterodyne Linewidth Measurement of Vertical-Cavity Surface-Emitting Laser Diodes

Christian Jung, Wolfgang Schmid

The linewidth measurement of VCSELs using an heterodyne detection system is presented. The minimum linewidth without any optical feedback is as narrow as 35 MHz. A linewidth power product of 14 mW·MHz is obtained. The measured linewidth enhancement factor is α_H = -5.

1. Introduction

Vertical-cavity surface-emitting-laserdiodes (VCSEL) with a low linewidth of about 30 MHz [1] and an α_H parameter of -3.7 [3] have been fabricated. In the measurement, a grating spectrometer and a scanning Fabry-Perot interferometer are used for the optical spectrum analysis. The typical resolution limits are 10 GHz and 10 MHz in the visible and near infrared wavelength regions, respectively. An alternative method to measure the field spectrum of a laser diode is to use a heterodyne detection system. In such a system, the light of the laser under test is frequency mixed with a local oscillator light. The optical frequency is down-converted to the intermediate frequency (IF). The maximum IF is limited by the receiver bandwidth. Moreover, the spectral width of the local oscillator must be much narrower than that of the laser under test. The spectral resolution limit is practically given by the spectral width of the local oscillator. However, it is rather difficult to prepare such a frequency-stabilized and spectrum-purified local oscillator. To overcome this difficulty, we use a technique, called delayed self-heterodyne method. It offers a resolution of 100 kHz without any difficulty.

2. Experimental Setup for Delayed Self-Heterodyne Method

The experimental setup to determine the linewidth of VCSEL is shown in Fig. 1. The laser diode is driven by a current source which is controlled to be better than 10 μA. The VCSEL is butt coupled to a 3-dB single-mode fiber directional coupler. The output from one arm is delayed by the time τ_d using a single-mode fiber of 1 km length. This offers a resolution of 150 kHz. Additional to time delay the light passes through a polarization converter and is frequency shifted by a $LiNbO_3$ phase modulator. The converter is necessary to polarize the light in z direction to achieve a maximum modulation. The output of the other arm only passes through a polarization converter. Both beams are then superimposed into another 3-dB coupler. One branch of the superimposed light reaches a grating spectrometer, where the spectrum without modulation is observed. The second branch is detected by a photo diode, amplified and then recorded by a RF spectrum analyzer. In the branch which includes the phase modulator and the single-mode fiber for delay time we can take losses of nearly 10 dB into account.

3. Theory

In this section, the spectrum of the heterodyne method is evaluated. For our calculation we neglect AM noise fluctuations and assume that both waves will have the same polarization. The

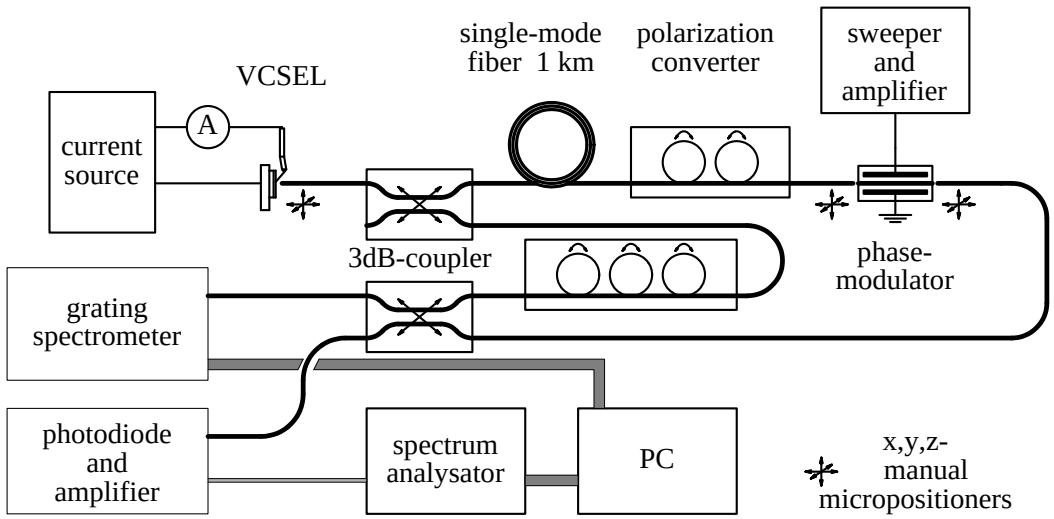

Fig. 1: Experimental setup for the linewidth measurement

electric field of the investigated laser can be written as $\mathbf{E_s} = \hat{\mathbf{E}}_\mathbf{s} \exp\{i[\omega_s t + \Phi_s(t)]\}$ and the local oscillator as $\mathbf{E_l} = \hat{\mathbf{E}}_\mathbf{l} \exp\{i[\omega_l t + \Phi_l(t)]\}$. The electric field of the superimposed waves then is $\mathbf{E} = \mathbf{E_s} + \mathbf{E_l}$. The current of the photodiode is proportionally to the square of the incident electrical field and can be expressed by

$$I_{Ph}(t) \sim \mathbf{E}\mathbf{E}^* = (\hat{\mathbf{E}}_s^2 + \hat{\mathbf{E}}_l^2) + 2\hat{\mathbf{E}}_s\hat{\mathbf{E}}_l \cos\{\Delta\omega t + [\Phi_s(t) - \Phi_l(t)]\} \ . \quad (1)$$

We see that Eq. (1) obtains the difference frequency (intermediate frequency IF) of both lasers. The autocorrelation function is

$$\mathcal{A}_{I_{Ph}} = \left[\hat{\mathbf{E}}_s^2 + \hat{\mathbf{E}}_l^2\right]^2 + 2\hat{\mathbf{E}}_s^2\hat{\mathbf{E}}_l^2 \cos\{\Delta\omega t\} \exp\left\{-\sigma^2\{\Phi(t)\}\right\} \ ,$$

where σ^2 represents the variance of the phase. Now we get the spectrum by calculating the Fourier transform of the autocorrelation function

$$\mathcal{S}_{I_{Ph}}(f) = \left[\hat{\mathbf{E}}_s^2 + \hat{\mathbf{E}}_l^2\right]^2 \delta(f) + \frac{\hat{\mathbf{E}}_s^2\hat{\mathbf{E}}_l^2}{\pi f_\Delta}\left[\frac{f_\Delta^2}{f_\Delta^2 + [f - \Delta f]^2} + \frac{f_\Delta^2}{f_\Delta^2 + [f + \Delta f]^2}\right] \ , \quad (2)$$

where f_Δ is the FWHM given by [2] and Δf is the intermediate frequency. Note that the obtained Lorentzian lineshape has a FWHM which is twice as large as that of the original laser. Since we use a delayed self-heterodyne method, the frequency of one beam has to be shifted to the wanted intermediate frequency. For this case we obtain the spectrum as

$$\mathcal{S}_{I_{Ph}}(f) = \left[\hat{\mathbf{E}}_s^2 + \hat{\mathbf{E}}_l^2\right]^2 \delta(f) + \frac{2\hat{\mathbf{E}}_s^2\hat{\mathbf{E}}_l^2}{\pi f_\Delta} \sum_{j=-\infty}^{\infty} \frac{J_j^2(\mu)}{1 + \left[\frac{f - j f_m}{f_\Delta}\right]^2} \ , \quad (3)$$

where J is the Bessel function, f_m the modulation frequency and μ the modulation index. The spectrum repeats with the modulation frequency f_m, the amplitude is given by the Bessel

functions. To avoid an overlap between the individual Lorentzian lineshapes, the modulation frequency has to be twice as large as the linewidth.

4. Results

Fig. 2 shows a typical light versus current characteristic of a proton implanted laser structure of 16 μm active diameter, which has been investigated. The threshold current is 2.3 mA corresponding to a threshold current density of $j = 1$ kA/cm^2. The maximum output power is 1 mW and is only restricted by the thermal roll over.

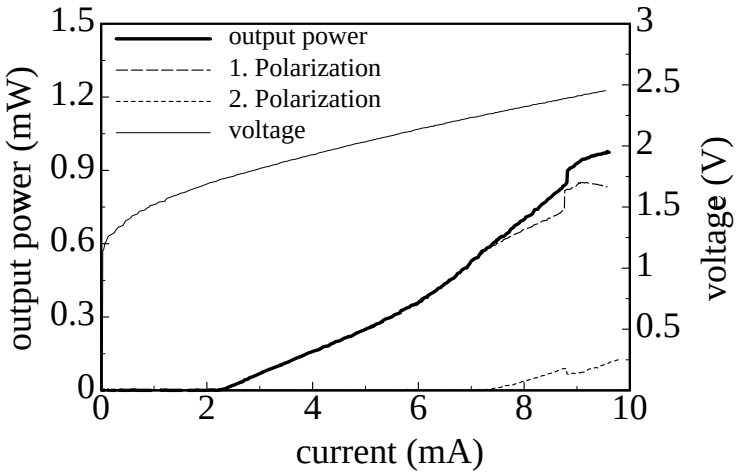

Fig. 2: Light output and driving voltage characteristics of a laser with 16 μm active region

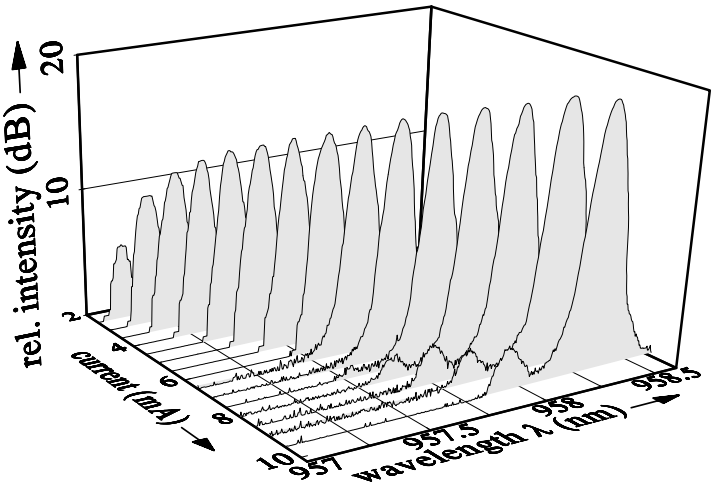

Fig. 3: Logarithmic spectra of 16 μm laser for different driving currents

In a wide range to 7 mA the laser only oscillates in one polarization. The logarithmic spectra for different currents are depicted in Fig. 3. The emission at a wavelength of about 957.1 nm occurs in a single longitudinal and transverse mode up to a current of 7 mA.

Higher-order transverse modes in the spectrum appear at 7.4 mA. The mode suppression of the next transverse-order mode is better than 20 dB. Fig. 4 shows the recorded linewidth as a function of the inverse output power. The experimental data for all measured linewidths are very well approximated by a linear regression curve resulting in a linewidth power product of 14 mW·MHz. For infinte output the residual linewidth reaches 4 MHz.

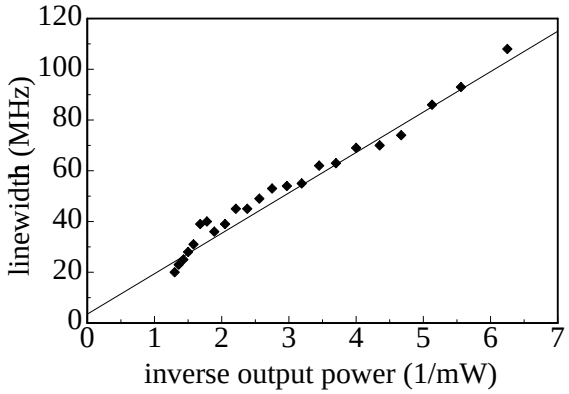

Fig. 4: Linewidth as a function of inverse output power. The residual linewidth is 4 MHz

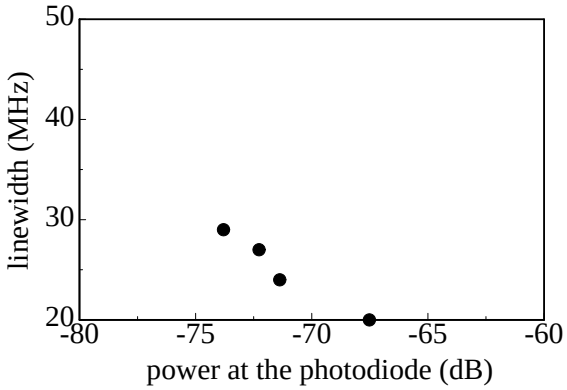

Fig. 5: Linewidth in dependence of the feedback level

Due to the fact that no isolator is used we have to regard optical feedback effects of the VCSEL. The linewidth in dependence of the feedback level at the photo diode is depicted in Fig. 5. To investigate the influence of the feedback, we vary the spacing between fiber and VCSEL to control the insertion loss. For 67 dB feedback, we obtain a very low linewidth of 20 MHz. The linewidth without any feedback can be approximated with a upper limit of nearly 35 MHz.

Since we obtain a very narrow linewidth it is interesting to investigate the corresponding α_H factor. The α_H parameter can be obtained as [4]

$$\alpha_H = -\frac{2\hat{\beta}}{m}\,, \tag{4}$$

from the frequency and intensity modulation indices $\hat{\beta}$ and m, respectively. The experimental setup for the measurement of the linewidth enhancement factor is described in [3].

A typical optical spectrum recorded with a confocal scanning Fabry-Perot interferometer is depicted in Fig. 6. The laser has been biased at a current of 5 mA and modulated with a modulation depth of $m = 0.38$ at a frequency of 1.5 GHz. The frequency modulation index $\hat{\beta}$ is numerically evaluated from the relative sideband strenghts [4]. A α_H parameter of -5 is determined, the sign is calulated from the asymmetric sidebands, which occurs at a frequency of 0.5 GHz [5].

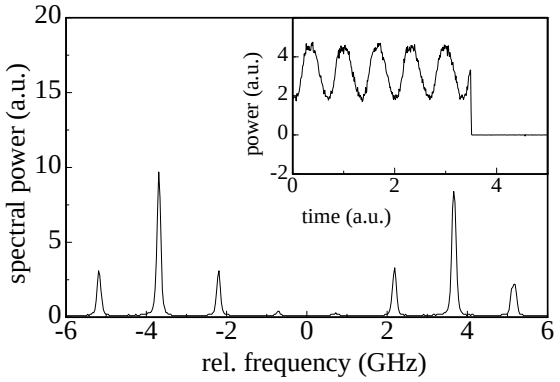

Fig. 6: Measured optical spectrum with an intensity modulation index $m = 0.38$ and a modulation frequency of 1.5 GHz. From the inset the modulation index m is obtained

5. Summary

The linewidth measurement of VCSELs using a delayed self-heterodyne method has been shown. Extremely low linewidths of less than 35 MHz have been observed. The setup allows to determine the linewidth with less sensitivity against vibrations and an easier adjustment than using a scanning Fabry-Perot interferometer. In the future a fiber isolator must be used to avoid optical feedback effects. Instead using a $LiNbO_3$ phase modulator, an acoustic optical modulator (AOM) with a modulation frequency of 80 MHz should be used. Future work will be devoted to investigations of highly-efficient selectively-oxidized single-mode VCSELs.

References

[1] E. Zeeb, G. Reiner, M. Ries, B. Möller and K.J. Ebeling, "VCSELs with Extremely Low Linewidth and Linewidth Power Product," in Proc. *Conf. on Lasers and Electro-Optics (CLEO)*, p. 171, Baltimore, MD, USA, May 1995.

[2] C.H. Henry, "Theory of the Linewidth of Semiconductor Lasers," *IEEE J. Quantum Electron.*, vol. QE-18, no. 2, pp. 259-264, 1982.

[3] B. Möller, E. Zeeb, T. Hackbarth, K.J. Ebeling, "Linewidth Enhancement Factor of Vertical-Cavity Surface-Emitting Laser Diodes," *IEEE Photonics Technol. Lett.*, vol. 6, pp. 921-923, 1994.

[4] C. Harder, K. Vahala and Amnon Yariv, "Measurement of the Linewidth Enhancement Factor α of Semiconductor Lasers," *Appl. Phys. Lett.*, vol. 42, no. 4, pp. 328-330, February 1983.

[5] W. Schmid, "Messung der Linienbreite vertikal emittierender Laserdioden im Heterodyn-Übertragungsverfahren," *Diploma Thesis*, p. 55, November 1995.

10 Gbit/s Data Transmission Using Top Surface-Emitting Vertical-Cavity Laser Diodes

Ulrich Fiedler, Peter Schnitzer

Intensity modulated proton-implanted top surface-emitting vertical-cavity lasers (VCSELs) with a small signal modulation bandwidth of 12 GHz butt-coupled to multi-mode fibers are investigated as light source for optical interconnection. At 10 Gbit/s pseudo random data rates, the bit error rate (BER) remains under 10^{-11} *after transmission over 500 m of graded-index multi-mode fiber. Optimum transmission behavior is achieved for linearly polarized nearly single-mode laser operation with a side-mode suppression of better than 25 dB under modulation. Spectral characterization indicates that linearly polarized single-mode light output is essential for good BER performance.*

1. Introduction

Performance of short wavelength (λ=850/980 nm) proton implanted vertical-cavity surface-emitting lasers (VCSELs) has improved significantly in the past years such that these devices are now considered as transmitters for optical communication applications alternatively to in plane lasers [1]. The electrical problem of excessive voltage drop in the VCSEL Bragg reflectors and low conversion efficiency has been solved by using modulation and δ-doping at the heterointerfaces [2] and threshold voltages close to the bandgap voltage has been demonstrated by several groups [3,4]. At the present status, VCSELs are investigated as transmitters for short distant data links, board-to-board communication and optical interconnection. Properties such as formation of two-dimensional arrays [5], easy on-wafer testing and low-divergent light output perpendicular to the wafer allowing efficient fiber coupling [6] promise low-cost production. Additionally, bias-free modulation can be expected from oxidized VCSELs where high wall-plug efficiencies [7] and threshold currents below 10 μA have been demonstrated [8]. To achieve low-cost solutions, VCSEL transmitters will be installed with large-core plastic-clad fibers [9] or graded-index multi-mode fiber where transmission of 3 Gbit/s has been reported over 500 m length [10,11].

In this report we study the emission characteristics of VCSELs with 12 GHz optical modulation bandwidth. Transmission of 10 Gbit/s pseudo-random bit sequence (PRBS) data rates with a bit error rate of less than 10^{-11} is achieved for both back to back testing and transmission over 500 m of graded index multi-mode fiber.

2. Device Structure and Modulation Response

The VCSEL used for the transmission experiment is described in [2]. It is grown in $< 100 >$ direction and contains three 8 nm thick strained InGaAs quantum wells embedded in GaAs barriers surrounded by $Al_{0.35}Ga_{0.65}As$ layers for efficient carrier confinement. The active region is sandwiched between two Bragg reflectors where the bottom and the top reflector consists of 35.5 periods and 28 periods of $GaAs/Al_{0.7}Ga_{0.3}As$ layers, respectively. A TiPtAu top ring p-contact is used to achieve both, good ohmic contacts as well as light emission through the top Bragg reflector at 980 nm.

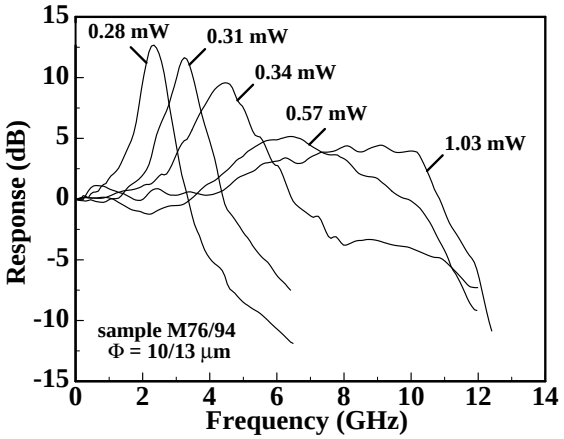

Fig. 1: Small signal frequency response of a 13 μm active diameter VCSEL with 10 μm emission window.

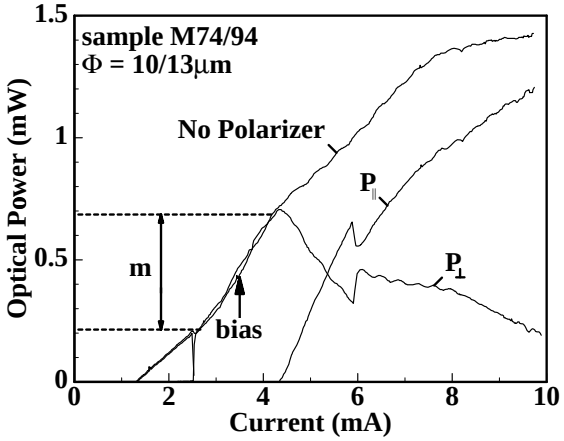

Fig. 2: Polarization resolved output characteristics of top emitting VCSELs with 10 μm diameter emission window and 13 μm active diameter. $P_\perp$ and $P_{||}$ denote orthogonal polarizations.

To measure the modulation characteristics free of parasitics laser diodes are processed in 250 μm pitch ground-signal configuration and contacted with microwave probes. The modulated light is detected with a 15 GHz bandwidth InGaAs pin photodiode and recorded with a RF spectrum analyzer. Fig. 1 depicts the measured small-signal amplitude modulation behavior of a laser diode with 13 μm active diameter and 10 μm emission window aperture. The modulation bandwidth increases with increasing driving current. The maximum electrical and optical bandwidth obtained at 1.03 mW optical output is 11.2 GHz and 12 GHz, respectively.

3. Emission Characteristics

Fig. 2 shows the polarization resolved output characteristics of the VCSEL with 13 μm active diameter and 10 μm emission window. Above the threshold current of 1.5 mA the laser oscillates in the linear polarization state $P_{||}$. At 2.6 mA polarization switching to the orthogonal eigenstate is observed which might be due to a change in crystallographic strain induced by the current. Since the frequency splitting of the nearly degenerate orthogonal eigenstates is less than the 0.1 nm resolution bandwidth of the grating spectrometer [12], the polarization modes are not resolved in the emission spectra depicted in Fig. 3. Above 4.3 mA the LP_{11} mode appears 0.3 nm blue shifted and orthogonally polarized to the fundamental LP_{01} mode. The power in the LP_{01} and the LP_{11} equal at approximately 6 mA where again a polarization mode transition occurs. A third transverse mode oscillates for currents higher than 8.4 mA.

4. Bit Error Rate Measurement

For high bit rate data transmission the VCSELs with short feeding lines and bondpads are connected to SMA sockets. The electrical 3 dB frequency of the packaged device is 9 GHz. Bias current and 10 Gbit/s PRBS are combined in a bias-tee. After transmission over 500 m of multi-mode fiber the signal is attenuated, and focused on a 15 GHz bandwidth InGaAs

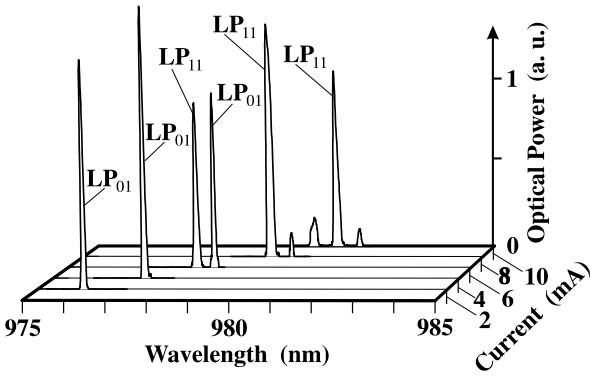

Fig. 3: Emission spectra of 10/13 μm VCSEL for various bias currents.

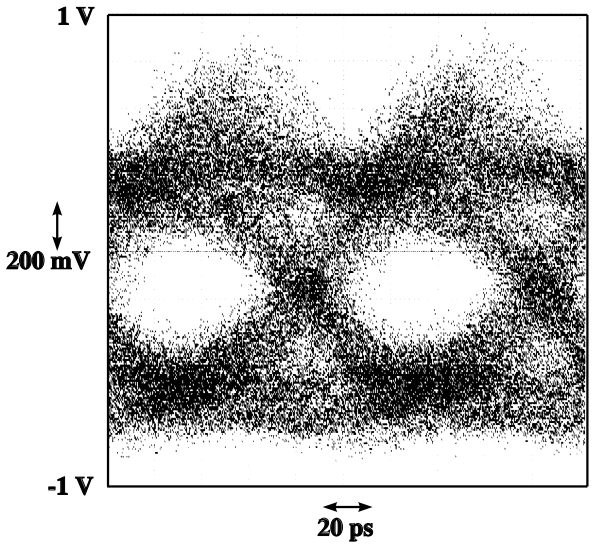

Fig. 4: Eye diagram at 10 Gbit/s PRBS modulation at a BER of 10^{-9}.

photodiode. Focal spot size is smaller than the active diameter of 50 μm of the photodiode such that modal noise is negligible. The electrical signal is amplified in two stages and fed to an electrical sampling oscilloscope and the bit error detector. Fig. 4 depicts the eye diagram at a BER of 10^{-9}. The eye opening is symmetric though laser relaxation oscillation is observed when switching from low to high level. The results of the transmission experiments are summarized in Fig. 5 where full circles denote back to back testing. A 2^7–1 non-return-ow zero PRBS has been choosen since long sequences of "1" lead to additional errors caused by the low end cut-off frequency of the second stage amplifier.

Optimum results with no noise floor and $\eta\langle P\rangle$=–13.1 dBm required for a BER of 10^{-11} are obtained at 3.4 mA bias current and $m = 50\,\%$ optical modulation depth determined with an optical sampling oscilloscope. The driving conditions avoid dynamic transverse mode transitions as well as dynamic polarization switching and yield extremly stable single-mode linearly polarized light output as indicated in Fig. 2 and Fig. 3. The receiver sensitivity limit is given by thermal noise of the 50 Ω resistor in the front end and the noise figure F=2.5 (F_{dB}=4 dB) of the first stage amplifier. Using

$$\eta < P >= \frac{h\nu}{q}\frac{Q}{m}\sqrt{\frac{FkT\Delta f}{R}} \tag{1}$$

where η is the quantum efficiency of the photodetector, h Planck's constant, ν the optical frequency, q the electron charge, k Boltzmann's constant, T the temperature and Δf the bandwidth a mean optical power of $\eta\langle P\rangle$ = –16.7 dBm for a quality factor Q = 6 as required for a BER of 10^{-9} is calculated. The difference of 2.7 dB is attributed to laser relaxation oscillation and intersymbol interference caused by the low end cut-off frequency of the electrical amplifier. The power penalty after 500 m graded index fiber transmission of 1.7 dB at a BER of 10^{-11} is due to fiber dispersion. The fiber dispersion power penalty is lower than expected for graded index

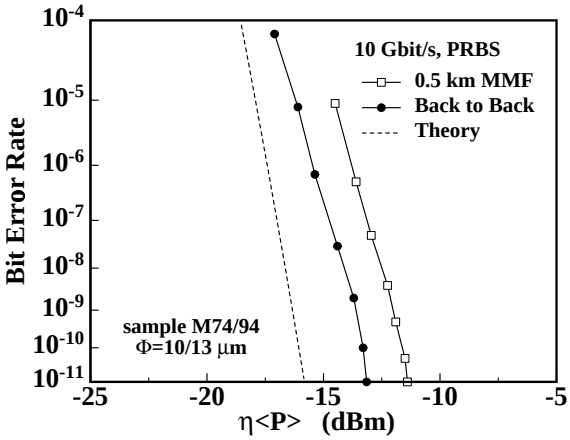

Fig. 5: BER measurement at 10 Gbit/s with 2^7–1 PRBS using small size VCSEL for transmission over 500 m of graded index multi-mode fiber. The dashed line indicates the receiver limit for 50 % optical modulation depth.

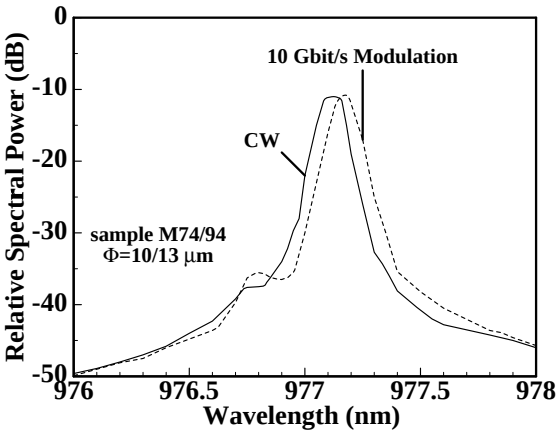

Fig. 6: Spectra of 10/13 μm VCSEL at I_L=3.4 mA measured with 0.1 nm resolution. The full line depicts cw-operation only and the dashed line 10 Gbit/s PRBS modulation.

multi-mode fibers since the power is mainly guided in the center of the fiber core. Sharp bending at the transmitter end leading to higher order mode excitation is avoided. Fig. 6 shows both the cw-spectrum as well as the spectrum of the modulated laser on a logarithmic plot at a bias current of 3.4 mA. With 10 Gbit/s PRBS the lasing mode is 0.1 nm red shifted due to additional power dissipation. Since no spectral broadening is observed the chirp is certainly less than the resolution bandwidth of 0.1 nm. The suppression of the side mode at 976.8 nm decreases from 27 dB for cw operation to 25.2 dB in the modulated case.

V. Conclusion

We demonstrate 10 Gbit/s PRBS data transmission with nearly single-mode operating VCSELs using intensity modulation and direct detection. A BER of 10^{-11} is achieved for both back to back testing as well as transmission over 500 m of graded index multi-mode fiber. The power penalty of 1.7 dB compared to back to back testing is attributed to fiber dispersion. To our knowledge this is the highest pseudo random bit sequence transmitted with a VCSEL to date. The LP_{11} mode suppression of the modulated VCSEL is better than 25 dB. Analysis of spectral and polarization characteristics show that dynamic polarization mode switching as well as higher order transverse mode oscillation should be avoided to achieve minimum laser noise and a minimum BER as long as modal noise is negligible. The transmission experiments demonstrate that polarization control in top surface-emitting VCSELs is very important to enhance VCSEL performance in high-speed optical interconnects, short distance communication and board-to-board data links.

References

[1] K. Hahn, "Gigabyte/s Data Communication with the VCSEL based POLO Module," *in Proc. 8th Annual Meeting LEOS*, San Francisco, vol. 1, pp. 228-229, 1995.

[2] G. Reiner, E. Zeeb, M. Ries, and K.J. Ebeling, "Optimization of planar Be-doped InGaAs VCSELs with two-sided output," *IEEE Photonics Technol. Lett.*, vol. 7, pp. 730-732, July 1995.

[3] M.G. Peters, D.B. Young, F.H. Peters, J.W. Thibeault, and L.A. Coldren, "17.3 % peak wall-plug efficiency vertical-cavity surface-emitting lasers using lower barrier mirrors," *IEEE Photonics Technol. Lett.*, vol. 6, pp. 31-33, Jan. 1995.

[4] K.L. Lear, R.P. Schneider, K.D. Choquette, S.P. Kilcoyne, J.J. Figiel, and J.C. Zolper, "Vertical cavity surface emitting lasers with 21 % efficiency by metalorganic vapor phase epitaxy," *IEEE Photonics Technol. Lett.*, vol. 6, pp. 1053-1055, Sept. 1994.

[5] B. Möller, E. Zeeb, T. Hackbarth, and K.J. Ebeling, "High speed performance of 2-D vertical-cavity laser diode arrays," *IEEE Photonics Technol. Lett.*, vol. 6, pp. 1056-1058, Sept. 1994.

[6] U. Fiedler and K.J. Ebeling, "Design of VCSELs for feedback insensitive data transmission and external cavity active mode-locking," *IEEE J. of Select. Topics in Quantum Electron.*, vol. 1, pp. 442-450, June 1995.

[7] K.L. Lear, K.D. Choquette, R.P. Schneider, S.P. Kilcocyne and K.M. Geib, "Selectively oxidised vertical cavity surface emitting lasers with 50 % power conversion efficiency," *Electron. Lett.*, vol. 31, pp. 208-209, Feb. 1995.

[8] G.M. Yang, M.H. MacDougal, and P.D. Dapkus, "Ultralow threshold current vertical-cavity surface-emitting lasers obtained with selective oxidation," *Electron. Lett.*, vol. 31, pp.886-888, May 1995.

[9] H. Kosaka, A.K. Dutta, K. Kurihara, Y. Sugimoto, and K. Kasahara, "Giga-bit-rate optical-signal transmission using vertical-cavity surface-emitting lasers with large-core plastic-cladding fibers," *IEEE Photonics Technol. Lett.*, Aug. 1994, vol. 7, Aug. 1995, pp.926-928.

[10] U. Fiedler, B. Möller, G. Reiner, D. Wiedenmann, and K.J. Ebeling, "Proton implanted VCSELs for 3 Gbit/s data links," *IEEE Photonics Technol. Lett.*, vol. 7, Oct. 1995, in press.

[11] J.W. Scott, F.H. Peters, B.J. Thibeault, D.B. Young, L.A. Coldren, and C.J. Mahon, "2.488 Gbit/s optical data transmission with linear arrays of intra-cavity contacted, top emitting vertical cavity lasers," *20th European Conf. on Optical Comm.*, pp. 339-342, Firenze, Sept 1994.

[12] K.D. Choquette, R.P. Schneider, K.L. Lear, R.E. Leibenguth, "Gain-dependent polarization properties of vertical-cavity lasers," *IEEE J. of Select. Topics in Quantum Electron.*, vol. 1, pp. 661-666, June 1995.

Simple Understanding of Waveguiding in Oxidized VCSELs

Rainer Michalzik

In this contribution, the waveguiding mechanism in oxidized vertical-cavity surface-emitting laser diodes is explained in an instructive manner. It is shown that the detuning of the cavity in the oxidized section results in the formation of an effective index guide, the effectiveness of which is strongly dependent on both the thickness of the oxide layer and its position in the standing wave field of the cavity. From the induced index step, the wavelength separation of different transverse modes can easily be inferred.

1. Introduction

In the last year, vertical-cavity surface-emitting lasers (VCSELs) employing selectively oxidized AlAs layers for current confinement have set new performance standards for devices operating in the 980 nm as well as in the 650 nm short wavelength regimes [1]-[4]. With conversion efficiencies up to 50 % [1], [3], thermally induced index guiding is expected to play no longer the dominant role for mode guiding, as is usually the case in proton-implanted lasers [5]. For the investigation of the transverse mode behavior of oxidized VCSELs, a theoretical understanding of the waveguiding mechanism and thus of the influence of the oxide layer is of crucial importance. This article attempts to give an understanding of the index waveguide formation in the device with an intuitive rather than a strictly theoretical approach [6]. It provides a method for calculating an effective index step from a given layer structure and to get information about the wavelength separation of different transverse modes.

2. Formation of an Effective Index Guide

In Fig. 1, the reflectivity spectrum $R_c(\lambda)$, determined with the one-dimensional transfer matrix method [7]-[8], is shown for a VCSEL with a one-wavelength thick inner cavity tuned to an emission wavelength of 980 nm, a 24 pairs $Al_{0.67}Ga_{0.33}As$-GaAs top and a 25.5 pairs AlAs-GaAs bottom Bragg reflector. As also schematically illustrated in Fig. 1, a single AlGaAs layer in the top mirror, adjacent to the inner cavity, is replaced by AlAs and is partially oxidized in a wet vapor atmosphere. The resulting aluminum oxide is electrically isolating and thus provides an aperture for current injection from a top ring contact into the active layer. For further details of the oxidation process and the layer structure, especially in the inner cavity, the reader is referred to other articles in this annual report.

Measurements have indicated that the refractive index of the oxide has a value of $\bar{n}_{ox} = 1.55$ [9] and is thus considerably smaller than that of AlAs, $\bar{n}_{sc} = 2.97$. The calculation of the reflectivity spectrum $R_{ox}(\lambda)$ in the oxidized section of the VCSEL consequently shows that the cavity resonance is shifted to shorter wavelengths by an amount $\Delta\lambda_{ox}$. For an AlAs layer thickness of $d_{sc} = d_{ox} = 82.5$ nm, a wavelength shift of $\Delta\lambda_{ox} = -19.2$ nm is read from Fig. 1[1].

[1] An observed shrinkage of the layer during oxidation [9]-[10] is not taken into account here. In fact, the structural and geometrical details at the oxidation front are still unknown.

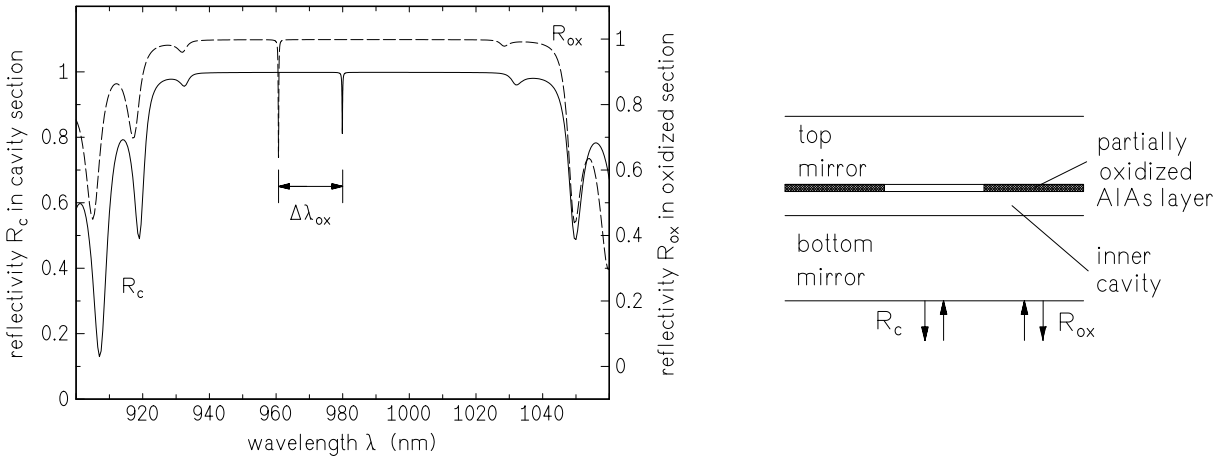

Fig. 1: Reflectivity spectra in the cavity section and the oxidized section of a selectively oxidized VCSEL, as seen from the GaAs substrate (left), and schematic cross section of the device (right).

The detuning of the cavity in the passive part of the laser can also be considered as to be a result of a reduction of the mean refractive index $< \bar{n} >$ in the laser for radii larger than the active radius r_a. The effective cavity model of a VCSEL as a resonator with a fixed geometrical length L_{eff} accordingly implies a cavity index variation

$$\Delta\bar{n}_{eff,c} = \Delta\lambda_{ox} \cdot \frac{< \bar{n} >}{\lambda} \,, \tag{1}$$

which is proportional to the wavelength shift. With $\lambda = 980\,\mathrm{nm}$ and $< \bar{n} >= 3.3$, the effective cavity index step is calculated to be $\Delta\bar{n}_{eff,c} = -6.5 \cdot 10^{-2}$ in the example of Fig. 1, which turns out to provide a rather strong waveguiding. For illustration, a temperature variation of more than 200 K from the center of the laser to the active radius would be necessary to give the same amount of thermally induced index guiding, if a temperature coefficient $\Delta\bar{n}/\Delta T = 3 \cdot 10^{-4}\,\mathrm{K}^{-1}$ of the semiconductor is assumed [11]. For a deeper understanding of the influence of the oxide layer, the cavity detuning has to be investigated in more detail.

3. Understanding of the Cavity Detuning

The representation of the multilayered VCSEL structure as an effective cavity with length L_{eff} provides a first analytical estimate for the theoretically observed wavelength shift. According to this model, the change of the mean refractive index in the oxidized cavity translates into a detuning of

$$\Delta\lambda_{ox} = \lambda \cdot \frac{d_{ox}}{L_{eff}} \cdot \frac{\bar{n}_{ox} - \bar{n}_{sc}}{< \bar{n} >} \,, \tag{2}$$

which varies linearly with the oxide thickness. A more accurate description can, however, only be obtained numerically, for example with the matrix method. In Fig. 2, the wavelength detuning is plotted as a function of the oxide thickness for three different positions of the oxide layer in the cavity, namely in the first, second, or third Bragg pair of the top mirror, as seen from the active zone. The remainder of the quarter-wavelength layer not being occupied by the oxide is again replaced by $Al_{0.67}Ga_{0.33}As$.

With increasing distance from the active layer, the detuning of the cavity becomes smaller and a saturation of $\Delta\lambda_{ox}$ is observed when the thickness of the oxide approaches that of the quarter-wavelength layer. The nonlinear dependence $\Delta\lambda_{ox} = \Delta\lambda_{ox}(d_{ox})$ results in a large deviation from the analytical estimation (2) for thicknesses $d_{ox} > 30\,\mathrm{nm}$.

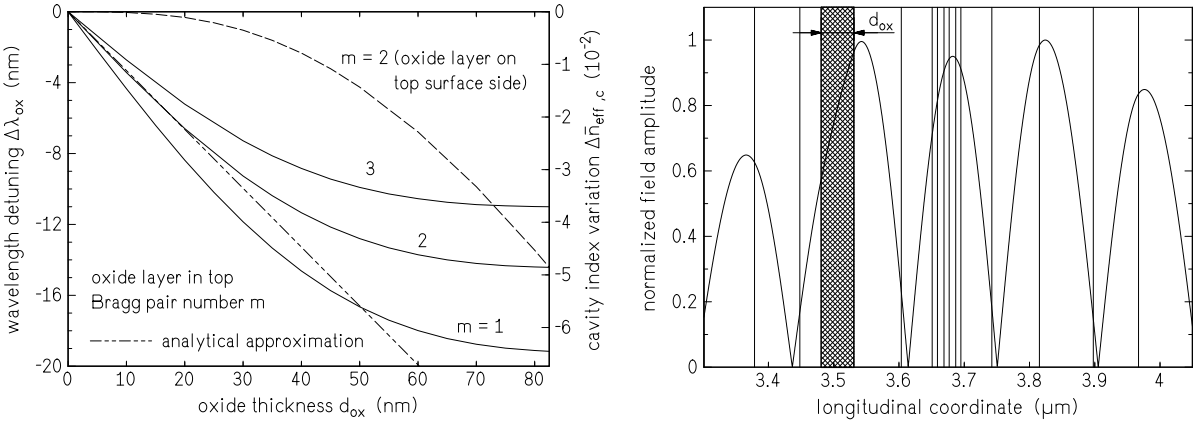

Fig. 2: Dependence of the cavity wavelength shift from the thickness of the oxide layer, which is located in the mth Bragg pair of the top mirror (left) and the resonant standing wave pattern in the oxidized VCSEL section for the case $m = 1$ and $d_{ox} = 50\,\mathrm{nm}$ in the vicinity of the 3 QW inner cavity (right). In contrast to the solid curves, the dashed curve for $m = 2$ in the left diagram is calculated for the oxide being located at the top surface side of the quarter-wavelength layer. Also included is the analytical relation $\Delta\lambda_{ox}(d_{ox})$ as the dash-dotted line according to (2) and the conversion (1) of the wavelength shift into an effective cavity index variation for $\lambda = 980\,\mathrm{nm}$ and $< \bar{n} >= 3.3$.

The shape of the solid curves in Fig. 2 is well understood by looking at the standing wave pattern in the VCSEL, depicted in the second diagram of the figure. The decreasing wavelength shift with increasing Bragg pair number m is apparently due to the decaying field amplitude in the top mirror. The perturbation of the cavity is the stronger, the higher the field amplitude in the oxide layer is. For a large thickness d_{ox}, the index perturbation is introduced near to a node of the electric field, thus resulting in the observed saturation behavior of the wavelength shift. This effect is even better seen if the oxide is located at the top surface side of the quarter-wavelength layer, as is the case for the dashed curve in the left part of Fig. 2.

The above discussion clearly shows the importance of correctly placing the oxide layer in the laser cavity and of deliberately choosing its thickness if one wishes to achieve a certain amount of index guiding in addition to current confinement.

4. Transverse Mode Spacing

As explained in section 2, an oxidized VCSEL, from the waveguiding point of view, can be approximated by a step index guide of diameter $2r_a$ and index difference $\Delta\bar{n}_{eff,c}$. The properties of the guided modes in such a waveguide have been intensively investigated in optical fiber theory. In an optical resonator, the difference in propagation constants between the transverse modes translates into a resonance wavelength shift to satisfy the phase condition for a complete round trip of the optical field. Using the approach taken in [12], Fig. 3 shows the wavelength

spacing between the lowest order LP_{01} and LP_{11} transverse modes as a function of the laser active diameter for a number of cavity index steps $\Delta\bar{n}_{eff,c}$. An increase of mode spacing with decreasing active diameter and increasing index difference is observed. High values of several nm are predicted for small diameter devices, e.g., $\Delta\lambda_{01-11} = 3\,\mathrm{nm}$ for $d_a = 2r_a = 3\,\mu\mathrm{m}$ and a moderate index step of $\Delta\bar{n}_{eff,c} = -0.05$. For weak guiding, the higher order mode cutoff can be reached, as is the case for $\Delta\bar{n}_{eff,c} = -0.01$ at a diameter of $d_a = 2.9\,\mu\mathrm{m}$ in Fig. 3.

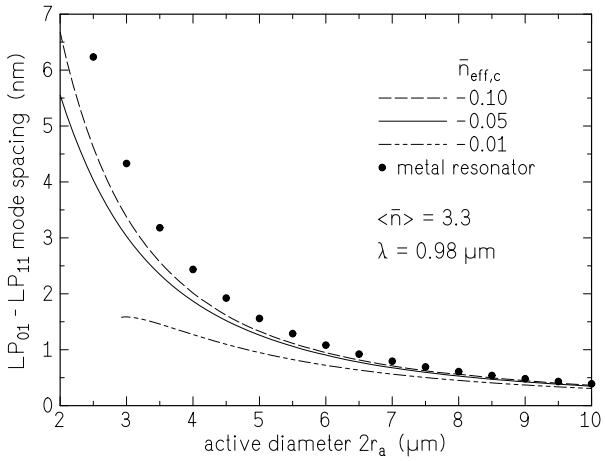

Fig. 3: Wavelength spacing between the fundamental LP_{01} mode and the higher order LP_{11} donut mode vs. laser active diameter for different effective cavity index steps $\Delta\bar{n}_{eff,c}$. The dots represent the analytically calculated values for the modes of a circular metal resonator.

The stronger the index guiding, the more do the mode profiles resemble the shape of eigenmodes in a circular waveguide of refractive index $< \bar{n} >$ with an ideally conducting boundary at $r = r_a$. The wavelength spacing of these modes in a metal resonator can be written as [12]

$$\Delta\lambda_{01-11} = \lambda_{01} - \lambda_{11} = \frac{\lambda^3}{2(2\pi < \bar{n} > r_a)^2}\left(x_{11}^2 - x_{01}^2\right) \quad , \tag{3}$$

where x_{lp} is the pth zero of the Bessel function J_l. In this limiting case, the wavelength spacing is inversely proportional to the active area $A_a = \pi r_a^2$. With $x_{01} = 2.41$ and $x_{11} = 3.83$, the relation (3) is also plotted in Fig. 3. As expected, the deviation from the curves calculated for index guiding vanishes for large diameter devices. It is important to note that the factor λ^3 in (3) can account for considerably different mode spacings in short or long wavelength VCSELs, compared to Fig. 3.

5. Conclusion

In this article, a simple method for investigating the induced index guiding in oxidized vertical-cavity lasers has been presented. It is based on the one-dimensional evaluation of the resonance condition in the active as well as in the passive sections of the device and leads to the representation of the VCSEL in terms of a step index waveguide. From the properties of the guided eigenmodes, the wavelength spacing of different transverse modes is readily obtained. Due to the strong guiding and the improved power conversion compared to proton-implanted devices, thermally induced index guiding is expected to be of less importance, relieving the necessity of employing more elaborate models for cavity analysis [13].

References

[1] K.L. Lear, K.D. Choquette, R.P. Schneider, Jr., S.P. Kilcoyne, and K.M. Geib, "Selectively oxidized vertical cavity surface emitting lasers with 50 % power conversion efficiency," *Electron. Lett.*, vol. 31, pp. 208-209, 1995.

[2] G.M. Yang, M.H. MacDougal, and P.D. Dapkus, "Ultralow threshold current vertical-cavity surface-emitting lasers obtained with selective oxidation," *Electron. Lett.*, vol. 31, pp. 886-888, 1995.

[3] B. Weigl, G. Reiner, M. Grabherr, and K.J. Ebeling, "High-power selectively oxidized vertical-cavity surface-emitting lasers," in Proc. *Conf. on Lasers and Electro-Optics*, CLEO'96, Anaheim, CA, USA, June 1996, paper JTuH2.

[4] K.D. Choquette, R.P. Schneider, Jr., M. Hagerott Crawford, K.M. Geib, and J.J. Figiel, "Selective oxidation for record cw 640-660 nm AlGaInP VCSELs," in Proc. *Conf. on Lasers and Electro-Optics*, CLEO'95, Baltimore, MD, USA, May 1995, paper CPD5-1.

[5] R. Michalzik and K.J. Ebeling, "Modeling and design of proton-implanted ultralow-threshold vertical-cavity laser diodes," *IEEE J. Quantum Electron.*, vol. 29, pp. 1963-1974, 1993.

[6] G.R. Hadley, "Effective index model for vertical-cavity surface-emitting lasers," *Opt. Lett.*, vol. 20, pp. 1483-1485, 1995.

[7] M. Born and E. Wolf, *Principles of Optics,* 6th Edition. Pergamon Press, Oxford 1989.

[8] P. Yeh, *Optical Waves in Layered Media.* J. Wiley & Sons, New York 1988.

[9] M.H. MacDougal, H. Zhao, P.D. Dapkus, M. Ziari, and W.H. Steier, "Wide-bandwidth distributed Bragg reflectors usinf oxide/GaAs multilayers," *Electron. Lett.*, vol. 30, pp. 1147-1148, 1994.

[10] M.H. MacDougal, P.D. Dapkus, V. Pudikov, H. Zhao, and G.M. Yang, "Ultralow threshold current vertical-cavity surface-emitting lasers with AlAs oxide-GaAs distributed Bragg reflectors," *IEEE Photon. Technol. Lett.*, vol. 7, pp. 229-231, 1995.

[11] D.T.F. Marple, "Refractive index of GaAs," *J. Appl. Phys.*, vol. 35, pp. 1241-1242, 1964.

[12] R. Michalzik and K.J. Ebeling, "Generalized BV diagrams for higher order transverse modes in planar vertical-cavity laser diodes," *IEEE J. Quantum Electron.*, vol. 31, pp. 1371-1379, 1995.

[13] R. Michalzik and K.J. Ebeling, "Quasi-3D Modeling of Vertical-Cavity Surface Emitting Laser Operation," in *Physics and Simulation of Optoelectronic Devices III*, M. Osiński and W.W. Chow (Eds.), Proc. SPIE 2399, pp. 360-371, 1995.

Double-Fused Long-Wavelength Vertical-Cavity Surface-Emitting Lasers

Torsten Wipiejewski

We introduce a vertical-cavity surface-emitting laser design to achieve continuous-wave laser operation at an emission wavelength of 1.55 μm. The device employs two wafer fused InP-GaAs interfaces. Wet oxidation of an AlAs layer in one of the Bragg reflectors provides current confinement. We analyze the optical and thermal properties of the structure and estimate the optimum device diameter based on the size dependence of laser parameters.

1. Introduction

Vertical-cavity surface-emitting laser diodes (VCSELs) at wavelengths of 1.3 μm or 1.55 μm are much harder to fabricate than in the short wavelength regime at 980 nm or 850 nm. This is mainly because there are no highly reflecting Bragg mirrors with good thermal conductivity which are easy to fabricate in one epitaxial growth run. The AlAs-GaAs Bragg reflectors used for short-wavelength VCSELs are also good candidates for devices in the longer wavelength regime due to the good optical properties and the high thermal conductivity. It is necessary bond them to InP based active material for laser fabrication. A technique called wafer fusion provides the required mechanical bonding between the non-lattice matched InP and GaAs material with no optical loss and good electrical characteristics. Due to excellent results obtained recently with wafer-fused VCSELs [1] we decided to explore the fabrication of a double-fused vertical-cavity laser structure for 1.55 μm emission wavelength. Here we want to introduce the device structure and discuss some modeling aspects that are important for laser operation.

2. Schematic

Figure 1 shows a schematic of a double-fused VCSEL for an emission wavelength of 1.55 μm. The InGaAsP-InP active material is sandwiched between two GaAs based distributed Bragg reflectors. There are two wafer-fused interfaces one above and one below the active layer. An n-type doped GaAs substrate provides mechanical support for the laser. The bottom DBR is n-type doped and consists of 28 periods AlAs-GaAs layers each with a thickness corresponding to a quarter wavelength. The top DBR is p-type doped with 30 periods of $Al_{0.67}Ga_{0.33}As$-GaAs. We employ AlGaAs as low index material rather than AlAs to reduce the voltage drop in the mirror [2]. The top reflector also contains a thin AlAs layer just above the active layer. This AlAs is partly oxidized after mesa etching. The oxidized AlAs provides an aperture for current injection into the active layer. We intent to fabricate mesa diameters ranging from about 40 μm to 54 μm with corresponding diameters for the current aperture of 6 μm to 20 μm. The incorporation of oxidized AlAs layers for current funneling has led to dramatic improvements in short-wavelength VCSEL performance [3], [4]. Therefore, we think it is promising to use the same technique for wafer-fused long-wavelength VCSELs. The active layer consists of seven 1% compressively strained InGaAsP quantum wells and InGaAsP barriers with 0.9% tensile strain. They are surrounded by 314 nm thick InP cladding layers.

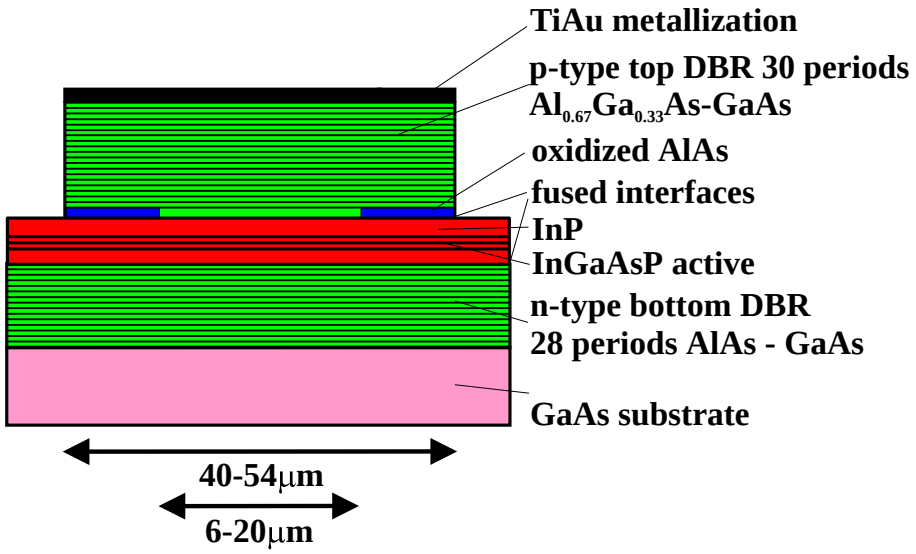

Fig. 1: Schematic of a long-wavelength double-fused VCSEL

3. DBR Reflectivity

We can analytically calculate the reflectivity of the laser mirrors. For the 28 period AlAs-GaAs bottom DBR we obtain a power reflectivity of $R_b = 99.93\%$ at 1.55 μm wavelength. The 30 period $Al_{0.67}Ga_{0.33}As$-GaAs top DBR exhibits a reflectivity of 99.04% which is further boosted by the Au metal reflector to a total reflectivity of $R_t = 99.98\%$. The mirror reflectivity in the VCSEL is reduced by diffraction loss. For a laser with 10 μm active diameter we calculate a finesse of $F = 78.7$ for the bottom DBR. This finesse translates to a diffraction loss of $\delta = 0.00043$ which decreases the effective bottom mirror reflectivity to $R_b = 99.89\%$. For the top mirror we obtain a lower finesse of $F = 49.7$ due to the smaller refractive index difference between $Al_{0.67}Ga_{0.33}As$ and GaAs. Thus, the diffraction loss is somewhat higher ($\delta = 0.00086$) resulting in an effective top mirror reflectivity of $R_t = 99.89\%$. It is suprising that due to diffraction loss the effective reflectivityis the same for the top and the bottom mirror. In general, the reflectivity of the output coupler should be lower to obtain high efficiency. We can achieve this by reducing the number of bottom DBR periods in future VCSEL designs. Initially, we aim at getting as much reflectivity as possible for both mirrors to ensure laser operation.

4. Thermal Properties

The thermal impedance of a vertical-cavity laser is an important parameter, because it determines the temperature rise in the laser due to the dissipated electrical input power. The available optical gain in the active material decreases with increasing temperature and also the maximum output power is limited by thermal roll-over. The temperature profile for various VCSEL structures has been calculated with numerical analysis by many authors in the literature. Experimental data [5] suggests that it is a good approximation to calculate the thermal

impedance for mesa-type VCSELs by using the simple analytical formula

$$R_{th} = \frac{1}{2\sigma_{th} d}$$

where d is the laser diameter and σ_{th} is the average thermal conductivity of the laser material below the active layer. An experimental value of $\sigma_{th} = 0.28$ W/(cmK) [5] was measured for 980 nm wavelength VCSELs with AlAs-GaAs Bragg reflectors which is much smaller than the average thermal conductivity of bulk AlAs and GaAs layers. It is expected that phonon scattering at the interfaces of the thin DBR layers causes this increase of the thermal resistance. This is supported by the fact that the experimentally determined value is close to numbers obtained by other authors for AlAs-GaAs superlattices. In Fig. 3 we calculated the thermal resistance as function of laser diameter for an average thermal conductivity of $\sigma_{th} = 0.28$ W/(cmK).

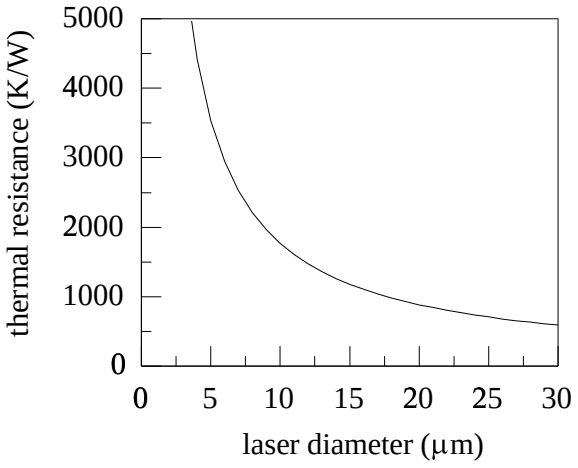

Fig. 2: Calculated thermal resistance as function of laser diameter for $\sigma_{th} = 0.28$ W/(cmK).

For long-wavelength VCSELs we can speculate that the average thermal conductivity of the AlAs-GaAs Bragg reflector material is higher than for 980 nm VCSELs, because phonon scattering is less pronounced in the thicker AlAs and GaAs layers. The average thermal conductivity is probably closer to the mean thermal conductivity of GaAs and AlAs:

$$\sigma_{th} = \frac{\sigma_{th,GaAs} d_{GaAs} + \sigma_{th,AlAs} d_{AlAs})}{d_{GaAs} + d_{AlAs}} = 0.7 \text{ W/(cmK)}$$

Thus, the thermal impedance of double-fused long-wavelength VCSELs might be up to about 50% lower compared to 980 nm VCSELs of the same diameter.

5. Temperature at Threshold

We want to calculate the internal temperature increase ΔT of the laser at threshold. From the size dependence of ΔT we can estimate the laser diameters with the lowest operating temperature. These devices are most likely to start lasing. The temperature increase ΔT is given by the dissipated electrical power ΔP and the thermal resistance of the device R_{th}

$$\Delta T = R_{th} \Delta P = \rho d u j_{th} \frac{\pi}{4} d^2$$

where we substituted the size dependence of $R_{th} = \rho d$ and of the threshold current $i_{th} = j_{th} \frac{\pi}{4} d^2$. We neglect the small size dependence of the threshold voltage u. Size dependent optical loss

causes an increase of the threshold current density j_{th} for small VCSEL diameters. We describe this relation with the empirical formula

$$j_{th} = j_o[1 + (d_o/d)^3]$$

The parameter d_o represents the amount of excess optical loss. It critically depends on the exact laser structure. We assume a value of $d_o = 8$ μm for the double-fused VCSEL.

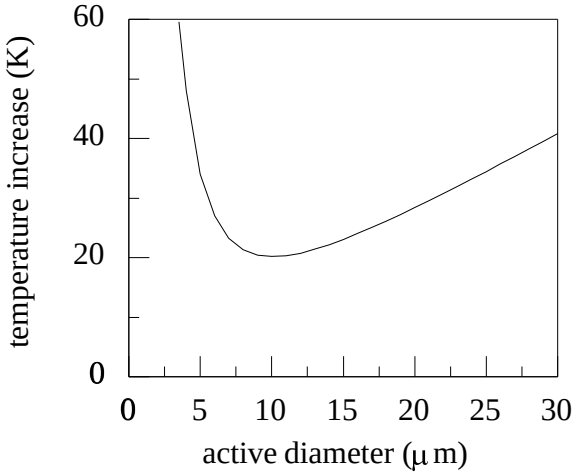

Fig. 3: Calculated laser temperature increase as function of device diameter for $u = 4$V, $j_o = 2.5$ kA/cm^2, and $\rho = 1.7$ cmK/W.

The two equations give the temperature increase as function of laser diameter as plotted in Fig. 4. We used typical parameters of $u = 4$V, $j_o = 2.5$ kA/cm^2, and $\rho = 1.7$ cmK/W. The lowest temperature at threshold occurs for lasers with diameters of $d_{min} = 10$ μm. The temperature increase is $T_{min} = 20$ K. Thus, we expect VCSELs with diameters around 10 μm to be the most promising candidates for continuous wave operation at room temperature. The temperature increase we want to minimize is small for good heat sinking, low voltage, low threshold current density, and low size dependent excess loss.

6. Conclusion

We introduced a double-fused vertical-cavity surface-emitting laser structure for operation at 1.55 μm emission wavelength. We discussed some of the optical and thermal characteristics of the laser and estimated that devices of around 10 μm diameter are the most promising candidates to achieve continuous wave operation at room temperature. Low voltage drop and low optical loss as well as good heat sinking of the active region are important factors which affect laser operation.

References

[1] D.I. Babic, K. Streubel, R.P. Mirin, N.M. Margalit, J.E. Bowers, E.L. Hu, D.E. Mars, L. Yang, K. Carey, "Room-temperature continuous-wave operation of 1.54 μm vertical-cavity laser," *10th IOOC*, post-deadline paper PD1-5, , Hong Kong, 1995.

[2] M.G. Peters, D.B. Young, F.H. Peters, J.W. Scott, B.J. Thibeault, L.A. Coldren, "17.3% peak wall plug efficiency vertical-cavity surface-emitting lasers using lower barrier mirrors," *IEEE Photon. Technol. Lett.*, vol. 6, pp. 31-33, 1994.

[3] K.L. Lear, K.D. Choquette, R.P. Schneider, S.P. Kilcoyne, K.M. Geib, "Selectively oxidized vertical cavity surface emitting lasers with 50% power conversion efficiency," *Electron. Lett.*, vol. 31, pp. 208-209, 1995.

[4] B. Weigl, G. Reiner, M. Grabherr, K.J. Ebeling, "High Power Selectively Oxidized Vertical-Cavity Surface-Emitting Lasers," *CLEO*, Anaheim, CA, June 1996.

[5] T. Wipiejewski, M.G. Peters, D.B. Young, B.J. Thibeault, G.A. Fish, L.A. Coldren, "Thermal Resistance of Etched-Pillar Vertical-Cavity Surface-Emitting Laser Diodes," *SPIE Int. Symposium on Optoelectronic Packaging*, San Jose, CA, Jan. 1996.

High-Reflecting Mirrors for Long-Wavelength Vertical-Cavity Surface-Emitting Lasers

Dirck Sowada, Hin Yiu Anthony Chung, Georgi Stareev, Torsten Wipiejewski

Vertical-cavity surface-emitting lasers operating in the 1.3 μm and 1.5 μm wavelength range are highly attractive for telecommunication applications. However, they are far less well developed than devices operating at shorter wavelengths. Long growth times are required for highly-reflecting epitaxial mirrors. In this report we discuss dielectric MgO/α-Si mirrors and oxidized $In_{0.52}Al_{0.48}As$ layers on InP substrates. Reflection measurements of evaporated MgO/α-Si mirrors show good agreement with simulated results. We can achieve a maximum reflectivity of about 99.2% assuming an absorption coefficient of 800 cm^{-1}. The native oxidation of lattice matched 120-nm-thick $In_{0.52}Al_{0.48}As$ layers shows an oxidation rate of 600 nm/h at an oxidation temperature of T_{ox}=520 °C. This is 48 times slower than the oxidation rate of 27-nm-thick AlAs layers.

1. Introduction

Vertical-cavity surface-emitting lasers (VCSELs) have generated a lot of interest for optical systems due to their surface-emitting nature. Their benefits include simple integration into 2-D arrays, on-wafer testing, and efficient fiber coupling. The first near room temperature (14 °C) cw operation of an electrically pumped VCSEL at 1.3 μm [1] and low-threshold-current roomtemperature pulsed lasing at 1.5 μm [2] have been achieved recently. Both structures employ two dielectric reflectors, which require removal of the substrate. Recently, very encouraging results have been reported using wafer fusion of AlGaAs-based Bragg reflectors and InP-based active material. Roomtemperature continuous-wave operation of 1.54-μm double-fused vertical-cavity lasers was demonstrated with a minimum threshold current of 2.3 mA and highest cw operating temperature of 33 °C [3][4].

There are several requirements for distributed Bragg reflectors (DBRs) used in VCSELs. First of all they must have a very high reflectivity (above 99%) to satisfy the laser threshold condition with the small optical gain of the extremly thin active material in quantum well structures. The reflectors must also exhibit a good thermal conductivity to provide heat sinking of the active region. This property is required at least for one of the two laser mirrors. Furthermore, the DBR should be electrically conductive, because the injection of laser current through the mirror simplifies the laser structure and the fabrication process. The other case requires lateral current injection which is harder to achieve and can cause problems like current crowding at the edge of the active area.

In this report we discuss dielectric MgO/α-Si mirrors for long-wavelength VCSELs and oxidized InAlAs/InP mirrors on InP-substrates.

2. Dielectric MgO/α-Si Mirrors

We investigated the materials MgO and amorphous Si for long-wavelength VCSELs. In Fig. 1 we plotted the refractive index and the absorption loss of e-beam-evaporated amorphous silicon.

Deposition conditions are a vacuum pressure of less than 5×10^{-6} torr, low evaporation rates of 0.2 to 0.5 nm/sec and large crucible-to-substrate distance ($\approx$ 40 cm) [5]. The amorphous Si with the high refractive index is not an ideal material, because of its low thermal conductivity of $\lambda_c = 0.26$ W/cmK and its high optical loss at 1.3 μm and 1.55 μm wavelength. At 1.55 μm wavelength, α-Si shows a refractive index of nearly 3.48 and an absorption coefficient of 800 cm^{-1}. MgO has a higher thermal conductivity ($\lambda_c = 0.6$ W/cmK) than even GaAs ($\lambda_c = 0.45$ W/cmK). At 1.55 μm wavelength, the refractive index is about 1.72, the absorption loss is negligible. The optical loss depends on the deposition conditions and limits the maximum achievable reflectivity from such a mirror. The combination of both materials for dielectric mirrors should result in good optical and thermal properties. In Fig. 2 we plotted the maximum reflectivity at the resonance wavelength of 1.55 μm for a MgO/α-Si mirror as function of layer pairs. The reflectivity of the multilayer stack was numerical calculated with the transfer matrix theory described in [6].

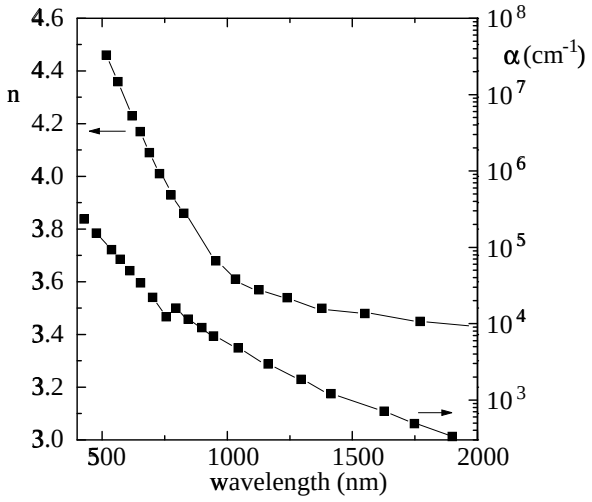

Fig. 1: Refractive index and absorption coefficient for amorphous silicon [6].

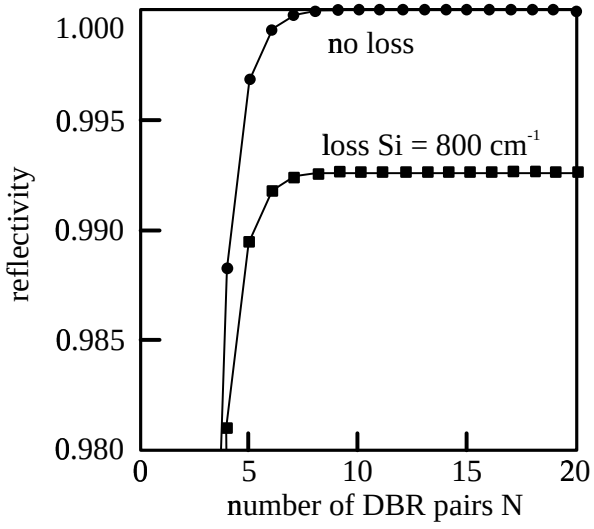

Fig. 2: Maximum reflectivity at resonance wavelength 1.55 μm for an MgO/α-Si mirror as a function of layer pairs.

Due to the large refractive index difference we obtain a high reflectivity already for a few DBR periods. The absorption in the α-Si limits the maximum reflectivity. If we assume an absorption coefficient of 800 cm^{-1} (Fig. 1), we obtain a maximum reflectivity of about 99.2%.

The measured (solid line) and simulated plot (dotted line) of a three period MgO/α-Si DBR in Fig. 3 agree quite well. The deviation for long wavelengths is due to a measurement error.

We intent to fabricate a hybrid mirror consisting of a MgO/α-Si DBR and a metal reflector i.e. Ag to obtain a higher reflectivity and a lower thermal resistance.

2. Oxidation of $In_xAl_{1-x}As$ layers

A relatively simple new technique called native oxidation ("wet" chemical oxidation via H_2O vapor + N_2) was proposed recently for the preparation of index-guided laser structures on GaAs substrates [7]. Wet oxidation of InAlAs lattice matched to InP was employed to fabricate long wavelength InAlAs-InP-InGaAsP gain-guided native-oxide-defined stripe-geometry laser diodes

[8]. If the Al content x of the confining layers is high enough ($x > 0.5$), the layer can be transformed into a stable native oxide by heating in water vapour. This simple technique for current blocking and optical confinement offers a promising alternative to buried heterostructure lasers based on multiple epitaxial growth.

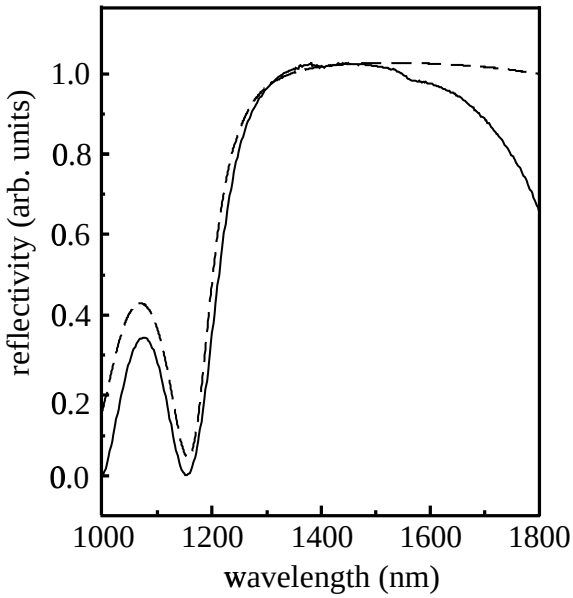

Fig. 3: Measured and simulated plots of a three-period MgO/α-Si DBR on silicon substrate.

Mac Dougal et al. fabricated the first electrically-pumped VCSELs with Al_xO_y/GaAs DBRs on both sides of the gain region [9]. The required epitaxial growth time is only a third compared to VCSELs with semiconductor DBRs.

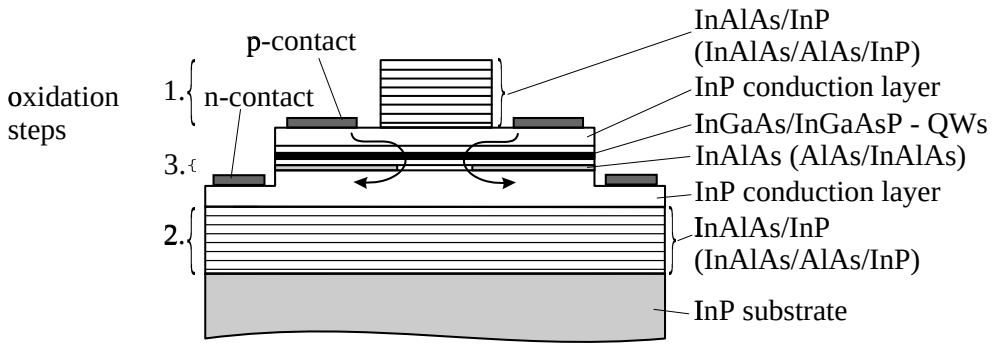

Fig. 4: Schematic of a InP-based VCSEL structure with oxidized DBRs and current confinement layer. Holes are injected into the p-InP and funneled into the InGaAs QWs by the oxide current constriction layer. Electrons are injected into the n-InP.

Fig. 4 shows a schematic of a long wavelength InP based VCSEL structure with two oxidation steps for the InAlAs/InP DBRs and one step for the InAlAs current confinement layer. Due to the critical oxidation depth for the confinement layer, this oxidation should be the last one. Conducting InP layers are inserted between the mirrors and the cavity to form a current path

into the gain region for intra-cavity contacts. On the way to realize this structure it is necessary to investigate the oxidation characteristics of $In_{0.52}Al_{0.48}As$ layers lattice matched to InP.

We used epitaxial grown $In_{0.52}Al_{0.48}As/(In_{0.53}Ga_{0.47}As)_{0.7}(In_{0.52}Al_{0.48}As)_{0.3}$ Bragg reflectors for the first test runs. The total thickness is almost 4.8 μm. The layers are oxidized after wet etching of 3.2-μm-deep ridges. We determine the vertical oxidation rate between the stripes and the lateral oxidation rate of the high and low Al content material by looking at the oxidation fronts of cleaved facets in a scanning electron microscope (SEM).

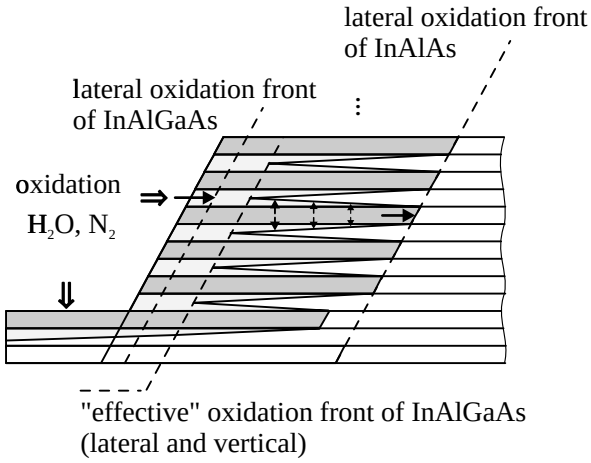

Fig. 5: Ratio of lateral and vertical oxidation rate in DBRs near at the side wall of a etched stripe structure.

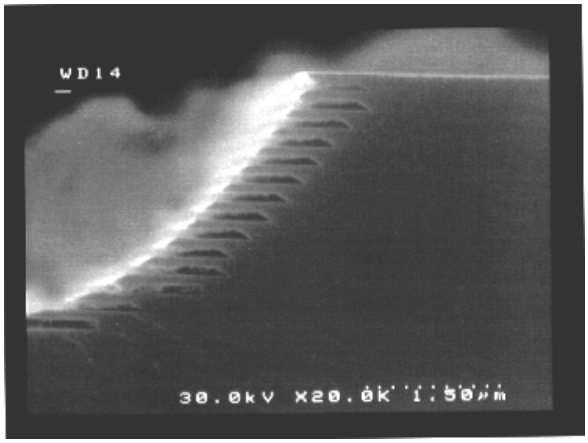

Fig. 6: Scanning electron microscope image of an oxidized $In_{0.52}Al_{0.48}As/(In_{0.53}Ga_{0.47}As)_{0.7}$-$(In_{0.52}Al_{0.48}As)_{0.3}$ Bragg reflector.

Fig. 5 shows a schematic of the oxidized ridge structure. Layers with low Al content have a lower oxidation rate than layers with high Al content. The vertical oxidation starts at layers with high Al content and continues at layers with lower Al content. Thus, layers with a low Al content exhibit a larger effective oxidation rate than without additional vertical oxidation. This effect can be utilized to increase the effective oxidation speed by incorporating a thin layer with high Al content. In the SEM image of Fig. 6 we see the oxidation fronts of the DBR after oxidizing the sample at 520 °C for two hours.

Fig. 7 shows the oxidation rate for lattice matched $In_{0.52}Al_{0.48}As$ at different oxidation temperatures. We have to take into consideration, that the growth temperature of the structure was 520 °C. Determining the lateral oxidation rate r by fitting to the usual approximation,

$$r = r_0 e^{\frac{-E_a}{kT}}, \tag{1}$$

gives a r_0 value of 162.2×10^9 nm/h and an activation energy E_a =1.326 eV. For comparision a 27 nm thick AlAs layer ($x_{Al} = 100\%$) has a 48 times larger r_0 value of 7.75×10^9 μm/h and an activation value of 1.31 eV [10]. The vertical oxidation rate of a 2-μm-thick AlGaAs layer with an Al content of 48% shows an oxidation rate of about 10 nm/min at T_{ox} = 520 °C. The oxidation rate has in simple consideration only a dependence of Al content and is independent of the material. We seems to have indeed to notice that the horizontal oxidation speed is about 1.5 times higher than the vertical oxidation speed.

To accelerate the oxidation rate of $\lambda/4$ InAlAs layers in Bragg reflectors for VCSELs, it could be helpful to grow a thin AlAs layer between two $\lambda/8$ InAlAs layers. The fast lateral oxidation rate of the film could also accelerate the lateral oxidation rate of the thick layer with lower Al content because of the additional vertical rate.

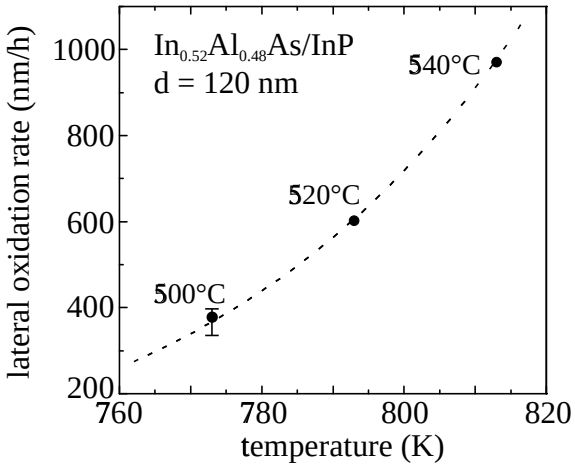

Fig. 7: Linear plot of the lateral oxide thickness vs. oxidation temperature of a 120-nm-thick $In_{0.52}Al_{0.48}As$ layer.

References

[1] T. Baba, Y. Yogo, K. Suzuki. F. Koyama, and K. Iga, "Near room temperature continous wave lasing characteristics of GaInAsP/InP surface emitting laser," *Electron. Lett.*, vol. 29, pp. 913-914, 1993

[2] K. Uomi, S.J.B. Yoo, A. Scherer, R. Bhat, N.C. Andreadakis, C.E. Zah, M.A. Koza, and T.P. Lee, "Low threshold, room temperature pulsed operation of 1.5-μm vertical-cavity surface-emitting lasers with an optimized multi-quantum well active layer," *IEEE Photon. Technol. Lett.*, vol. 6, pp. 317-319, 1994

[3] D.I. Babic, J.J. Dudley, K. Streubel, R.P. Mirin, B.I. Miller, J.E. Bowers, and E.L. Hu "Double-fused 1.52 μm vertical-cavity lasers," *Appl. Phys. Lett.*, vol. 66, no. 9, pp. 1030-1032, 1995

[4] D.I. Babic, K. Streubel, R.P. Mirin, N.M. Margalit, J.E. Bowers, and E.L. Hu, "Room-temperature continous-wave operation of 1.54-μm vertical-cavity lasers," IOOC 1995, PDI-5, Hongkong

[5] E.D. Palik, Handbook of Optical Constants of Solids, Academic Press Inc., p. 571, 1985

[6] P. Yeh, Optical Waves in Layered Media, John Wiley & Sons, New York, 1988

[7] K.L. Lear, K.D. Choquette, Jr., S.P. Kilcoyne, and K.M. Geib, "Selectively Oxidized Vertical Cavity Surface Emitting Lasers with 50% Power Conversion Efficiency," submitted to Electron. Lett.

[8] S.J. Caracci, M.R. Krames, N. Holonyak, Jr., M.J. Ludowise, and A. Fischer-Colbrie "Long wavelength ($\lambda \approx 1.5$ μm native-oxide-defined InAlAs-InP-InGaAsP quantum well heterostructure laser diodes," *J. Appl. Phys.*, vol. 75, no. 5, pp. 2706-2708, 1994

[9] M.H. MacDougal, G.M. Yang, A.E. Bond, C.K. Lin, D. Tishinin, and P.D. Dapkus, "Electrically-pumped vertical-cavity lasers with Al_xO_y/GaAs reflectors," submitted to Photon. Technol. Lett.

[10] M. Grabherr, B. Weigl, "Selective Oxidation of AlGaAs Layers," annual report, Department of Optoelectronics, University of Ulm, 1995

Fabrication of High-Power InGaAs/AlGaAs Strained-Layer Quantum-Well Lasers

Georgi Stareev, Gernot Reiner

We have fabricated high-power InGaAs/AlGaAs strained-layer lasers containing two $In_xGa_{1-x}As$ (x=0.2) quantum wells separated by GaAs barriers. The layer structure was grown in a Molecular Beam Epitaxy (MBE) reactor. Using a simple metal-stripe device under pulse operation, we achieved an output power of 840 mW per facet and a total differential efficiency of 67 % at a temperature of 25° C. The laser facets were uncoated and broad-area dies (50 μm × 500 μm) emitting at 996 nm were tested under a needle probe without bonding on heatsinks. The threshold current density J_{th} was about 350 A/cm^2 for diodes with a cavity length L = 500 μm. For continious wave (cw) operation, it was sufficient to reduce the stripe width under 20 μm. The obtained maximum cw output power was 32 mW per facet, limited by temperature rise. The corresponding operating current was 210 mA. The high-power capabilities of the structures demonstrate their potential as sources for pumping of solid-state lasers and for applications in laser amplifiers.

1. Introduction

Many efforts have been devoted to the fabrication of laser diodes which exhibit high power, low threshold current density, improved power conversion efficiency and stable temperature characteristics. High performance semiconductor lasers have drawn considerable attention as compact sources for optical pumping of rare-earth ions in solid-state lasers or fiber amplifiers. Strained quantum-well InGaAs/AlGaAs lasers are well suited for such applications because the emission wavelength can be extended to 1.1 μm, compared with the long-wavelength limit of nearly 0.9 μm for lattice-matched GaAs/AlGaAs quantum-well lasers. The compressive strain appearing in the active InGaAs layer should decrease the effective density of states in the valence band, thus leading to lower threshold current densities. Recently, the expected reduction of the J_{th} was corroborated experimentally [1]. The ridge waveguide laser has already proven to be a structure which yields high performance, especially concerning maximum powers [2]. A significant problem to be solved in high-power operation is the facet degradation which is attributed to optical absorption at the mirror surface. Large spot sizes are required in order to lower the optical power density on the facet. Usually, the lasers are patterned into index-guided devices where the ridge is etched deeply enough to minimize both, the optical antiguiding in the system and the current spreading. Optimum performance requires that the distance from the bottom of the ridge to the active layer has to be controlled precisely [3].

2. Laser Structure

The device used in this study is a GRaded INdex Separate Confinement Heterostructure (GRIN-SCH). The InGaAs/AlGaAs structure was grown on Si-doped n^+-GaAs (100)-substrates using MBE. The device configuration, as shown schematically in Fig. 1, consists of the following layers: a 100-nm-thick n-GaAs buffer layer, a 1-μm-thick n-$Al_{0.47}Ga_{0.53}As$ cladding layer with

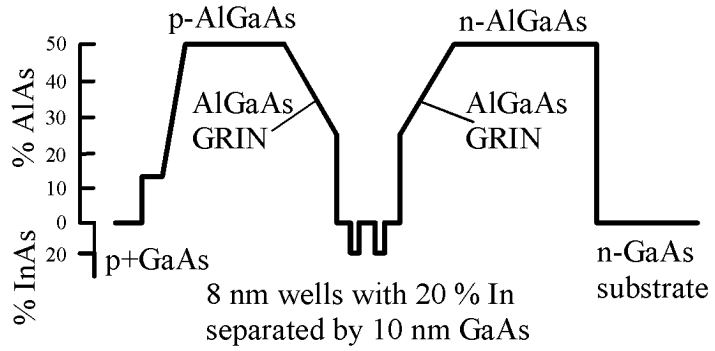

Fig. 1: Structure of InGaAs/AlGaAs graded-index separate-confinement heterostructure quantum-well laser.

a donor concentration of 5×10^{17} cm^{-3}, a 250-nm-thick $Al_yGa_{1-y}As$ confining layer (y linearly graded from 0.47 to 0.11), an active layer containing two 8-nm-thick InGaAs quantum wells, each of them surrounded by 10-nm-thick GaAs barriers, then another 250-nm-thick GRIN layer (compositionally transformed from $Al_{0.11}Ga_{0.89}As$ to $Al_{0.47}Ga_{0.53}As$), a p-type $Al_{0.47}Ga_{0.53}As$ cladding layer with a thickness of 1 μm and doping concentration of 5×10^{17} cm^{-3}, a 150-nm-thick graded p-$Al_yGa_{1-y}As$ layer (y linearly graded from 0.47 to 0.11) and a 300-nm-thick Be-doped (p=10^{20} cm^{-3}) contact layer.
The substrate temperatures used for growing the InGaAs and AlGaAs epilayers were specified on the basis of morphology and photoluminescence studies performed on test samples. The GaAs buffer layer and n-AlGaAs layers were grown at 650°C. The growth temperature of the InGaAs active layer was 500°C. The temperature raised to 650°C for growth of the upper AlGaAs layers. Finally, the p^+-GaAs cap layer was grown at 400°C, because this temperature was optimal for growing highly doped contact layers.

3. Device Fabrication

The processing of the ridge waveguide lasers was carried out as follows. In the first step Ti/Pt/Au stripes with variable sizes on 100 μm centres were deposited on the p^+-GaAs by means of evaporation and liftoff. Prior to the metal deposition, the GaAs surface was cleaned by bombardment with low energy (60 eV) Ar^+ ions for 40 s according to the procedure described elsewhere [4]. It has been shown, that this treatment radically improved the quality of the ohmic contacts. During the formation of the index-guided structure, the as-deposited metal stripes surve as a mask and both, the p^+-GaAs contact layer and the p-AlGaAs cladding layer, were removed between the contacts. The wet chemical etching was chosen for the definition of the ridge. This technique is simple but does not allow a good control of the etch depth. The process was carried out using H_2SO_4:H_2O_2:H_2O solution and the etching was finished after removing of the upper cladding layer. Afterwards, the laser samples were thinned from the substrate side to about 100 μm by polishing in a Br-methanol solution. AuGeNi ohmic contacts were deposited on this side and formed at 400°C for 40 s. Another advantage of this rapid thermal processing is that the upper Ti/Pt/Au contact also undergoes an effective annealing that improves the ohmic behavior. The device architecture was completed by cleaving of Fabry-Perot resonators with definite lengths.

4. Laser Characteristics

The laser characterization was carried out by probing individual devices on the bar in the junction-side-up configuration without mounting or active cooling. The devices oscilate in multiple longitudinal modes. Room-temperature electroluminescence spectra show that the structures are matched for operation with wavelengths in the range from 980 to 1000 nm. The lasers prepared in the form of uncoated dies with cavity lengths of 500 μm exhibit a lasing wavelength of 996 nm. It has been demonstrated [5] that the laser spectrum can be tuned to longer wavelengths if larger cavity lengths or facets with reflection coatings are used. On the other hand, antireflection coatings shift the spectrum to shorter wavelengths. Figure 2 shows a typical power-current relationship for 50 μm-wide index-guided lasers. During the measurements, the diodes were driven by 1 μs current pulses with a duty cycle of 0.1 %. A typical power output of 840 mW per facet was obtained from 500 μm long stripes. The power value was limited by the maximum current of 2 A available from the pulser.

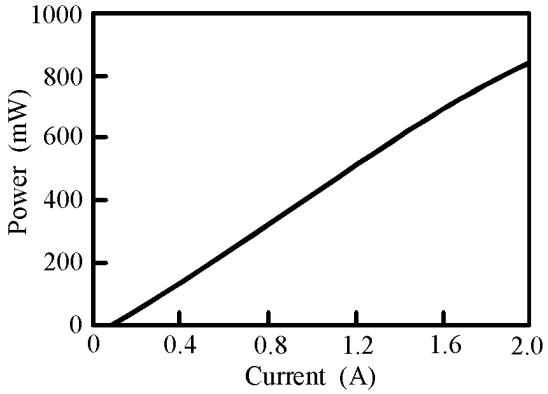

Fig. 2: Power-current data for 50-μm-wide laser under pulse operation (500μm-length, uncoated facets).

The achieved power levels are comparable to those obtained in high-power InGaAs/AlGaAs devices mounted on heatsinks [2]. The broad-stripe lasers exhibit threshold current densities of 350 A/cm^2. This value is relatively low taking into account that the etch depth was not strictly controlled. Since a spreading part of the bias current occurs under the ridge, the structures can still be optimised. Even higher performances could be attained by introducing coating processes. The lasers exhibit high differential quantum efficiences of about 67 % that are no worse than those obtained in high-quality InGaAs/AlGaAs lasers [5]. Typical room temperature *cw* power against injection current characteristics of as-cleaved devices with 20-μm-wide and 500-μm-long cavity lengths are shown in Fig.3. The thermal saturation limits the maximum *cw* power to 32 mW per facet. The threshold current and the maximum *cw* current are 50 mA and 210 mA, respectively. With increasing I the output power initially increases, but then decreases because junction heating enhances the carrier leakage and thus reduces the differential quantum efficiency. Measurements of current-voltage characteristics show that our MBE-grown diodes have a differential series resistance R_C in the range of 1.9 to 2.4 Ω. This values are several times larger than those in optimised lasers with a similar band diagram and geometry [2]. The higher

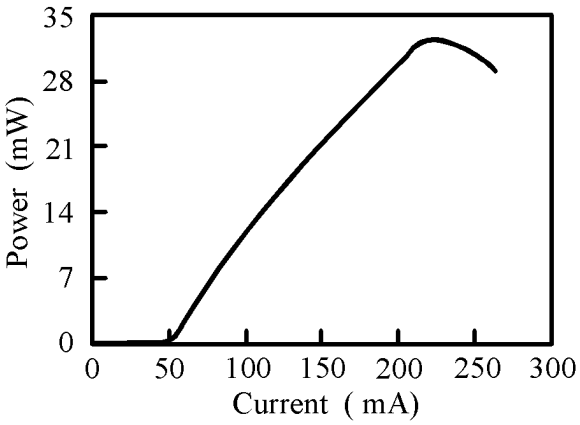

Fig. 3: Continuous wave curve of optical power against drive current for 20-μm-wide laser.

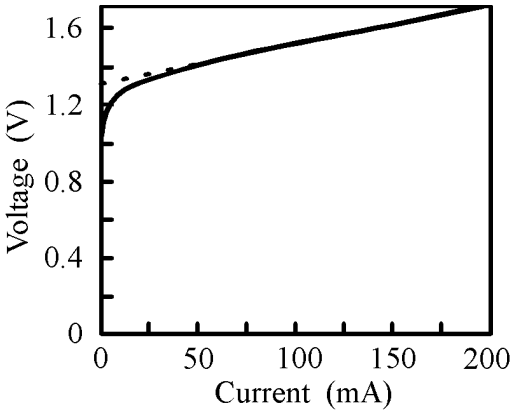

Fig. 4: Typical current-voltage characteristic of the laser diodes.

R_C values in our case can be attributed to parasitic resistivities eappearing at the heterojunctions, while the resistivity of the contacts is believed to be negligible. In fact, as can be seen in Fig. 4, the current-voltage characteristic gives a relatively low intercept value of 1.32 V. It should be possible to achieve significantly higher *cw* powers by decreasing the series resistance and by modifying the diode construction in order to reduce the dissipation losses.

5. Conclusions

The design, fabrication, and characteristics of strained layer InGaAs/AlGaAs quantum well lasers are described. We grew the laser on an n^+-GaAs substrate by one-step MBE. Graded-index AlGaAs layers were used to increase the light confinement. We demonstrate, that following simple processing, it is possible to fabricate devices designed for high-power operation. We achieved high-power levels under pulsed operation (840 mW per facet). For all that, no mirror coatings were applied to the diodes. A rapid test of the wafer homogeneity was performed by recording light-current characteristics for various diode stripes along a cleaved bar. Though the heating of the devices plays a considerable role in the junction-up configuration used, the obtained *cw* power output in 20-μm-wide structures is 32 mW per facet. Differential quantum efficiencies of 67 % have been estimated in relatively short-cavity (500 μm) ridge waveguide lasers tested in the junction-side up configuration. A further decrease of the diode series resistance is necessary to reduce the spontaneous Joule energy dissipation and to achieve less thermally limited *cw* characteristics. We believe that the simple ridge formation described in this work may be useful to realize high-power laser diodes with excellent characteristics.

References

[1] H.K. Choi, C.A. Wang, "InGaAs/AlGaAs strained single quantum well diode lasers with extremely low threshold current density and high efficiency," *Appl. Phys. Lett.*, vol. 57, pp. 321-323, July 1990.

[2] C.A. Wang, H.K. Choi, J.N. Walpole, G. A. Evans, W.F. Reichert, W. W. Chow, C. T. Fuller, " High-power, high-temperature InGaAs/AlGaAs strained-layer quantum-well diode lasers," *Electron. Lett.*, vol. 30, pp. 646-648, April 1994.

[3] B. Elman, W.F. Sharfin, F.D. Crawford, W.C. Rideout, J. Lacourse, R.B. Lauer, " High power 980 nm ridge waveguide lasers with etch-stop layer," *Electron. Lett.*, vol. 27, pp. 2032-2033, October 1991.

[4] G. Stareev, "Formation of extremely low resistance Ti/Pt/Au ohmic contacts to p-GaAs," *Appl. Phys. Lett.*, vol. 62, pp. 2801-2803, May 1993.

[5] J.S. Major, Jun., W.E. Plano, D. F. Welch, D. Scifres, "Single-mode InGaAs/GaAs laser diodes operating at 980 nm," *Electron. Lett.*, vol. 27, pp. 539-540, March 1991.

Improved Method to Determine the Gain of Strained InGaAs Quantum-Well Lasers and Amplifiers

Jörg Heerlein, Stefan Morgott, Günter Jost

Exact spectral gain measurements on laser diodes and laser amplifiers are presented using a correction method to minimize measurement errors caused by the finite resolution of the spectrometer. For an optimization of laser diodes and laser amplifiers with respect to high efficiencies and high output power, it is necessary to determine the spectral gain coefficient of the devices as exact as possible. Especially for amplifiers we get information about the figures of merit like spectral width, efficiency, and gain $G = P_{out}/P_{in}$. The spectral gain characteristics can be evaluated by measuring the optical intensity spectrum below the laser threshold. Two very common methods are known from Hakki-Paoli and Cassidy. Both techniques will be introduced and discussed concerning their accuracy with respect to the resolution of the measurement system, the mode gain and the free spectral range FSR. We show that it is possible to achieve exact results of the "real" mode gain despite of the finite resolution. For that reason we have simulated the measurement of the Fabry-Perot spectrum. It will be shown that it is possible to calculate the real spectral gain with the knowledge of the relative error. This correction method is used here to characterize InGaAs quantum-well laser diodes and amplifiers.

1. Introduction

The optical spectral mode gain g_m of a laser diode or amplifier supplies many important information like threshold current, lasing wavelength, spectral width, efficiency and gain $G = P_{out}/P_{in}$. Further presented methods for the determination of the mode gain g_m appropriates the intensity undulation of the Fabry Perot (FP) modes. A very common method was introduced by Hakki and Paoli [1]. This method will be denoted as Hakki-Paoli method throughout this report. The Hakki-Paoli method requires the measurement of the maxima ($\pi\lambda/FSR = m\pi$) and minima ($\pi\lambda/FSR = (2m+1)\pi$) of the longitudinal FP modes. The ratio of maximum to minimum intensity gives the signal gain undulation ν which can also be expressed by the following equation using the single-pass gain G_s and the reflectivity of both facets R_1, R_2.

$$\nu = \frac{I_{max}}{I_{min}} = \left(\frac{1 + \sqrt{R_1 R_2} G_s}{1 - \sqrt{R_1 R_2} G_s} \right)^2 \tag{1}$$

The mode gain g_m is then given by

$$g_m = \alpha_i + \frac{1}{2L} \ln \left(\frac{1}{R_1 R_2} \right) + \frac{1}{L} \ln \left(\frac{\sqrt{\nu} - 1}{\sqrt{\nu} + 1} \right). \tag{2}$$

The last term is often called net mode gain $g_{m,net}$. The net mode gain is equal to the mode gain less intrinsic and mirror losses.

$$g_{m,net} = \frac{1}{L} \ln \frac{\sqrt{\nu} - 1}{\sqrt{\nu} + 1} \begin{cases} g_{m,net} = 0 & \text{for} \quad i \geq i_{th}, \\ g_{m,net} < 0 & \text{for} \quad i < i_{th} \end{cases} \tag{3}$$

At lasing threshold, all losses are compensated and the net mode gain $g_{m,net}$ becomes zero. With decreasing operating current the net mode gain $g_{m,net}$ decreases. This indicates, that the net mode gain $g_{m,net}$ is negative below lasing threshold.

Cassidy showed a modified determination of the gain from the spectrum [2]. Instead of using minimum and maximum intensity Cassidy uses the average mode intensity $< I >$ and the minimum intensity I_{min}.

$$\chi = \frac{< I >}{I_{min}} = \frac{1 + R_1 R_2 G_s^2}{1 - R_1 R_2 G_s^2} \tag{4}$$

For the net mode gain $g_{m,net}$ we can write now

$$g_{m,net} = \frac{\chi - 1}{\chi + 1} \tag{5}$$

To take a comparison of these methods we have to keep in mind that the resolution of a monochromator is finite. This means that not a discrete wavelength but a defined spectral width $\Delta\lambda$ is detected. For a calculation of the detected signal the resolution has to be taken into account as a rectangular response function $D(\lambda)$.

$$D(\lambda) = \begin{cases} 1 & \text{for } -\Delta\lambda/2 \leq \lambda \leq \Delta\lambda/2, \\ 0 & \text{else.} \end{cases} \tag{6}$$

The spectrum measured by the system $P_{meas}(\lambda)$ can be written as:

$$P_{meas}(\lambda) = \frac{1}{\Delta\lambda} \int_{-\infty}^{+\infty} P_{in}(\lambda') D(\lambda' - \lambda) d\lambda'. \tag{7}$$

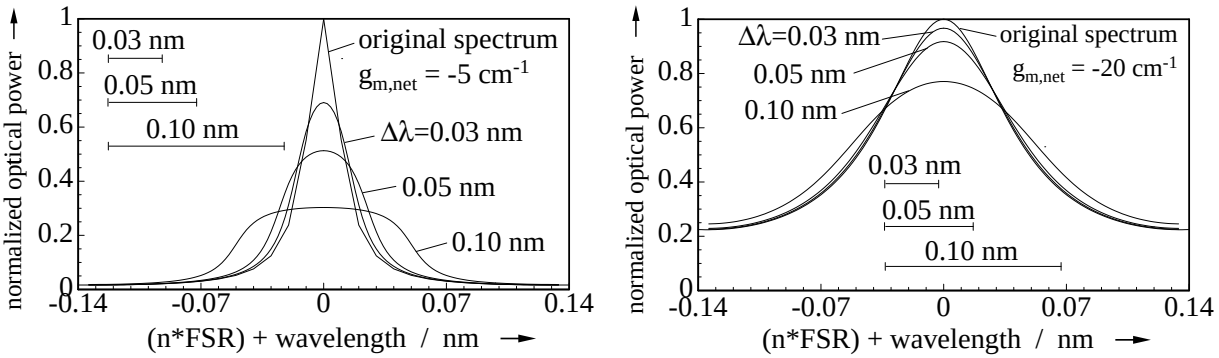

Fig. 1: Calculated input and output spectra about one FSR (0.27 nm) for different wavelength resolutions $\Delta\lambda$ of the measurement system and different values of net mode gain (a) $g_{m,net} = -5\,\mathrm{cm}^{-1}$ (b) $g_{m,net} = -20\,\mathrm{cm}^{-1}$. The horizontal bars indicate the different resolutions of the monochromator

Fig. 1 shows the influence of the monochromator resolution on the measured longitudinal mode. As the wavelength resolution decreases ($\Delta\lambda$ increases), the mode peak starts to flatten up while the valleys change slightly since the minima are defined through some more points. Only far below threshold the deviation is distinct. The comparison between different net mode gains $g_{m,net}$ shows their strong influence on the shape of the mode. With decreasing $g_{m,net}$ the mode broadens and the ratio of I_{max} to I_{min} changes less.

For the calculation of the net mode gain with the Hakki-Paoli method, the maximum intensity is divided by the average of the neighbored minima. Therefore, only three points are used. With the Cassidy method, all measured points n in the FSR are added and then divided by the average of the neighboring minima. For the Cassidy method the signal-noise ratio is about $\sqrt{n}$ better than for the Hakki-Paoli method. The S/N ratio becomes higher with decreasing step width and therefore increasing number of measured points. A further enhancement with regard to the S/N ratio delivers the modified Cassidy method [3]. Cassidy proposed to estimate the minimum intensity by averaging over a certain wavelength interval.

2. Simulation

For the simulation of the relative error of the determinated gain we have compared the input spectrum with the output spectrum of the spectrometer. The original spectrum is given by the transmission function T

$$T(\lambda) = \frac{(1-R_1)(1-R_2)G_s}{(1-\sqrt{R_1R_2}G_s)^2 + 4\sqrt{R_1R_2}G_s \sin^2(\frac{\pi\lambda}{FSR})} \tag{8}$$

and the single pass gain G_s

$$G_s = \exp\left((g_m - \alpha_i)L\right) = \exp\left(g_{m,net}L + \frac{1}{2L}\ln\left(\frac{1}{R_1R_2}\right)\right). \tag{9}$$

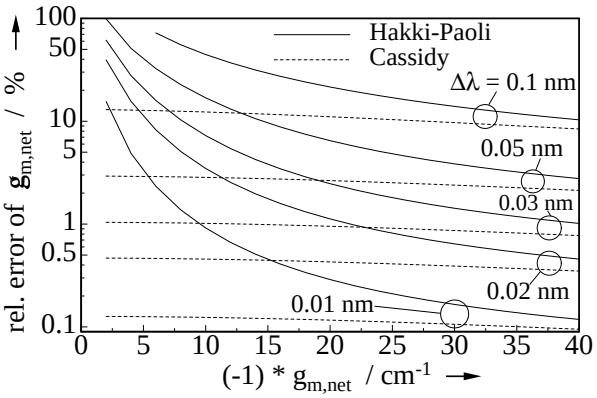

Fig. 2: Relative error of the determinated net mode gain as a function of net mode gain with the resolution $\Delta\lambda$ as parameter and a FSR of 0.27 nm

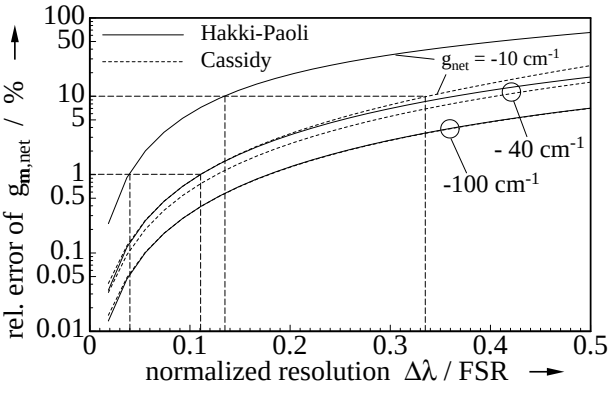

Fig. 3: Relative error of the determinated net mode gain as a function of normalized wavelength resolution with the net mode gain as parameter

Therefore the knowledge of the intrinsic losses α_i is not necessary. To simulate the plotted spectrum, the value of the wavelength resolution $\Delta\lambda$ is required. The step width s of the measured system has been neglected. Some experiments have shown that $s \leq \frac{1}{20}\Delta\lambda$ is necessary to neglect the error caused by the finite small step width. Fig. 2 shows the relative error of the net mode gain in % with the limited wavelength resolution $\Delta\lambda$ as parameter. The FSR is about 0.27 nm for an $In_{0.2}Ga_{0.8}As$ laser with an emission wavelength of 980 nm ($L = 500\ \mu$m and $n_{eff} = 3.6$). Obviously the evaluated net mode gain is always lower than the input net mode gain. If $g_{m,net}$ approximates to the laser threshold ($g_{m,net} = 0$), the relative error of the Hakki-Paoli method increases stronger compared to the Cassidy method. Especially for a current near

the laser threshold, the Cassidy method should be preferred. In Fig. 3 the relative error of $g_{m,net}$ as a function of the normalized wavelength resolution for different $g_{m,net}$ is depicted.

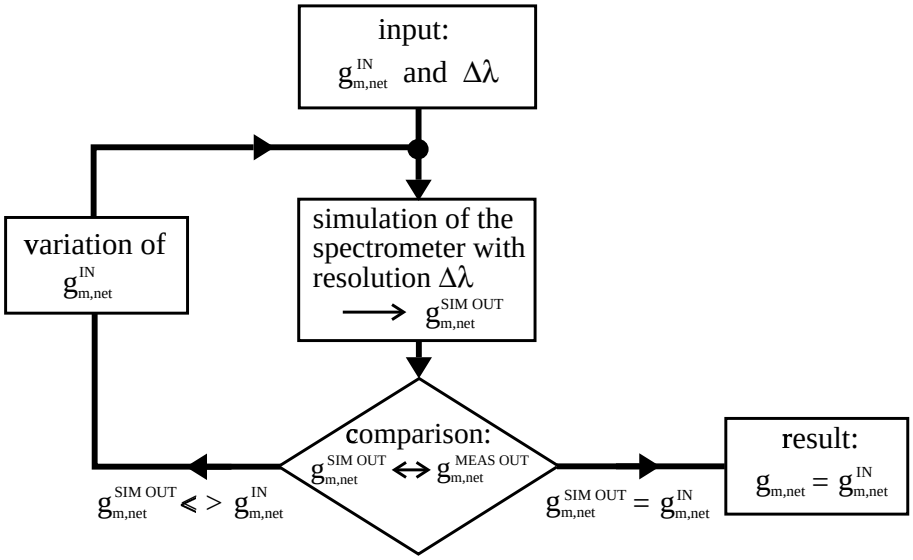

Fig. 4: Flow diagram for the correction of the measured net mode gain

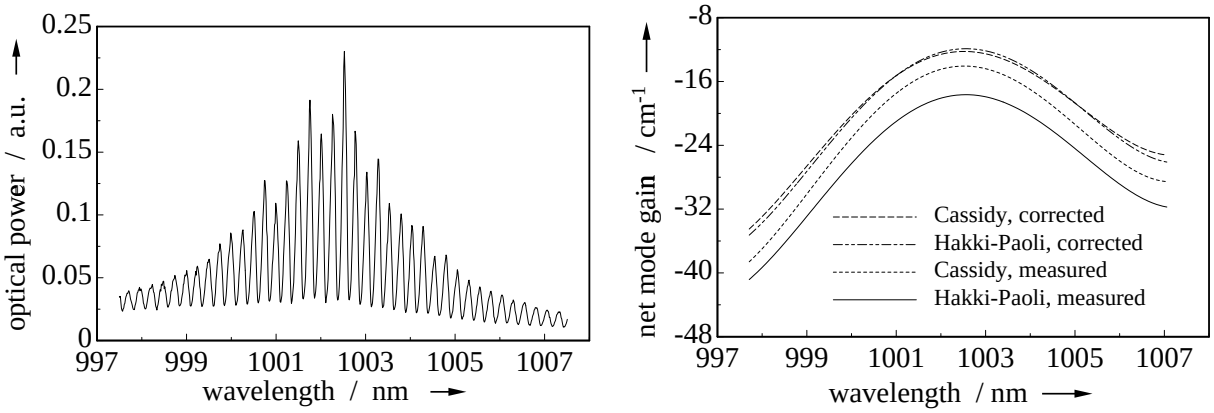

Fig. 5: (a) Spectrum of a double quantum-well laser near laser threshold and (b) the corresponding measured and corrected gain curves

3. Correction of the Measured Gain Curve

Using this simulation, it is possible to calculate the "real" gain curve. Fig. 4 shows the flow diagram for this calculation. Using equation (8), a FP spectrum with a start value of the input net mode gain $g^{IN}_{m,net}$ is calculated. Afterwards, the output net mode gain $g^{SIM\ OUT}_{m,net}$ of the measured system with the known wavelength resolution $\Delta\lambda$ is simulated and compared with the measured net mode gain $g^{MEAS\ OUT}_{m,net}$. Then, $g^{IN}_{m,net}$ will be varied until $g^{SIM\ OUT}_{m,net}$ and $g^{MEAS\ OUT}_{m,net}$ are equal. Calculations using the Hakki-Paoli or Cassidy method should yield identical results.

Fig. 5 shows an example of such a corrected gain deviation. In Fig. 5a, the optical spectrum of a double quantum-well $In_{0.2}Ga_{0.8}As$ laser diode is depicted. The net mode gain spectrum calculated with the Hakki-Paoli method is about $4\,cm^{-1}$ less than the values obtained by the Cassidy method. Furthermore, the corrected spectra are plotted into the diagram of Fig. 5b. It is obvious that the corrected spectra of both methods show nearly the same results.

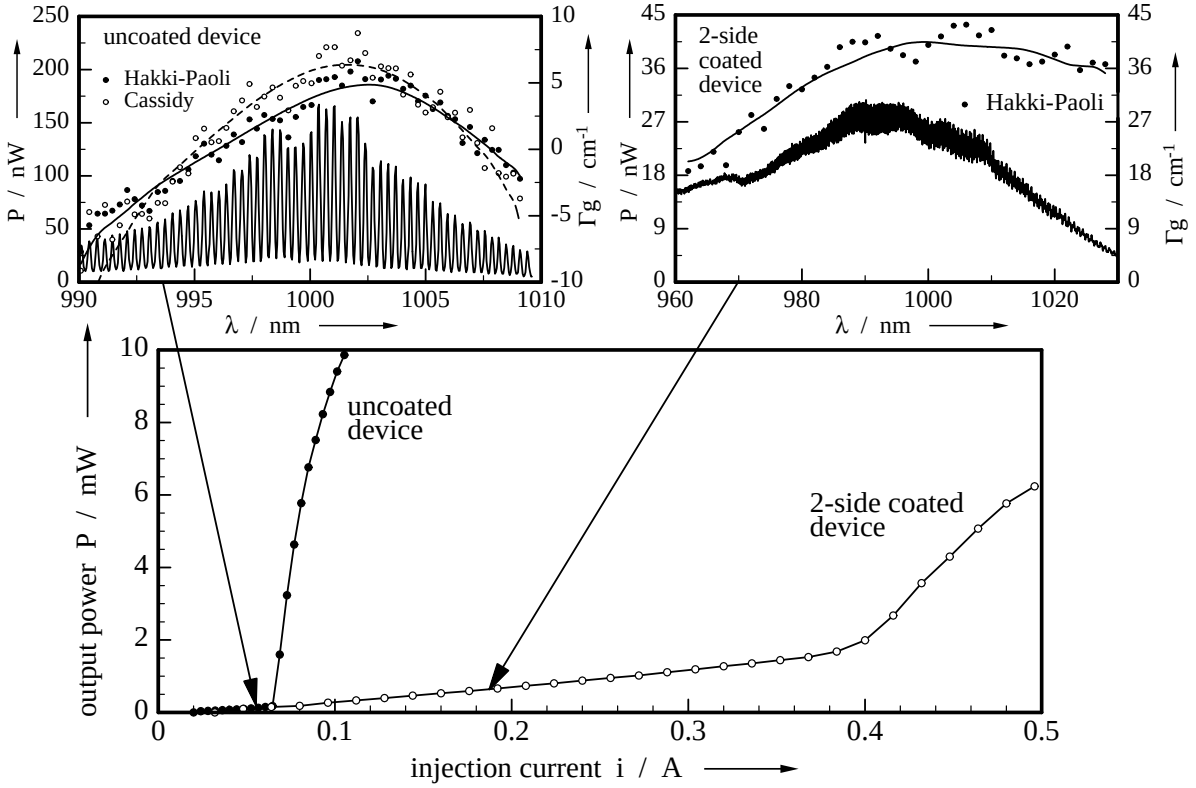

Fig. 6: Spectra, gain curves and optical output characteristic of a laser diode and a two-side AR-coated laser amplifier

Furthermore, it is possible to determine the residual reflectivities of an anti-reflection (AR) coated laser diode with the knowledge of the exact undulation of the FP spectrum and the reflectivity of the uncoated facet R. The residual reflectivity R^* is given by:

$$R^* = \frac{\sqrt{\nu} - 1}{\sqrt{\nu} + 1} R \tag{10}$$

or with Cassidy method:

$$R^* = \frac{\sqrt{\chi} - 1}{\sqrt{\chi} + 1} R \tag{11}$$

when the bias current is equal to the threshold current of the device with uncoated facets [4]. Fig. 6 shows a comparison between the spectra of a laser diode (uncoated device) and an amplifier (AR-coated device). The arrows show the operating points in the output characteristics, where

the spectral gain has been determined. For a three times higher operating current the mode gain increases by about $35\,\mathrm{cm}^{-1}$.

References

[1] B.W. Hakki, T.L. Paoli, "Gain spectra in GaAs double-hetrostructure injection lasers," *J. Appl. Phys.*, vol. 46, pp. 1299-1306, 1975.

[2] D.T. Cassidy, "Technique for measurement of the gain spectra of semiconductor diode lasers," *J. Appl. Phys.*, vol. 56, pp. 3096-3099, 1984.

[3] V. Jordan, "Gain measurement of semiconductor laser diodes: requirements for the wavelength resolution and sensitivity to noise," *IEE Proc. J.*, vol. 141, no. 1, pp. 13-15, 1994

[4] M. Mikulla, "Aktive Modenkopplung von AlGaAs-Halbleiterlaserdioden," *Ph.D. thesis*, Department of Optoelectronics, University of Ulm, 1994.

Characterization of High-Power Lasers and Traveling-Wave Amplifiers

Günter Jost, Jörg Heerlein, Stefan Morgott

High-power lasers and large-active-area traveling-wave amplifiers are required for a number of applications especially for biomedical uses, free-space communication systems and pump sources for Er-doped optical fiber amplifiers. In particular, traveling-wave amplifiers can amplify optical signals without conversation into electrical signals. Laser amplifiers are based on the same principle of stimulated emission in a population inverted laser medium as laser oscillators. However, for traveling-wave amplifiers it is necessary to suppress reflections at the laser facets. Laser and amplifier structures are grown by molecular beam epitaxy (MBE). Using an automatic setup, we have characterized laser diodes under CW and pulsed operation. Characteristics of broad-area amplifiers have been measured by an experimental setup with an astigmatic optic to achieve effective coupling between the traveling-wave amplifier and the beam of a Ti:sapphire laser.

1. Introduction

Strained-layer InGaAs/GaAs quantum-well laser structures are attractive light sources for high-power lasers and broad-area traveling-wave amplifiers. Graded-index seperate-confinement heterostructure quantum-well structures (GRIN-SCH) have been grown by molecular beam epitaxy (MBE) on n-doped GaAs substrates. A typical composition profile with two strained InGaAs quantum wells is shown in Figure 1 [1].

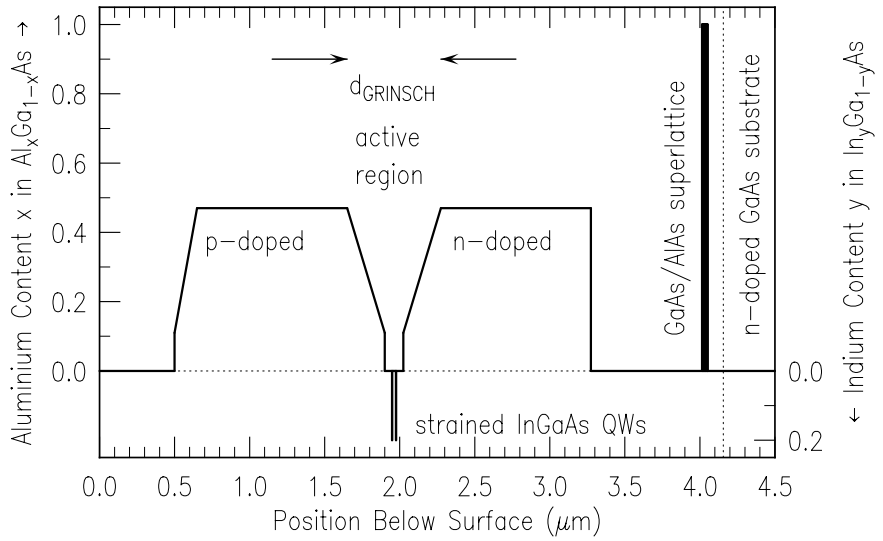

Fig. 1: Epitactical grown structure with two strained $In_{0.2}Ga_{0.8}As$ quantum wells.

The active region consists of two 8-nm $In_{0.2}Ga_{0.8}As$ quantum wells, seperated by 10-nm-thick GaAs layer and surrounded by 50-nm-thick GaAs layers. The waveguiding region of $Al_xGa_{1-x}As$ with a continuously varied Al concentration from 11 % to 47 %. The n- and p-type $Al_{0.47}Ga_{0.53}As$ cladding layers have a thickness of 1 μm. 20-μm-, 50-μm-, 100-μm- and 150-μm-wide broad-area lasers with cavity lengths between 150 μm and 1.5 mm have been fabricated and tested under pulsed and CW conditions.

2. Experimental Setup for Characterization of Laser Diodes

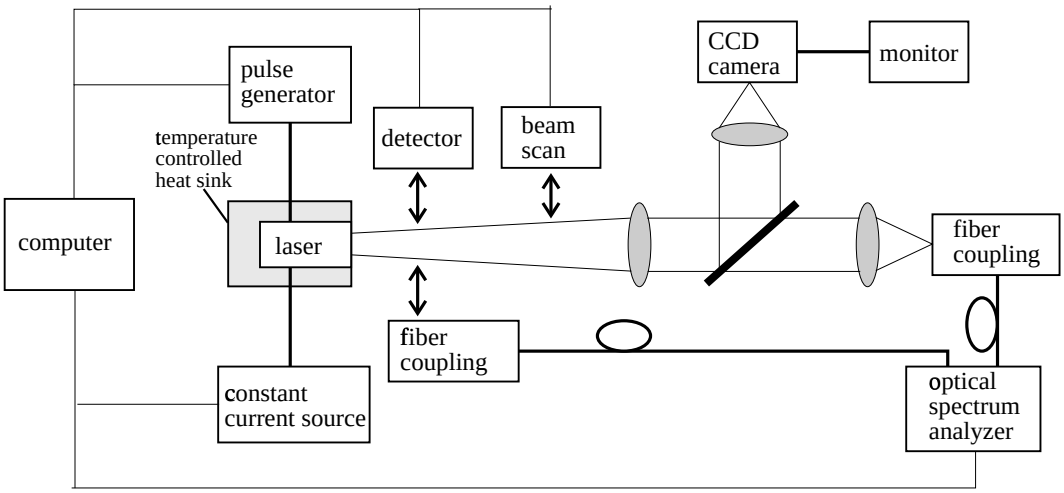

Fig. 2: Experimental setup for electrical and optical characterization of high-power laser diodes.

For standard measurements of high-power lasers, we use an automatic setup which is scetched in Figure 2. It is possible to measure the characteristic of a high-power laser diode under CW conditions up to 15 A or under pulsed conditions up to 2 A. We automatically obtain threshold current, threshold current density, differential quantum efficiency and series resistance. A magnifying optical arrangement and a CCD camera are used to monitor the condition of the laser facet and emitted near-field pattern. Furthermore we are able to measure the optical spectrum with a spectrum analyzer. The maximum wavelength resolution is 0.1 nm. The typical dependence of optical output power P_{out} and voltage V on current I is presented in Figure 3 for a 100 μm $\times$ 500 μm laser diode under CW condition. The device of Figure 3 has been mounted junction-side down on a heat sink. We obtain nearly the same characeristic for CW and pulsed operation. The threshold current of this device is 76 mA corresponding to a numerical threshold current density of 152 A/cm^2. We achieve maximum CW output power of 1.3 W at a pumping current of 1.7 A. The differential quantum efficiency is 67 % and the maximum wall-plug efficiency is 52 %

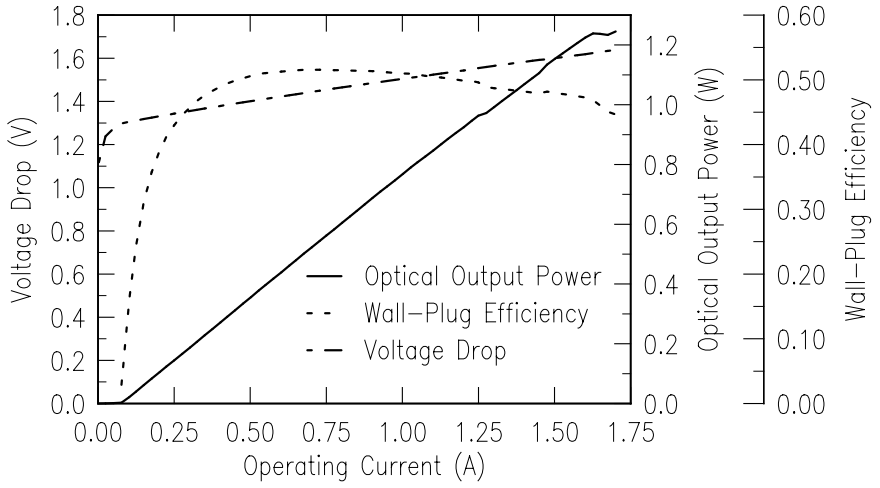

Fig. 3: Typical characteristic of a $100\,\mu$m $\times$ $500\,\mu$m laser diode under CW conditions.

3. Experimental Setup for Characterization of Traveling Wave Amplifiers

Semiconductor laser diodes with an antireflective coating on both facets can be used as traveling-wave amplifiers. Residual facet reflectivities in the range of 0.01 %-0.1 % are required to ensure reasonable high gain and small undulation in the optical spectrum[2] [3]. The operating characteristics of amplifiers are measured using an experimental setup as shown in Figure 4. As master oscillator we use a Ti:sapphire laser with a gaussian beam profil. The wavelength of this laser ranges continuously from 920 nm to 1060 nm. To achieve an appropriate input beam profil, the gaussian beam is expanded with a beam expander to approximately 4 mm FWHM. A combination of a cylindrical lens and a focusing lens is used in horizontal direction as an afocal telescope [4]. To inject a broad, gaussian shaped beam with nearly planar phase front into the active zone of the amplifier, typical cylindrical lenses with focal lengths between 6 cm and 30 cm are used, depending on the amplifier aperture. As focusing lens serves in vertical direction a lens with a numerical aperture of 0.615 and a focal length of 6.5 mm.

A schematic outline of the input is shown in Figure 5 for the vertical and horizontal beam propagation. With two CCD-cameras (Figure 4) it is possible to observe the diffraction-limited input beam of the master oscillator and the emission profil of the amplifier. The optical output spectrum of the amplifier is measured with an optical spectrum analyzer. This setup will be used for future investigations on traveling-wave amplifiers.

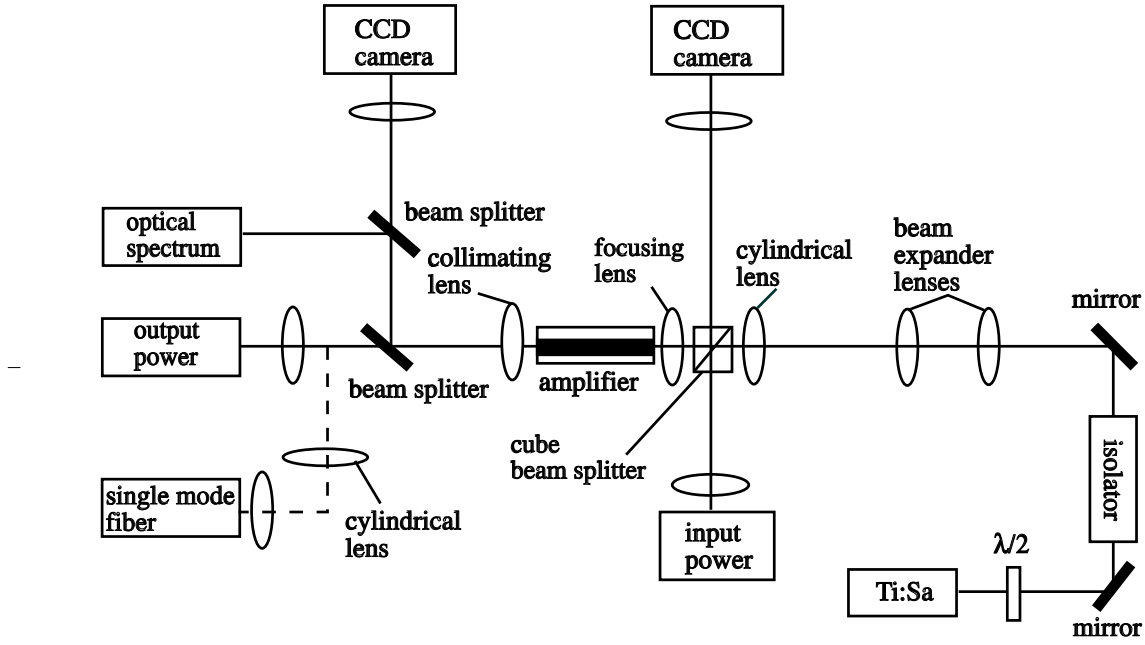

Fig. 4: Experimental arrangement to characterize traveling-wave amplifiers

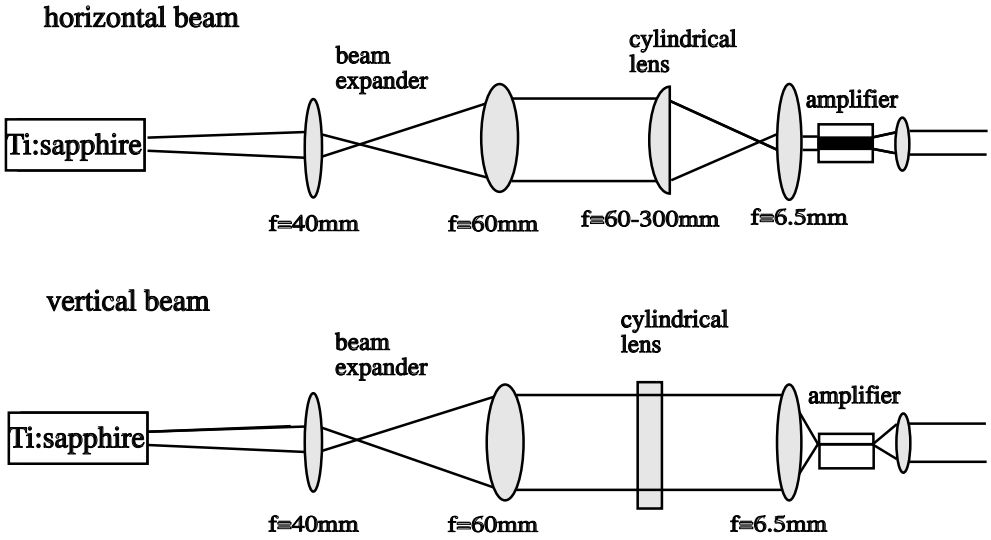

Fig. 5: Vertical and horizontal beam arrangement

References

[1] Z. Dai, J. Heerlein, G. Jost, G. Reiner, G. Stareev, P. Unger, K.J. Ebeling, "Hochleistungslaserdioden auf der Basis von InAlGaAs/GaAs", 1.Report, BMBF-project "Laser 2000", *University of Ulm*, Feb. 1995.

[2] G. Eisenstein, G. Raybon, L.W. Stulz, "Deposition and Measurement of Electron-Beam Evaporated SiO_x Antireflection Coating...," *J. Lightwave Technol.*, vol. 6, pp. 12-16, January 1988.

[3] J. Heerlein, "Fabrication of Optical Travelling-Wave Semiconductor Laser Amplifiers," *Annual Report, Department of Optoelectronics, University of Ulm 1994*, pp. 44 - 47, 1994.

[4] L. Goldberg, D. Mehuys, M.R. Surette, D.C.Hall, "High-Power, Near Diffraction-Limited Large-Area Traveling-Wave Amplifiers," *J. Quantum Electron.*, vol. 29, pp. 2028-2043, June 1993.

Beam-Profile Filamentation in High-Power Semiconductor Laser Amplification

Zheng Dai

Mechanisms of beam profile filamentation are analyzed and simulated using the beam-propagation method (BPM). Several methods are suggested to compensate the distributed thermal lens effect. The influence of the antiguiding factor on the filamentation process is intensively discussed. Unstable-cavity semiconductor laser diodes and master-oscillator power amplifiers (MOPAs) with distributed compensation structures are proposed.

1. Introduction

Beam profile filamentation has been one of the major problems of high power laser amplification. Induced index variations cause self focusing and beam-profile distortions. For semiconductor devices whose refractive indeces are more flexible, non-uniform current injection, lateral optical hole burning, non-uniform thermal effects as well as localized device defects are entangled to change the refractive indeces and to produce beam filamentation. Beam-profile shaping becomes more and more challenging. Recently, scientists from SDL had succeeded in using semiconductor for high power laser amplifications [1]. The complexity of semiconductor devices raises some new questions, but also provides some new aspects. In this paper, we use the beam-propagation method (BPM) [2, 3] to analyze beam filamentation and discuss methods to compensate the thermal lens effect and to avoid filamentation. Unstable cavity and master-oscillator power amplifier (MOPA) with distributed compensation structures are proposed.

2. Evolution of the Filamented Beams

The refractive index of optical materials is sensitive to temperature variations. Although special considerations are taken for heat dissipation, semiconductor chips still suffer from severe thermal distortions. Non-uniform heat sources produce a lateral temperature gradient and form a distributed positive lens. With a model similar to Ref. [4], we simulated the lateral temperature inhomogeneity and its impact on beam-profile distortion as shown in Fig. 1. A poor thermal conductivity produces stronger thermal response and makes the beam tend to filament.

The thermal effect is not the only reason for filamentation, also inadequate built-in index, antiguiding factor, and facet reflection can contribute to filamentation. Fig. 2 reveals the impact of an abrupt built-in lateral index variation at waveguide edge, which is frequently used for optical lateral confinement. Diffraction occurring at waveguide edges evolves its Fresnel-diffraction ripples along the amplification and causes filamentation. Since the waveguide edges are still not "hard" enough, the numbers of ripples is the Fresnel number times a reduction factor. The practical waveguide edges are more or less corrugated and their diffraction patterns are expected to be more chaotic.

Besides self focusing and diffraction at the edges, also residual facet reflection causes deterioration of the beam profile. The interference and amplification of the counter propagating beam

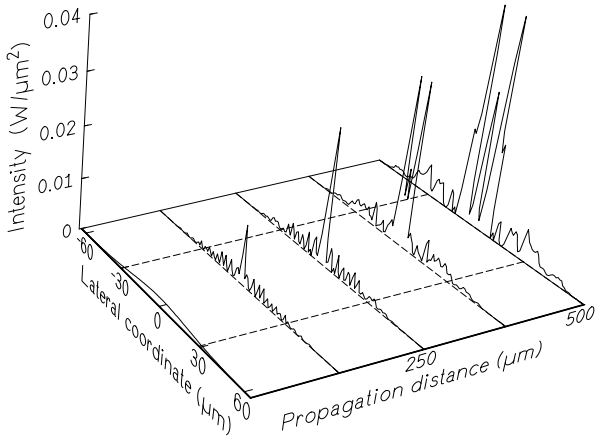

Fig. 1: Beam-profile filamentation due to thermal inhomogeneity.

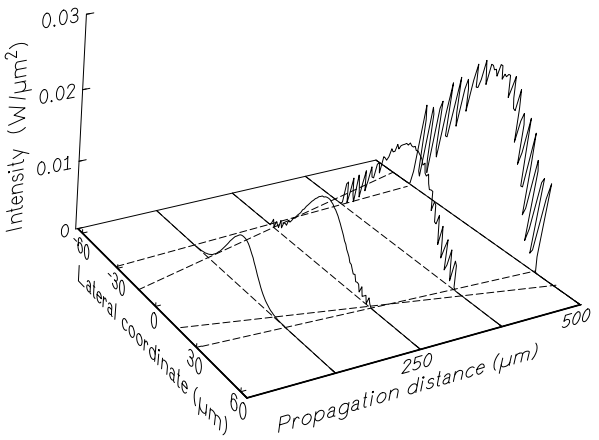

Fig. 2: Filamentation of divergent beam due to the diffraction at the edge of the waveguide.

increase the lateral inhomogeneity and lead to beam filamentation. Fig. 3 shows how small ripples caused by diffraction develop into filamentation due to a residual reflectivity of $2.5 \cdot 10^{-3}$.

Thermal lens effect, diffraction, and facet reflection are actually entangled together. Besides, antiguiding factor could also cause self focus. The combination of these factors make the problem of filamentation complicated and elusive. Once self focus occur, lateral inhomogeneity goes worse and filamentation starts collapse. In order to obtain high power amplification with good beam quality, one should remove lateral waveguide confinement, suppress the facet residual reflectivity, and compensate the thermal lens effect. Beam profile shaping should be applied before self focus dominates the transmission.

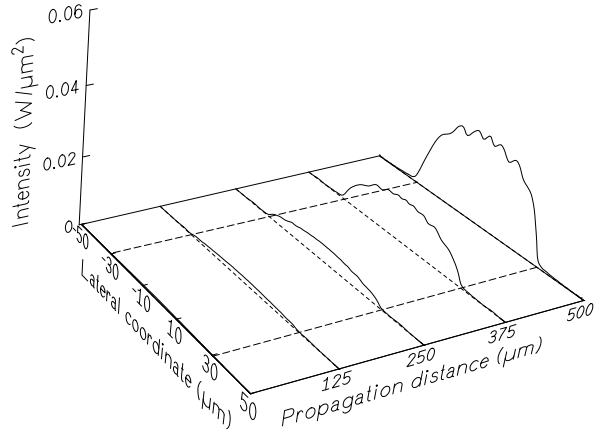

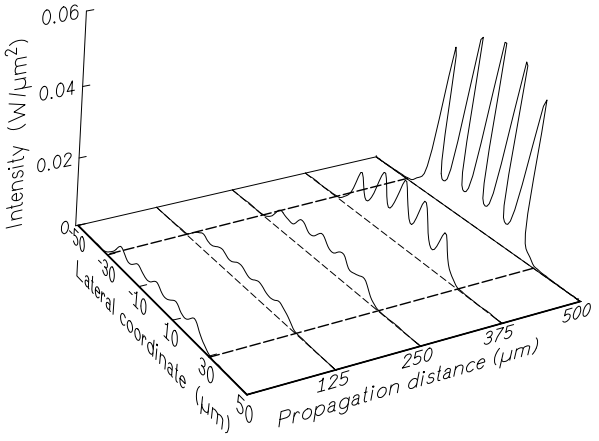

Fig. 3: Beam profile filamentation due to facet reflection. The left-hand side shows the propagation of a beam in a 60-μm-wide stripe of a laser amplifier with no residual facet reflection, whereas on the right-hand side the effect of a residual reflection of $R = 2.5 \cdot 10^{-3}$ is illustrated.

3. Compensation Mechanisms

Self focusing can be compensated by several methods. Tapered waveguide has been frequently used to generate a divergent beam. Divergent beam injection or parallel injection using a curved entrance facet have the same effect. Compared to a correction method which is distributed alang the waveguide, localized compensations are not very effective. Often, the thermal lens near the input facet is overcorrected and the thermal lens near the output is corrected insufficiently. Furthermore, localized compensations have a short effective length, while the high power amplification needs a relatively long amplification distance. The most effective way is to construct a distributed negative lens to compensate the distributed positive lens. In Fig. 4, the thermal lens is compensated by a distributed negative lens produced by a built-in index variation. Such compensation produces an satisfactory beam quality, but since the heat sources change significantly with operation conditions, a compensation of this kind has a limited operation range. Compensation of antiguiding factor having an adjustable range seems more favorable than other methods.

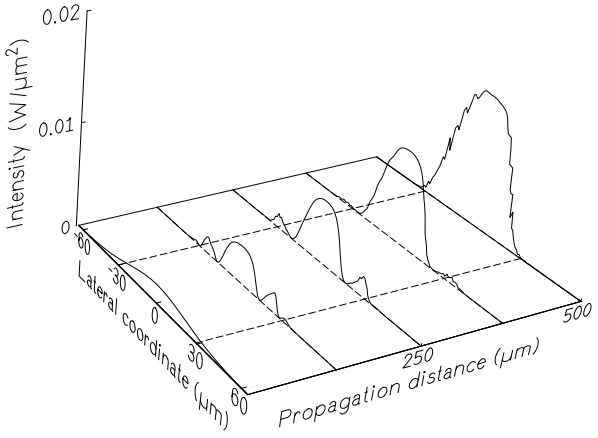

Fig. 4: Thermal lens compensated by built-in index variation.

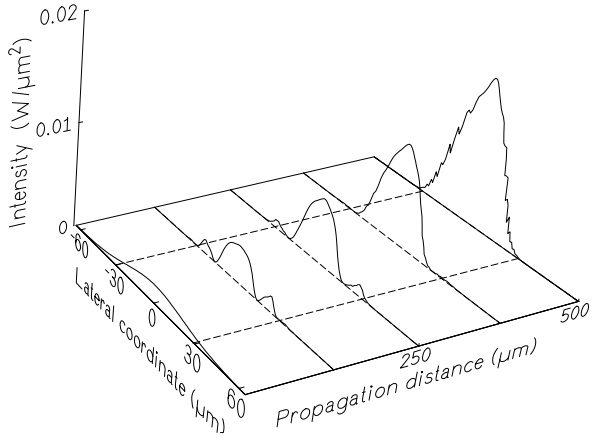

Fig. 5: Thermal lens compensated by antiguiding factor using non uniform pumping.

4. Antiguiding Factor

The antiguiding-factor is also called linewidth enhancement factor, Henry factor or *alpha*-factor. This word is not exact, since the antiguiding factor could cause either guiding effect or self focusing effect depending on the lateral profile of the gain coefficient. Without lateral hole burning, the antiguiding effect builds up a distributed negative lens, while with lateral hole burning its index variation forms a distributed positive lens and the antiguiding factor becomes a "self focus factor". This induced index variation adds to the distributed thermal lens makes compensation more difficult and determines the limitation of the high-power amplification. Exact control of the lateral gain profile under saturation is a challenging task. It needs not only a properly designed electrode geometry, but also a perfect active layer, which allows to generate the desired carrier concentration profile above the value of tansparency. With properly controlled non-uniform pumping we simulated the compensation to the thermal lens produced by antiguiding factor. The output beam profile in Fig. 5 has a satisfactory quality.

5. Unstable Cavity and MOPA

Unstable cavities and master oscillator power amplifiers (MOPAs) are conventional ways to prevent filamentation. For semiconductor devices, the unstable cavity can be constructed easily by well-designed built-in index compensation and non-uniform pumping. The distributed negative lens is equivalent to the convex mirrors of conventional unstable cavity. Built-in index compensation determines the approximate operating point, controlled non-uniform injection provides a fine adjustment of antiguiding factor or compensation. Fig. 6 shows the configurations of non-uniform pumping. The electric isolations between electrodes are provided by proton injection. The distance between electrodes are less than electric and thermal diffusion distances. Driving each electrode separately can avoid lateral hole burning and can adjust the antiguiding factor compensation.

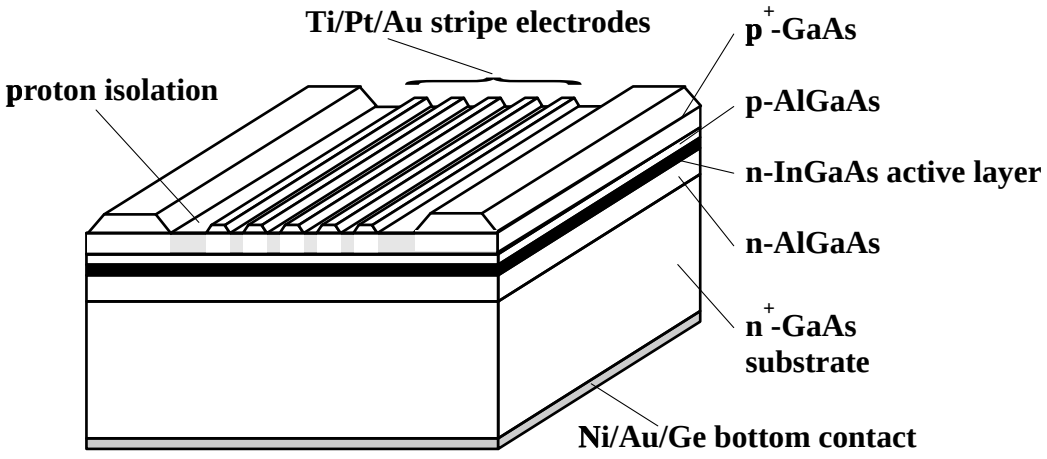

Fig. 6: Semiconductor unstable cavity laser with separate drived electrodes for antiguiding factor compensation.

Controlled non-uniform pumping can also be used in a MOPA device for beam-profile shaping. The optical intensity distributes in longitudinal and lateral direction non-uniformly in MOPA devices, the inhomogeneous saturation requires a separate pumping in both longitudinal and lateral direction. Since the integrated MOPAs have no noise due to mechanical instability, they are suitable for self-adaptive controlled driving. Fig. 7 shows a schematic structure of such a MOPA for multilevel amplifications. The wave fronts of the output beam are monitored by a computer, its distortions can be corrected self-adaptively by adjusting the electrodes in the two shaping sections. The last shaping section produces a negative lens of short focus to diverse the backscattered beam into absorptive layers. Electrodes above the absorptive layers are controlled to decrease the lateral carrier diffusion and form two strong absorption sides, which are favorable for eliminating spatial high frequency signals and for preventing filamentation.

6. Conclusions

Numerical simulation shows that the thermal lensing effect is mainly responsible for filamentation. Strong lateral optical confinement should be avoided used because of the waveguide edge diffraction. The antiguiding factor can be manipulated to compensate the thermal lens effect. Unstable cavity lasers and MOPAs with distributed index compensation structures are proposed. MOPAs with multilevel amplifications and beam profile shaping are expected to improve the high power amplification limitation.

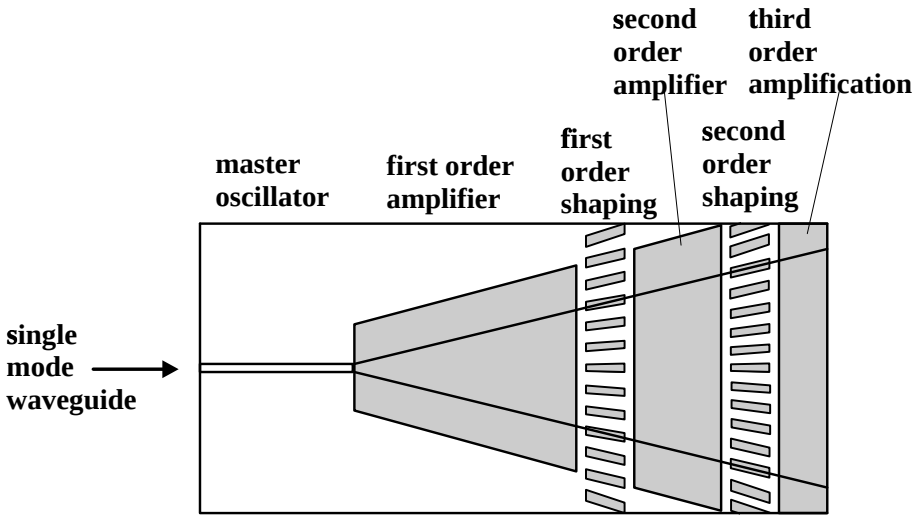

Fig. 7: MOPA device with separated electrodes for beam-profile shaping and multilevel amplification.

References

[1] L. Goldberg, D. Mehuys, M.R. Surette, D.C. Hall, "High-power, near-diffraction-limited large-are travelling wave semiconductor amplifiers", *IEEE J. Quantum Electron.*, vol. 29, pp. 2028-2043, 1993.

[2] Z. Dai, "Modelling of broad are travelling wave amplifiers," *Annual Report*, Department of Optoelectronics, University of Ulm, Germany, 1994.

[3] Z. Dai, R. Michalzik, P. Unger, "Operating characteristics simulation of high-power broad-stripe quantum-well semiconductor travelling wave amplifiers", *1995 OSA Technical Digest Series*, vol. 20, pp. 95-97.

[4] R.J. Long, A. Hardy, R. Park, D. Mehuys, S. O'Brien. J. Major, D. Welch, "Numerical analysis of flared semiconductor laser amplifiers", *IEEE J. Quantum Electron.*, vol. 29, pp. 2044-2051, 1993.

Vertical-Cavity Semiconductor Laser Amplifiers

Dieter Wiedenmann

The steady state amplification and the amplification bandwidth of vertical-cavity semiconductor laser amplifiers (VCSLA) have been investigated. We measured a small signal amplification of more than 20 dB with a bandwidth of 30 GHz. The response to sub-ps optical input pulses gives information on the dynamic behaviour of the device. The measured pulsewidth was below 60 ps. Operation in reflection and in transmission mode showed promising results.

1. Introduction

Recent progress in vertical-microcavity structures such as vertical-cavity surface-emitting lasers (VCSELs) and their potential application in parallel data processing has focused much interest in these devices. Up to now only a few investigations on amplification of an external beam have been reported [1,2]. Conventional semiconductor laser amplifiers which are based on edge emitting laser diodes usually show polarisation sensitivity of amplification and high coupling losses to optical fibres. Vertical-cavity semiconductor laser amplifiers (VCSLAs) easily overcome these problems due to their circular cavity geometry. Previous theoretical investigations have predicted the operating characteristics of VCSLAs to lie between those of standard-edge emitting travelling-wave and Fabry-Perot devices [3]. Applications can be foreseen as tunable wavelength-selective elements for optical preamplification and all-optical signal regeneration.

2. Device Structure

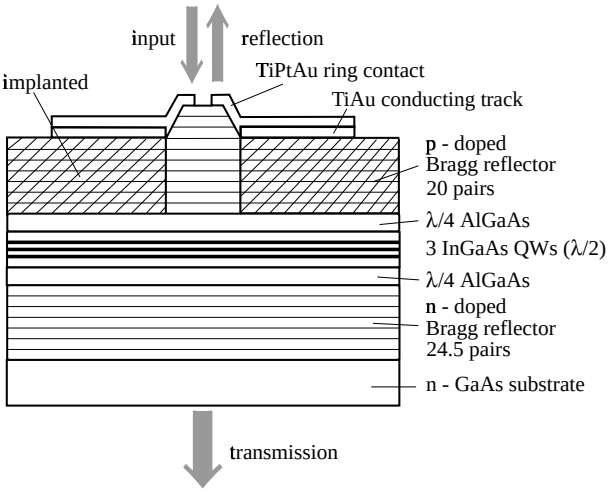

Fig. 1: Cross-sectional view of the vertical-cavity semiconductor laser amplifier under investigation.

A cross-sectional view of the VCSLA structure is shown in Fig. 1. The device is grown by molecular beam epitaxy on n-GaAs substrate [4]. The one-wavelength-thick central region contains three 8-nm thick strained $In_{0.2}Ga_{0.8}As$ quantum wells embedded between GaAs barriers and $Al_{0.4}Ga_{0.6}As$ cladding layers. The resonator region is surrounded by AlAs/GaAs Bragg

reflectors with 20 top and 24.5 bottom mirror pairs. The lateral current confinement is achieved by multi-step proton implantation into the top mirror.

3. Static Operation Characteristics

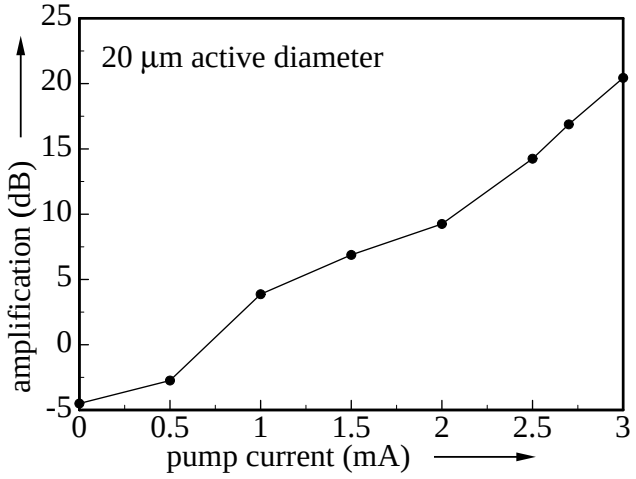

Fig. 2: Signal gain versus pump current for cw operation of the VCSLA.

The output power versus current characteristic of the VCSLA with 20 mm active diameter shows cw lasing for pump levels above 4 mA due to the high mirror reflectivities of the resonator. Light is emitted through both the top ring contact and the substrate at a wavelength of approximately 970 nm. To be sure that there is no self-oscillation of the amplifier, the highest pump level in our experiments has been 75 % of the threshold current. The static small-signal amplification characteristics, depicted in Fig. 2, has been measured using the emission of a Ti:sapphire cw-laser as input signal incidenting on the epitaxial side of the device. Input power is about 100 nW. A reflection mode amplification exceeding 20 dB is reached for a pump current of 3 mA. Amplification in transmission is much weaker due to the high reflectivity of the bottom mirror and additional absorption in the substrate. The resonance wavelength of the amplifier cavity can be tuned by slightly variing the driving current, and thus device temperature. Therefore, it is possible to match exactly the wavelength of the input light in order to reach the maximum amplification. With a detuning of the wavelength of the input light from the resonance of the amplifier cavity, a strong decay in amplification is observed, as shown in Fig. 3.

For comparison to the measured filter function of the cavity, we have also included a calculated function for the reflection signal gain of a Fabry-Perot amplifier with a single pass gain of 1.0086 [3]. The top and bottom reflectivities are 98.8 % and 99.3 %, respectively. The 3 dB bandwidth of the amplifier is about 0.1 nm, well suited for narrow-band active filters. Thermal tuning of the device is easily achieved, for instance in an extremely low power three-terminal configuration as in [5].

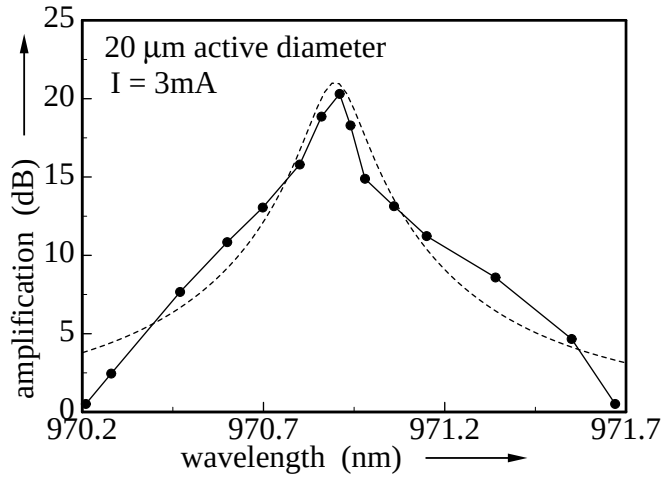

Fig. 3: Wavelength dependence of the static amplification at a pump current of 3 mA. The dashed curve is theoretical.

4. Dynamic Operation Characteristics

To investigate the dynamic behaviour of the device, being of great interest for high speed data processing,we have also studied the pulse response. For this purpose pulses of 200 fs length from a modelocked Ti:sapphire laser are used as the input, and a streak camera is employed for detection. Fig. 4 shows the FWHM of amplified transmitted pulses as function of driving current. For low pumping levels the pulse width of about 35 ps is close to the resolution limit of the measurement setup.

For pump levels above 1.7 mA there is a slight increase in pulse width. If we estimate a filter bandwidth of 0.1 nm for high pump levels and assume a gaussian shape for the input pulses, the minimum transmission pulse width is calculated to be about 60 ps, in fairly good agreement with the measured data. The increase in pulse width for increasing pump levels might thus be explained by the narrowing of the filter function of the amplifier cavity. Nevertheless the bandwidth is still large enough to handle 10 Gbit/s data rates.

5. Summary

In summary, we have experimentally demonstrated a vertical-cavity semiconductor laser amplifier with very good performance characteristics. The high static gain of up to 20 dB and the good dynamic behaviour together with other advantages of vertical-cavity structures such as polarisation insensitivity and low operating power make these devices very interesting for optical preamplification and all-optical signal regeneration in parallel optical data processing and lightwave communications.

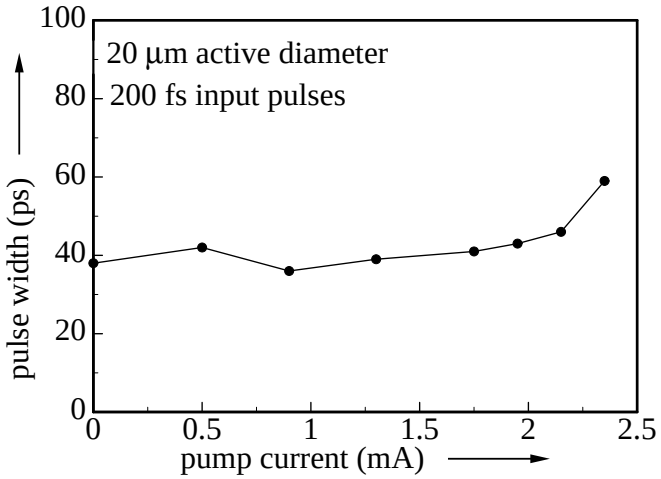

Fig. 4: Pulse width of the transmitted signal as a function of driving current for sub-ps pulse excitation of the VCSLA. Resolution of the detecting streak camera is about 35 ps.

References

[1] R. Raj, J.A. Levenson, J.L. Oudar, M. Bensoussan, "Vertical microcavity optical amplifying switch," *Electron. Lett.*, vol. 29, no. 2, pp. 167-169, 1993.

[2] F. Koyama, S. Kubota, K. Iga, "GaAlAs/GaAs active filter based on vertical cavity surface emitting laser," *Electron. Lett.*, vol. 27, no. 12, pp. 1093-1095, 1991.

[3] C. Tombling, T. Saitoh, T. Mukai, "Performance predictions for vertical-cavity semiconductor laser amplifiers," *IEEE J. Quantum Electron.*, vol. 30, no. 11, pp. 2491-2499, 1994.

[4] G. Reiner, E. Zeeb, B. Möller, M. Ries, K.J. Ebeling, "Optimization of planar Be-doped InGaAs VCSEL's with two-sided output," *IEEE Photon. Technol. Lett.*, vol. 7, no. 7, pp. 730-732, 1995.

[5] T. Wipiejewski, K. Panzlaff, E. Zeeb, K.J. Ebeling, "Tunable extremely low threshold vertical cavity laser diodes," *IEEE Photon. Technol. Lett.*, vol. 5, no. 8, pp. 889-892, 1993.

Epitaxy of High-Quality Nitrides: A Challenge for MBE

Markus Mayer, Markus Kamp

Ammonia (NH_3) has been investigated as nitrogen precursor for the MBE growth of Group-III Nitrides. We report on decomposition experiments of NH_3 using a high-temperature gas injector. The decomposition mechanism of the NH_3 is studied in detail. Theoretical calculations assuming thermal equilibrium for the NH_3 decomposition are presented and compared to experimental results. Applying this growth method, which we call On Surface Cracking (OSC), we have achieved low temperature (5 K) photoluminescence linewidths for GaN as narrow as 5.5 meV and electron mobilities of 220 cm^2/Vs at background carrier concentrations of $n \approx 2\times10^{17}$ cm^{-3} at room temperature. Furthermore ternary AlGaN, GaN/AlGaN SQW structures and n-doped (GaN:Si) have been successfully grown and characterized.

1. Introduction

The commercial success of high brightness blue and green light-emitting diodes (LEDs) [1] based on group-III nitrides and the recent announcement of first laser diodes [2] indicate the advantages of AlInGaN semiconductors compared to SiC or ZnMgSSe (II-VI). A few years ago commercially available blue and green LEDs were based on indirect semiconductors with low luminescence. Due to the direct wide bandgap of AlInGaN, high brightness LEDs are now available. In the chain for full color displays, GaN based LEDs have been the missing component to cover almost the whole visible light spectrum and led to a break through in this field of optoelectronics. The recent announcement of first blue nitride lasers [2] might further improve optical data storage due to an increase of data density by a factor of four compared to the current industry standard that is based on laser diodes emitting at a wavelength of $\lambda = 780$ nm.

High-quality nitrides and commercially available LEDs are usually produced using MOVPE [3] growth technique. However, MBE growth of AlInGaN offers potential advantages, compared to MOVPE. Benefits of MBE include the excellent controllability of thickness and composition. Compared to MOVPE the reduced deposition temperature enhances the incorporation of high vapor pressure elements such as In and Mg and leads to a general reduction of diffusion in the crystal. This improves interfaces and doping profiles. The general ability of MBE for growth of high quality devices has been proven in various semiconductor systems (e.g. AlGaAs/GaAs, etc.), but there are still various challenges in MBE growth of InAlGaN.

The problems encountered in MBE growth of nitrides are mainly due to the nitrogen source. Commonly, N_2 is employed as nitrogen source in MBE. The strong N-N binding energy (9.5 eV) is difficult to break and makes the application of plasma cracking sources (DC, RF, ECR plasmas) mandatory. Using plasma sources, ion damage is hardly to avoid [4]. Additionally, sputtering effects due to the self-bias voltages often result in contamination of the epitaxial structures. Other serious uncertainties with complex and sophisticated plasma sources include reproducibility and homogeneity.

In comparison the average binding energy of the N-H bonding of NH_3 (3.85 eV) [5] is significantly lower than the energy of the threefold N-N bonding. The dissociation of NH_3 can further be enhanced by catalytic effects.

We report on the use of NH_3 as an efficient N source in MBE. The thermal cracking of ammonia in a high temperature gas injector is investigated [6]. Furthermore we employed an On Surface Cracking (OSC) technique where NH_3 is cracked directly on the growing surface. Both techniques are compared and the influence of catalytic and/or chemical reactions will be discussed. Theoretical calculations assuming thermal equilibrium for the NH_3 decomposition are presented and compared to the experimental results.

2. Experimental

For our investigations we use an almost standard MBE system (Riber 32) which is adapted to group-V gas sources. The system is turbo pumped, the attached gas control system is home made. NH_3 is introduced into the growth chamber through a standard high temperature gas injector (Riber HTI 432). Group-III elements (Ga, Al) are supplied by effusion cells. For detection of background gas species and for the NH_3 cracking studies a quadrupole mass analyzer (QMA, Fisions SXP Elite) is used. Note that the QMA is mounted on the side wall and is therefore not hit by the direct molecular beam. For the cracking experiments the substrate temperature is set at 100°C. Unless otherwise mentioned, GaN layers are grown at growth rates of 700 nm/h to a thickness of approximately 2 μm. With an increased growth rate of 1.2 μm/h, comparable crystal and optical properties are achieved. Characterization of the grown structures is carried out with optical and scanning electron microscopy (SEM), x-ray diffraction (XRD) and photoluminescence (PL). Electrical quality is determined from Hall and CV measurements.

3. Cracking of NH_3 in the High-Temperature Gas Injector

The injector consists of a heated cracking zone (0-1200) °C with a molybdenum baffle. NH_3 is injected at a flow rate of approximately 10 sccm. The thermal cracking of NH_3 in the high temperature gas injector is investigated by the QMA. The cracking results, shown in Fig. 1 are corrected by the cracking pattern of the QMA.

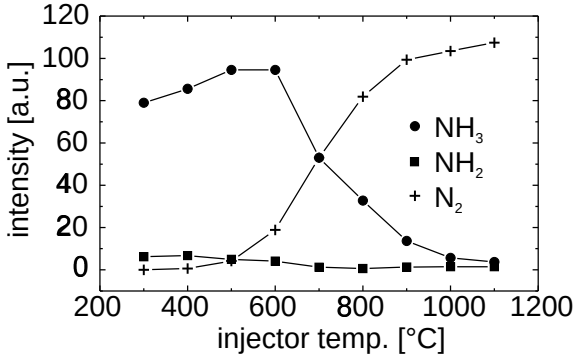

Fig. 1: Decomposition of NH_3 as verified with the quadrupole mass analyzer

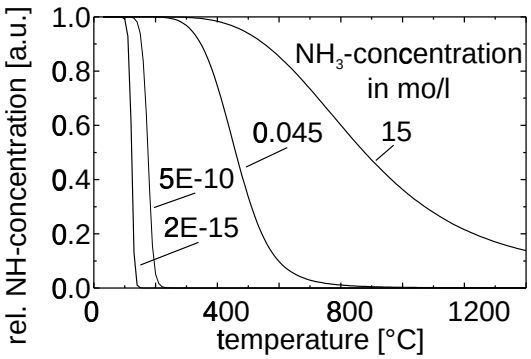

Fig. 2: Calculated NH_3 equilibrium concentration as a function of temperature and NH_3 concentration

The decomposition of NH_3, according to the experimental results of fig. 1, starts at temperatures of approximately 600 °C. Using the cracking of NH_3 in a high-temperature gas injector, the NH_3 should decompose into reactive N species (e.g. N, NH_1, NH_2). According to our results neither

atomic nitrogen nor other reactive N species are detectable in significant amounts. It cannot be excluded that the small quantities at measured atomar mass unit 16 are just an artifact, resulting from the determination of cracking pattern. The experimental results suggest the following overall reaction taking place inside the injector.

$$NH_3 \rightleftharpoons \frac{1}{2}N_2 + \frac{3}{2}H_2 \tag{1}$$

Under the assumption of thermal equilibrium the processes in the injector can be described by a thermal equilibrium constant K. Since the dissociation of NH_3 is endotherm and the total number of molecules changes with the position of the equilibrium, the equilibrium constant K depends on temperature as well as pressure. To investigate the thermic behaviour of the NH_3 dissociation, we are looking at a closed system with a NH_3 concentration of $[NH_3]_0$ at $T = 0\,K$. To calculate the relative $[NH_3]$ concentration with increasing temperature, following equations must be considered:

$$2[N_2] + [NH_3] = [NH_3]_0 \tag{2}$$

$$[H_2] = 3[N_2] \tag{3}$$

$$K_c = \frac{[NH_3]^2}{[N_2][H_2]^3} \tag{4}$$

The total amount of $[N_2]$ and $[NH_3]$ is given by equation (2), equation (3) considers the ratio of H_2 and N_2 (3:1) and equation (4) is the mass action equation for the dissociation of NH_3. The mass action equation has to be formulated in concentrations and not as usually in partial pressures, since equation (2) has to be formulated in concentrations. The temperature dependence of the equilibrium constant K, verified for the dissociation of NH_3 is given in the litterature [7]. Note that the pressure dependence of K can be eliminated with the ideal gas equation, assuming that NH_3 behaves like an ideal gas.

$$\begin{aligned} \lg K_c = {} & 2078/T - 2.498 \times \lg T - \\ & 1.258 \times 10^{-4} T + 1.859 \times 10^{-7} T^2 + 2.10 \end{aligned} \tag{5}$$

From the equilibrium constant K_c the temperature dependence of the ammonia dissociation can be calculated:

$$\frac{[NH_3]}{[NH_3]_0} = \frac{\frac{\sqrt{27}}{2} K_c [NH_3]_0 + 1 - \sqrt{\sqrt{27} K_c [NH_3]_0 + 1}}{\frac{\sqrt{27}}{2} K_c [NH_3]_0} \tag{6}$$

Fig. 2 shows the calculated NH_3 fraction versus temperature, assuming thermal equilibrium. Thermodynamic considerations reveal a dissociation of approximately 98 % of the NH_3 (concentration: 0.045 mol/l) under standard conditions (temperature: 273 K, pressure: 1013 mbar). For the conditions in our gasinjector, we assume a volume of 20 cm^3 and a pressure of (10 - 4) mbar. According to fig. 2 the NH_3 should completely dissociate under MBE conditions.

The difference between thermodynamic equilibrium and experimental results discloses that experimental conditions differ from perfect steady state conditions. We propose that the total

number of collisions between molecules and injector walls are insufficient to establish equilibrium conditions. Therefore, a certain quantity of NH_3 can pass the injector without being cracked.

To understand the dissociation on a microscopic scale one can consider the NH_3 dissociation on steel, which has been investigated in detail as a comparable mechanism. Here, the dissociation mechanism is the following [10]:

$$NH_{3g} \rightleftharpoons NH_{3ad} \tag{7}$$
$$NH_{3ad} \rightleftharpoons NH_{2ad} + H_{ad} \tag{8}$$
$$NH_{2ad} + H_{ad} \rightleftharpoons NH_{ad} + 2H_{ad} \tag{9}$$
$$NH_{ad} + 2H_{ad} \rightleftharpoons N_{ad} + 3H_{ad} \tag{10}$$
$$2H_{ad} \rightleftharpoons H_{2g} \tag{11}$$
$$2N_{ad} \rightleftharpoons N_{2g} \tag{12}$$

($g \mathrel{\hat{=}}$ gaseous , $ad \mathrel{\hat{=}}$ adsorpt)

with a decompositon rate ν (for $T \geq 550$ °C) given by

$$\nu = \frac{K_1 K_2 [NH_3]}{K_{-1} + K_2} \tag{13}$$

Where the NH_3 supply is regarded as the rate limiting step. The catalytic activity of molybdenum (which is the baffle material of our injector) is reported to be about 60 % of the catalytic activity of steel [8]. As mentioned above, thermal cracking of NH_3 involves steps where adsorpt N, NH, NH_2 are formed on the surface. Since the binding energies of these species to the surface are high, they do not desorb but react on surface to N_2 (and H_2). Due to the already mentioned strong binding energy of N_2, growth of GaN can not be obtained from N_2 without plasma sources. Instead of NH_3 injector cracking we propose an On Surface Cracking (OSC) technique. The NH_3 is dissociated directly on the growing surface. Assuming that the NH_3 dissociation includes the same surface states, the active nitrogen (N_{ad}) can chemically react with the elemental gallium on surface to form GaN. These considerations indicate that the cracking of NH_3 directly on surface is an excellent possibility for using NH_3 as a precursor for MBE-grown nitrides.

4. On Surface Cracking of NH_3

Applying OSC for GaN growth we find that growth can be performed at temperatures as low as 550 °C. Excellent GaN optical and crystalline properties are achieved at substrate temperatures around 800 °C using a beam equivalent pressure of 1.5×10^{-5} mbar and 5×10^{-7} mbar for NH_3 and Ga, respectively. This corresponds to a V/III ratio of approx. 30. High-quality 2 μm thick bulk GaN films are obtained on (0001) α-Al_2O_3 (c-plane) substrates using a short nitridation step and a thin AlN nucleation layer. Fig. 3 shows characteristic atomic force micrographs (AFM) of the sapphire after nitridation, after following formation of the AlN nucleation layer and after subsequent growth of the 2 μm GaN layer. After nitridation the topography shows a roughness of less than 1.5 nm. Numerous tiny islands of about 50 nm width and 10 nm height appear after formation of the nominally 30 nm thick AlN nucleation layer, grown at 750 °C and annealed at 850 °C. Besides these islands, a grainy background with grain sizes of less than 10

nm is observed. The growth of this nucleation layer obviously has a three-dimensional nature. Despite this three-dimensional nature of the nucleation layer the surface of the resultant 2 μm thick GaN layer smoothens.

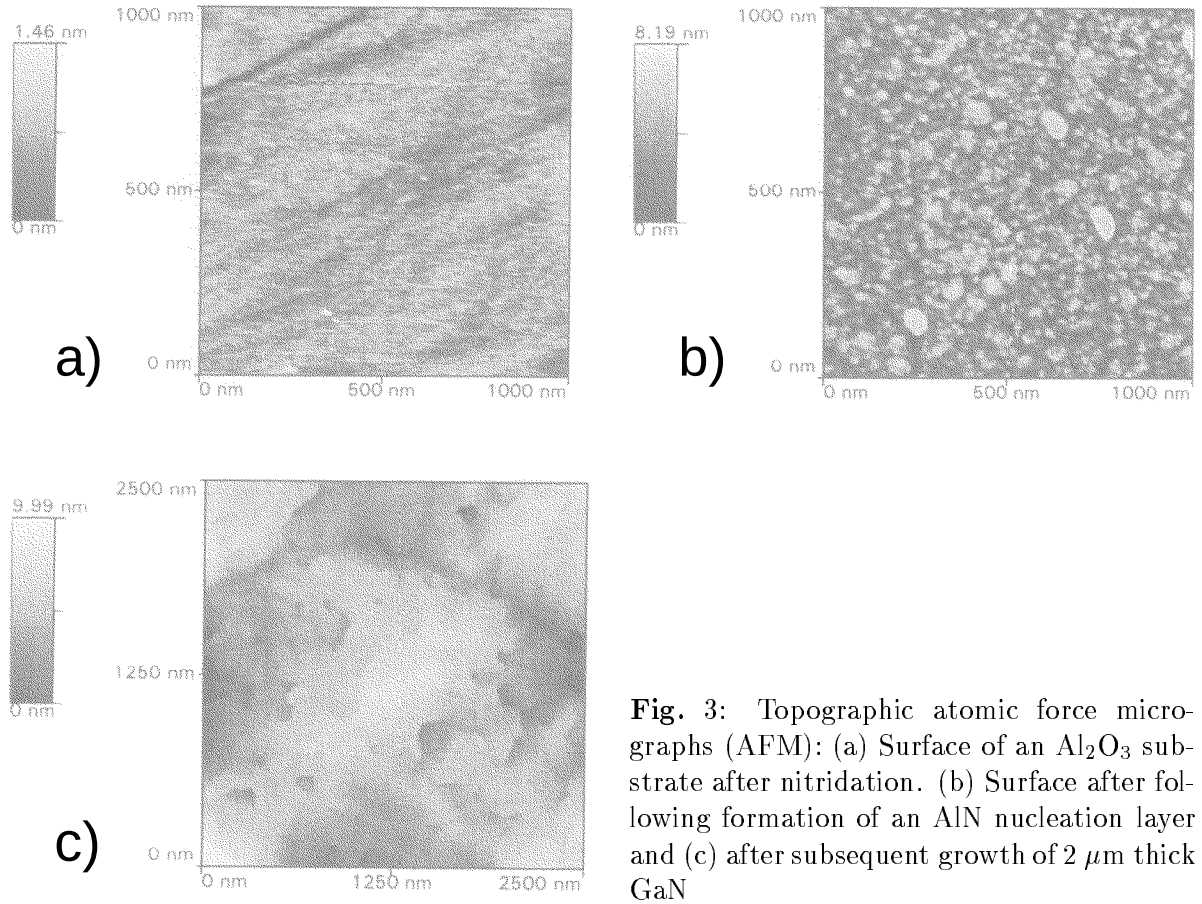

Fig. 3: Topographic atomic force micrographs (AFM): (a) Surface of an Al_2O_3 substrate after nitridation. (b) Surface after following formation of an AlN nucleation layer and (c) after subsequent growth of 2 μm thick GaN

The optical quality of GaN is investigated with PL as shown in Fig. 4. The low-temperature luminescence (5 K) is dominated by a transition at 3.480 eV, probably a D°X recombination. The small linewidth of 5.5 meV of this recombination indicates the high optical quality. Yellow emission, often present between 2 eV and 2.75 eV, is so much suppressed that it could not be detected, even at 300 K.

Electrical properties are obtained from Hall and CV measurements. With optimized growth conditions free carrier concentrations are 1×10^{17}cm^{-3} with mobilities of 220 cm^2/Vs at 300 K. The x-ray diffraction linewidth of 2 μm thick GaN layers is typically 450 arcsec ((0002) reflex, Cu $K_{\alpha1}$, omega scan).

A significant improvement in crystal quality is observed, when growth of GaN is performed on a GaN layer grown with our MOVPE system. This layer consists of a 0.5μm thick GaN grown on sapphire. The original x-ray linewidth of 100 arcsec (GaN) is reduced to 70 arcsec after MBE-overgrowth with 2 μm GaN. We conclude that the crystal quality of GaN films is essentially affected by the MBE nitridation and nucleation process. These experiments reveal also that there is still room for further optimization of nitridation and MBE growth of nucleation layer.

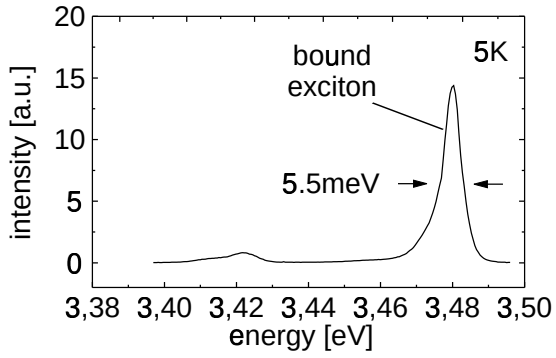

Fig. 4: Photoluminescence of 2-μm-thick GaN at 5 K

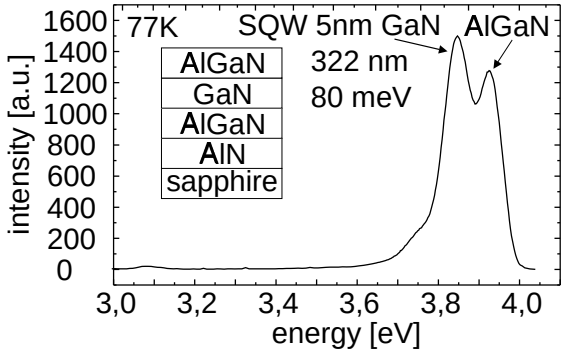

Fig. 5: Photoluminescence of nominally 5 nm GaN-SQW, embedded in AlGaN

Doping of binary GaN is further investigated, using Si for n-doping. We obtain free carrier concentrations of GaN:Si layers in the range of $n = 1\times10^{19}$ cm^{-3} with mobilities of $\mu = 160$ cm^2/Vs. Ternary $Al_yGa_{1-y}N$ up to 32 % Al is grown. The optical quality of $Al_{0.32}Ga_{0.68}N$ is reasonable with a PL linewidth of 160 meV at 77 K.

First GaN SQW structures with nominally 5 nm thick GaN QWs show also promising optical and crystalline quality. Characteristic photoluminescence of these GaN/AlGaN heterostructure, taken at 77 K is shown in Fig. 5. The PL linewidth of the GaN SQW is 80 meV at an energy of 3.846 eV. The higher intensity, compared to the AlGaN barriers originates in carrier confinement in the QW. The higher energy, compared to bulk GaN indicates the effect of energy quantization.

We believe that a decrease in linewidth and an increase in intensity is obtainable by optimizing the GaN/AlGaN interfaces and also the properties of bulk material.

5. Summary

We report on cracking of NH_3 on the growing surface and in a high-temperature gas injector. Efficient cracking of NH_3 in the gas injector is verified at temperatures above 600 °C using a quadrupole mass analyzer. The dominant cracking product is N_2 which, due to its high binding energy, is not appropriate for growth of nitrides. However, On Surface Cracking (OSC) of NH_3 results in excellent GaN optical qualities. Photoluminescence at 5 K reveals a bound exciton transition (probably D°X) with a linewidth of 5.5 meV (FWHM) at 3.480 eV. Yellow emission at 300 K is not detected. Electrical transport measurements show electron mobilities of 220 cm^2/Vs for free electron concentrations as low as 1×10^{17} cm^{-3}. X-ray rocking curves of this layers prove a linewidth of 450 arcsec, that indicates room for further optimizations of sapphire nitridation and growth of the nucleation layer. We conclude that OSC of NH_3 offers an excellent N source for MBE growth of GaN. It is easy to maintain, highly reproducible, economical, unsophisticated and the requirements to the injector are very low compared to every plasma source. Ternary AlGaN has been successfully grown up to 32 % Al. The photoluminescence of bulk $Al_{0.32}Ga_{0.68}N$ shows a linewidth of 160 meV at 77 K. n-doping of binary GaN is obtained with Si, resulting in free carrier concentrations up to $n = 1\times10^{19}$ cm^{-3} and mobilities of $\mu = 160$ cm^2/Vs (300 K). First nominally 5 nm thick GaN SQWs, embedded in AlGaN barriers show PL linewidths

of 80 meV (77 K, E_{QW}=3.846 eV). The PL spetra indicates carrier confinement and energy quantization in the QW.

6. Conclusions

On the way to highly luminous devices we started to face challenges, as a suitable N precursor in MBE, optimization of sapphire nitridation, growth of AlN nucleation layer, *n*-doping etc. From our cracking investigations we conclude that OSC of NH_3 offers an excellent N source for MBE growth of GaN.

Essentially for blue/green LEDs are ternary InGaN and *p*-doping. According to the literature the *p*-doping in nitrides is successfully achieved using Mg. However, the formation of a Mg-H complex during growth is a often described uncertainty and makes an additional annealing step for activating the Mg neccessary.

Recently, we started growing Mg doped GaN layers in our new modified MBE system and it looks very promising to achieve *p*-doped GaN. The remaining task on the way to the MBE-grown blue/green LED is the optimization of optical and crystalline qualities of the ternary InGaN semiconductor. Due to the increasing indium desorption with higher growth temperatures it is difficult to achieve ternary $In_xGa_{1-x}N$ with high indium contents.

7. Acknowledgments

We like to acknowledge contributions from C. Kirchner, S. Menzel, A. Fricke, T. Albrecht, M. Mundbrod, H. Sternschulte and S. Hild as well as the financial support from the German Minister Education, Science, Research and Technology (BMBF).

References

[1] S. Nakamura, "A Bright Future for Blue/Green LEDs," *Circuit and Devices*, pp. 19-25, 1995.

[2] S. Nakamura, M. Senoh, S. Nagahama, N. Iwasa, T. Yamada, T. Matsushita, H. Kiyoku, Y. Sugimoto, "InGaN-Based Multi-Quantum-Well-Structure Laser Diodes," *Jpn. J. Appl. Phys. Lett.*, vol. 35, pp. 74-77, 1996.

[3] I. Akasaki, H. Amano, "Crystal Growth of Column III Nitrides and Their Applications to Short Wavelength Light Emitters", *J. Cryst. Growth*, vol. 146, pp. 455-461 , 1995.

[4] R.J. Molnar, R. Singh, T.D. Moustakas, "Operation of a Compact Electron Cyclotron Resonance Source for the Growth of Gallium Nitride by Molecular Beam Epitaxy (ECR-MBE)," *J. Elect. Mat.*, vol. 4, pp. 275-281, 1995.

[5] L. Pauling, *J. Am. Soc.*, vol. 54, p.3574, 1932.

[6] M. Kamp, M. Mayer, A. Pelzmann, A. Thies, H.Y. Chung, H. Sternschulte, O.Marti, K.J. Ebeling, "NH_3 as Nitrogen Source in MBE Growth of GaN," *Proceedings of Topical Workshop on III-V Nitrides*, Nagoya, Japan, 1995.

[7] G.N. Lewis, E.Q. Adams in "Gmelin: Handbuch der anorganischen Chemie," 1936.

[8] M. Grunze in "The Chemical Physics of Solid Surfaces and Heterogenous Catalysis," edited by D.A. King, D.P. Woodruff, Elsevier, Amsterdam, 1982.

[9] M. Kamp, M. Mayer, A. Pelzmann, S. Menzel, H.Y. Chung, H. Sternschulte, K. J. Ebeling, "Thermally cracked NH_3 for MBE Growth of GaN," accepted for publication, *Material Research Society (MRS), Fall Meeting 1995*, Boston, USA, 1995.

[10] G. Ertl, M. Huber, "Mechanism and Kinetics of Ammonia Decomposition on Iron," *J. Cat.*, vol. 61, pp. 537-539, 1980.

MOVPE Growth of Group III Nitrides

Christoph Kirchner

Group III Nitrides (GaN, InN, AlN and their alloys) offer a large potential for devices such as high- brightness blue and green LEDs, short-wavelength Lasers, UV photodetectors and high-temperature electronic devices. In this article, the process of epitaxial nitride growth is described.

1. Introduction

Conventional III–V semiconductors (e.g. group III arsenides and group III phosphides) are limited to bandgap energies between 0.4 eV (InAs) and 2.4 eV (AlP). The group III nitrides GaN, AlN, InN and their ternary alloys have direct bandgaps with bandgap energies between 1.9 eV (InN) and 6.2 eV (AlN). Compared to another group of high-bandgap materials, the II–VI semiconductors, group III nitrides offer a higher utilizable bandgap range, higher bonding strength, and better thermal conductivity.

For fabrication of devices, epitaxial growth of layers and heterostructures is required. Here, group III nitrides suffer from the lack of suitable lattice matched substrate materials. Nitrides are grown either on sapphire (Al_2O_3, a or c axis) or 6H SiC. SiC offers superior properties due to an almost matched lattice constant and appropriate thermal expansion coefficient. Additionally, SiC substrates are available as $p-$ and $n-$ conducting type, while sapphire is an insulator. But due to the high prices of SiC substrates, sapphire is usually preferred for the growth of nitrides. A well established technique for the growth of nitrides, suitable for the large scale production of devices, is the Metal-Organic Vapor Phase Epitaxy (MOVPE).

2. MOVPE System

The growth experiments are carried out with an AIXTRON AIX 200 RF MOVPE. The system is equipped with a water cooled quartz glass reactor. 2 inch substrates are loaded on a SiC–coated graphite susceptor with rotating disc. An RF heating allows process temperatures up to 1200 °C. The growth pressure can be adjusted between 20 and 900 mbar. Fig. 1 shows a simplified function scheme of the MOVPE system. The carrier gases are nitrogen or hydrogen. High purity of the carrier gases is mandatory to avoid contamination of the metalorganic (MO) precursors and impurities in the grown layers. Thus, the nitrogen is chemically purified, while the hydrogen is purified in a Pd diffusion cell. The carrier gas is led through the metalorganic sources. The group–III sources are metalorganic compounds filled in stainless steel bottles with dip tube and outlet tube. The carrier gas bubbles through the organometallic compound and thereby transports the source molecules into the reactor. To achieve a constant MO flow, the carrier gas inlet flow is stabilized by a mass flow controller (MFC).

The MO flow (Q_MO) can be calculated using the following equation:

$$Q_{MO} = Q_s \cdot \frac{p_{d,MO}(T)}{p_c - p_{d,MO}(T)} \tag{1}$$

with

Q_s :	carrier gas source flow
$p_{d,MO}(T)$:	vapor pressure of metalorganic compound
p_c :	total pressure in the bottle

For a constant vapor pressure of the organometallic compounds, the bottles are stored in temperature-controlled bathes. The pressure controller stabilizes the total pressure in the bottle. The pusher flow accelerates the MO flow. This is important for fast switching between different metalorganic sources.

Additionally, carrier gas continuously flows into the reactor for purging and for adjusting the flow speed through the reactor. The run–vent manifold switches the process gases between the reactor and the vent line, which leads to exhaust. Reactor and vent line have to be kept at the same pressure to avoid pressure bursts when switching which disturb the flow control of the MFCs. The exhaust gases are cleaned by dry-bed absorbers.

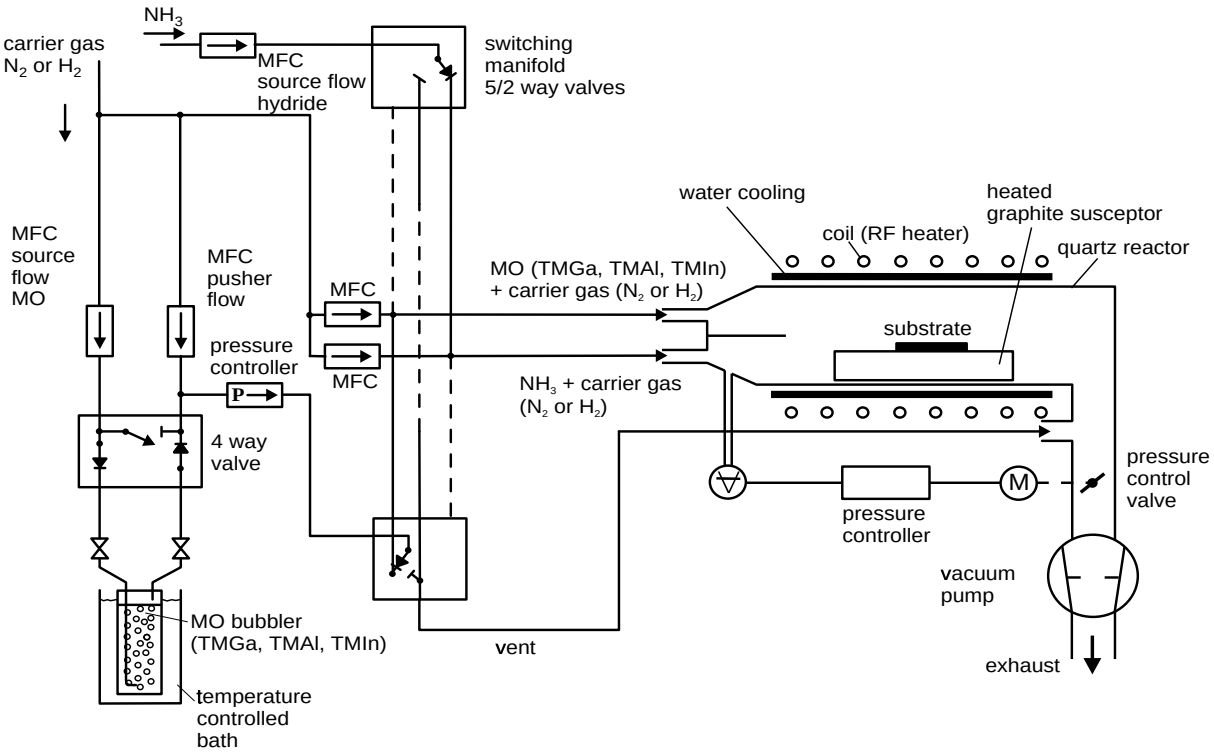

Fig. 1: Functional scheme of MOVPE system.

3. Growth Experiments

Group III nitrides are existing in two polytypes, the wurtzite and the zincblende modification. The wurtzite modification is the energetically preferred crystal structure. It is possible to grow zincblende GaN on GaAs substrates, while wurtzite GaN is grown on sapphire or SiC. All our nitride films are grown on c–plane oriented sapphire substrates. The substrates are cleaned in organic solvents and deionized water. The group–III organometallic precursors are trimethylgallium (TMGa, $(CH_3)_3Ga$), triethylgallium (TEGa, $(C_2H_5)_3Ga$), trimethylaluminium (TMAl, $(CH_3)_3Al$) and trimethylindium (TMIn, $(CH_3)_3In$). The group–V precursor is high purity ammonia (NH_3). For *p*-doping, the organometallic source biscyclopentadienylmagnesium (Cp_2Mg, $(C_5H_5)_2Mg$) is used, while *n*-doping is realized with silane (SiH_4).

A typical temperature profile for a MOVPE growth process is shown in Fig. 2. After loading the substrate into the growth chamber, the sample is heated up to 1000 °C under flow of ammonia to remove surface impurities and to nitridate the sapphire surface, i. e. replacement of some oxygen atoms desorbed from the surface by nitrogen atoms from dissociated ammonia. Then the process temperature is lowered to 800 °C for growth of the AlN nucleation layer. Because of the low temperature, the nucleation layer is highly polycristalline. The nucleation layer is extremely important for the quality of the grown epilayers, because the lattice mismatch between sapphire and GaN is very high. The nucleation layer forms a transition between the different lattice parameters. Besides the investigated AlN nucleation layers, GaN nucleation layers can be used too. These nucleation layers are grown at 600 °C. After growth of the nucleation layer, the reactor temperature is raised to 1060 °C. With this annealing step, the layer becomes partially monocrystalline on the surface. On this surface, epitaxial growth is performed.

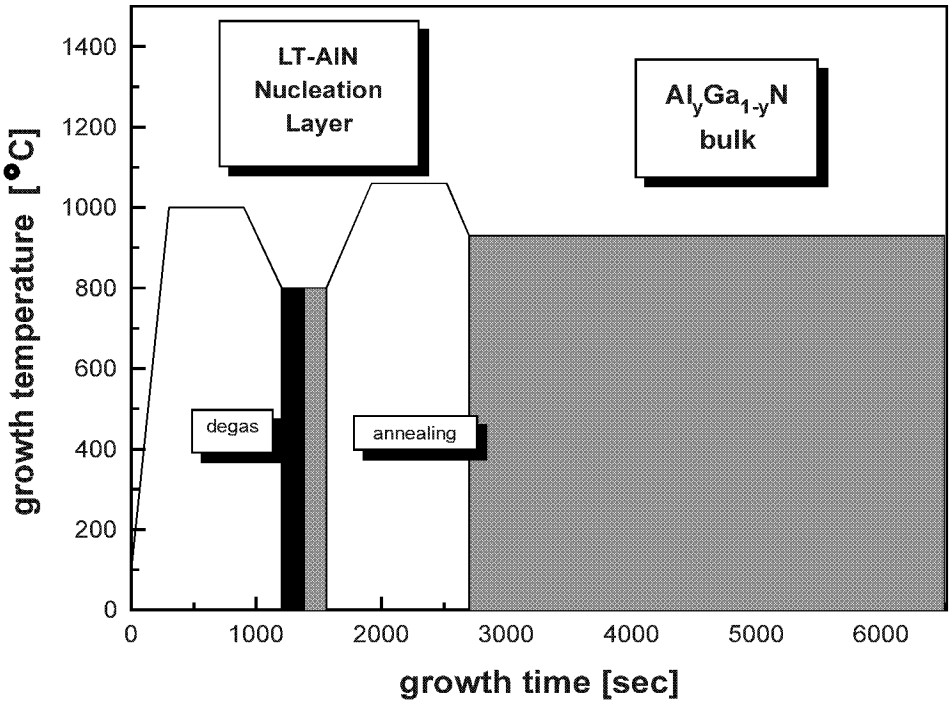

Fig. 2: Temperature profile of a MOVPE growth process.

Fig. 3 shows an atomic force micrograph (AFM) of an AlN nucleation layer with grainy surface morphology. Original size of the detail is 250×250 nm. Epitaxial GaN films, grown on this surface, have smooth surfaces, displayed in Fig. 4. The SEM micrograph shows the surface of a 400 nm thick GaN layer grown at 1000 °C with a magnification of 30000.

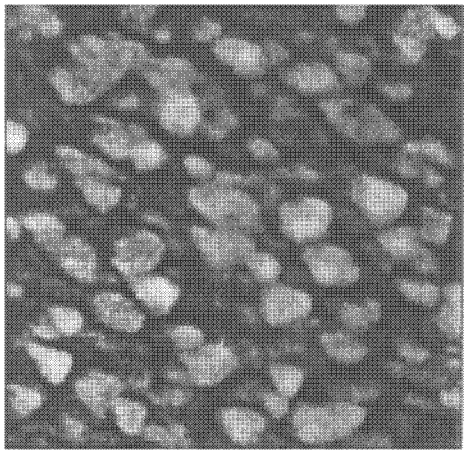

Fig. 3: AFM image of AlN nucleation layer

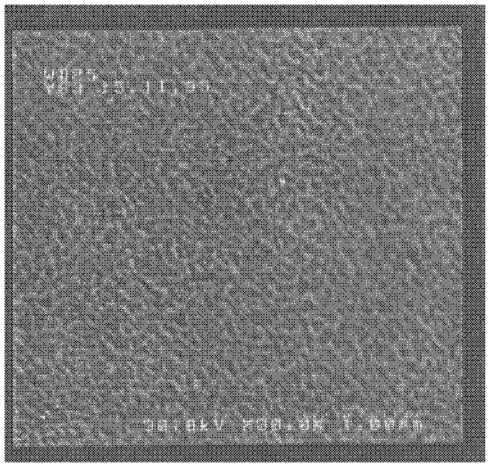

Fig. 4: SEM image of GaN layer

Typical temperatures for the growth of GaN and AlGaN are about 1000 °C and 750–850 °C for the growth of InGaN. The reactor pressure is varied from 25 to 150 mbar (*low pressure* MOVPE). V/III ratios are in the range from 3000 up to 7000 (GaN and AlGaN). Lower growth temperatures require higher V/III ratios, up to 20000 for growth of InGaN, due to the lower thermal decomposition of ammonia.

Characterization of the grown nitride layers is performed using x-ray diffraction (XRD), Photoluminescence, thickness, Hall and CV measurements. Fig. 5 shows a PL spectrum and a XRD curve of a 200 nm thick GaN layer, grown at 1000 °C and 25 mbar reactor pressure. PL measured at 300 K shows near–bandgap luminescence. The long wavelength emission in the yellow spectral region at around 2.2 eV is usually strongest at 300 K. The long wavelength emission is attributed to nitrogen vacancies. Due to improved process technology, the long wavelength emission of this sample is very low. The linewidth of 122 arcsec (full-width at half maximum, FWHM), measured with XRD, signifies excellent crystal quality. Our best MOVPE–grown GaN films have linewidths of 50 arcsec.

First doping experiments have been carried out, using Cp_2Mg for p–doping. P–type conduction in nitrides is not easy to achieve. For a p–type conduction in the range of $10^{18}\,cm^{-3}$ at room temperature, a Mg incorporation of around $10^{20}\,cm^{-3}$ in the nitride film is necessary. This is caused by the high activation energy of the Mg acceptors of 150–200 meV. At room temperature, only a few percent of the acceptors are ionized.

The high magnesium content of the nitride films decreases crystal quality. In MOVPE, Cp_2Mg doped nitride films require a post–growth annealing step in N_2 ambient to activate the acceptor. It's generally assumed that the annealing dissociates the incorporated Mg–H complexes and expels the hydrogen out of the layers. Without annealing, p–type conduction cannot be achieved due to passivation by hydrogen. The success of post–growth treatment for Mg activation was first shown by Akasaki et al. [1] using *Low–Energy Electron Beam Irradiation* (LEEBI) treatment of Mg doped GaN layers. Fig. 6 shows the p–conduction of a Mg doped GaN layer, annealed for 10 min at 700 °C in nitrogen ambient. The n–type background carrier concentration of the GaN films is in the range from $10^{17}\,\mathrm{cm}^{-3}$ to $10^{19}\,\mathrm{cm}^{-3}$.

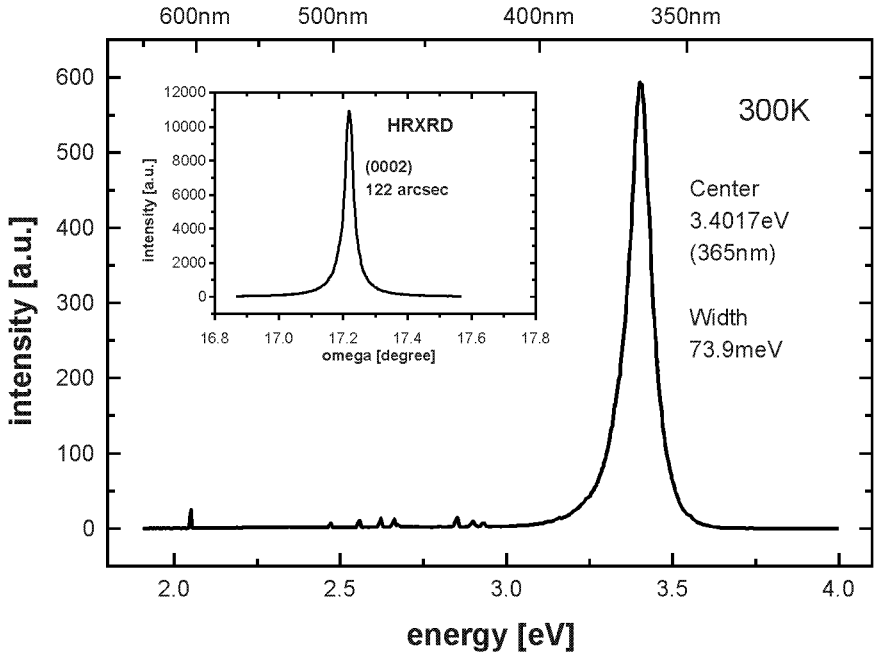

Fig. 5: PL spectrum and XRD curve of GaN

The ternary alloys $Al_xGa_{1-x}N$ and $In_xGa_{1-x}N$ are very important materials for fabrication of devices. Fig. 7 shows a PL spectrum and a XRD curve of AlGaN with an aluminium content of 10 %, grown at 930 °C. The PL peak shifts to shorter wavelenghts. The Al content can be calculated from the PL shift and the XRD peak shift. In Fig. 8, a PL spectrum and a XRD curve from InGaN with an In content of 5 % grown at 800 °C are displayed. The PL peak has shifted to longer wavelenghts. The XRD peak is quite broad, signifying poor crystal quality. This is caused by the low growth temperature, which is necessary due to the high vapor pressure of indium. High growth temperatures prevent In incorporation into the GaN layers.

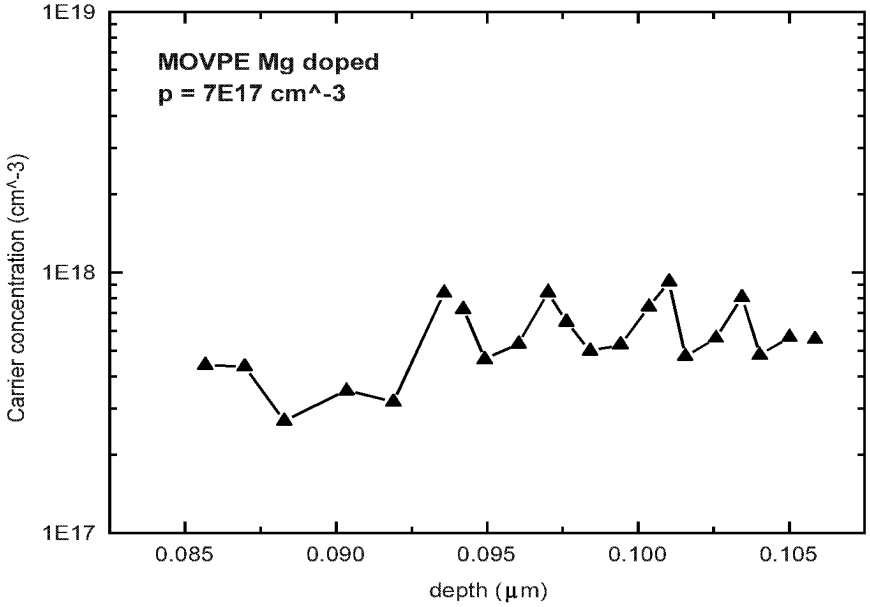

Fig.6: p–doping profile of Mg doped GaN layer

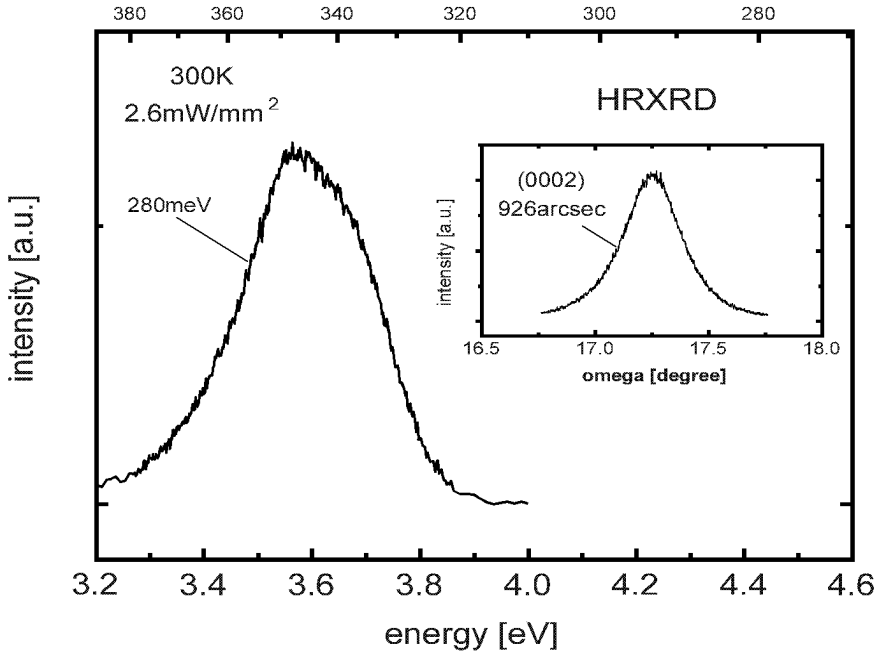

Fig. 7: PL spectrum and XRD curve of AlGaN

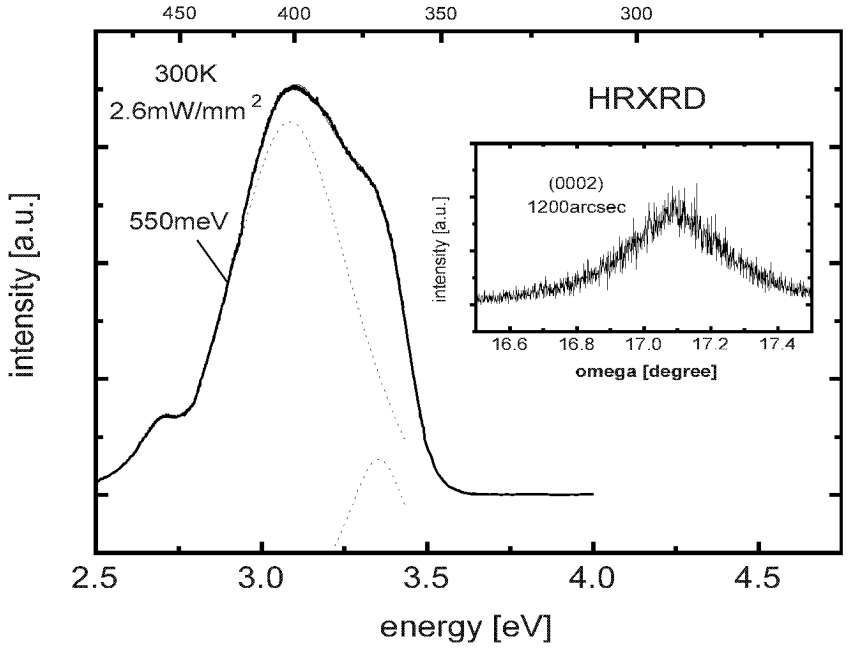

Fig. 8: PL spectrum and XRD curve of InGaN

4. Summary

Growth of group III nitrides in MOVPE has been performed. Epitaxial GaN films reveal excellent crystal quality up to 50 arcsec linewidth in XRD. Mg–doped GaN samples annealed under Nitrogen, show *p*–type conduction of $7{\cdot}10^{18}\,\mathrm{cm}^{-3}$. The MOVPE grown ternary alloys AlGaN and InGaN require further improvment of crystallinity and optical properties.

References

[1] H. Amano, M. Kito, K. Hiramatsu, I. Akasaki, "*p*–type conduction in Mg–doped GaN treated with low–energy electron beam irradiation (LEEBI)", *Jpn. J. Appl. Phys.*, vol. 28, no. 12, pp. L2112–L2114, December 1989.

Characterization of Group III Nitrides

Arthur Pelzmann, Markus Kamp

Group III nitrides grown with GSMBE and MOVPE on c-plane sapphire substrates are examined by temperature dependent photoluminescence measurements, x-ray diffraction and electrical characterization methods (Hall, CV).

1. Introduction

Group III nitrides (e.g. AlN, GaN, InN, and their alloys) are predestinated for optoelectronic applications from the long visible light range down to UV wavelengths since they cover a bandgap range from 1.6 to 6.2 eV. Nowadays, one of the most important optoelectronic applications of group III nitrides are GaN based blue and green LEDs. High-brightness GaN-based blue LEDs were first fabricated by S. Nakamura using α-Al_2O_3 as substrate material and two-flow metal-organic vapor phase epitaxy (MOVPE) for the epitaxial growth [1]. The lattice mismatch between sapphire and GaN is very high (GaN: $a = 3.189$ Å, α-Al_2O_3 : $a = 4.758$ Å). A more suitable substrate material for the epitaxial growth of GaN is 6H SiC. However, due to the high price and the low availability of suitable 6H SiC, most groups use the less expensive α-sapphire for the growth of wurtzite-type nitrides despite the above mentioned large lattice mismatch. Best results in growth of high quality group III nitrides are based on MOVPE techniques. However, the growth of group III nitrides by gas-source molecular beam epitaxy (GSMBE) appears also to be very promising. [3, 4]. Particularly in our department we have the opportunity to compare both growth techniques directly since we are equipped with a MOVPE and a GSMBE system.

The first step in the fabrication of optoelectronic semiconductor devices is the optimization of the grown material referring to optical, electrical and crystalline quality. In our investigations we use high resolution x-ray diffraction (XRD) to examine crystalline quality. Temperature dependent photoluminescence (PL) yields information about radiative transitions. Electrical properties such as doping profile, carrier concentration and mobility are measured with Hall and CV (capacity voltage) techniques.

2. Experimental Setup

Optical characterization

For photoluminescence measurements we use the setup depicted in Fig. 1. A HeCd laser with a maximum output power of 65 mW at 325 nm is used for optical excitation. The wavelength of 325 nm (3.815 eV) is sufficient for excitation of group III nitrides in the temperature range from 300 K down to 4.2 K except for $Al_xGa_{1-x}N$ with Al contents above approximately 17 %. This is due to the energy of the near bandgap I_2-line (exciton bound to neutral donor) which is given by

$$E_{peak_{I_2}} = 3.47 + 1.75x + 0.98x^2$$

at 4.2 K [5]. For the excitation of alloys with higher Al contents we use the 275 nm (4.51 eV) line of a Ar^+-ion laser. The excitation beam is chopped and focused onto the sample. The

luminescence signal is analysed in a monochromator and detected with a photomultiplier using lock-In amplification technique. For temperature dependent PL, the sample is located inside a cryostat which allows measurements from room temperature down to 10 K. Normally, PL spectra are taken in the range of 330 nm (280 nm for AlGaN) to 650 nm.

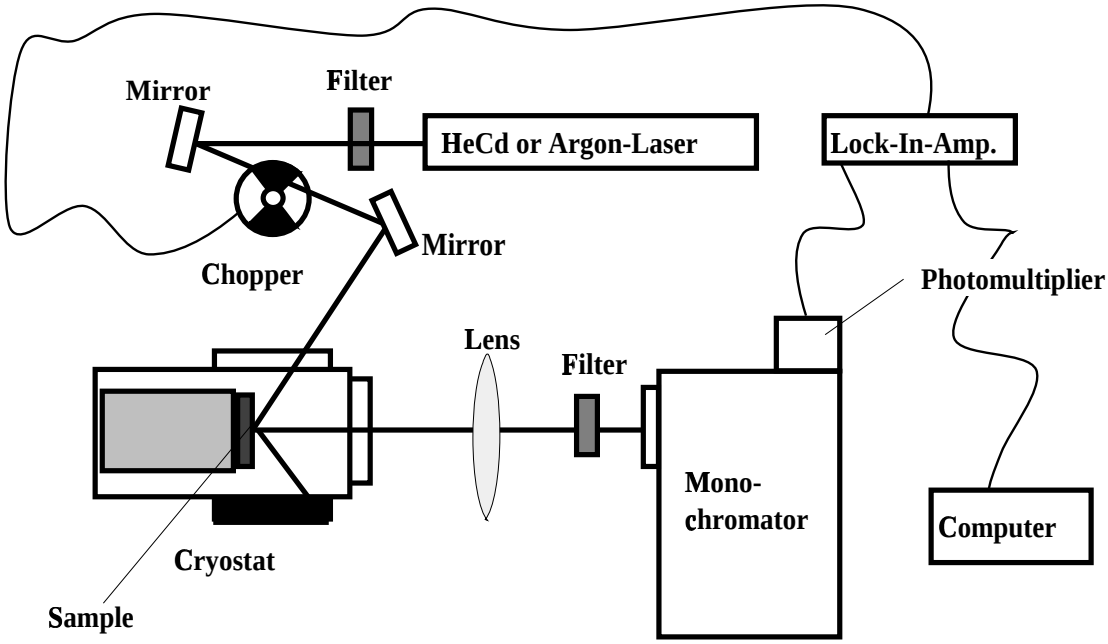

Fig. 1: Experimental setup for photoluminescence measurements on group III nitrides

Crystalline Characterization

For determination of the crystalline quality the (0002) reflexes of the nitride samples are measured using a Philips 5-crystal diffractometer ($Cu_{K_{\alpha 1}}$ line). A criterion for good crystalline quality is the linewidth of the measured reflex. The linewidth is determined by following contributions: the intrinsic rocking curve width of the investigated sample, the intrinsic rocking curve width of the monochromator, the rocking curve broadening by strain surrounding dislocations, the rocking curve broadening by angular rotation at dislocations and the rocking curve broadening due to crystal size, the rocking curve broadening due to curvature of the crystal [6]. Because the first two contributions will be constant for GaN, the rocking curve linewidth should be a measure for the density of dislocations in the layer.

X-ray diffraction is also used to calculate the Al and In content in the ternary alloys $Al_xGa_{1-x}N$ and $In_yGa_{1-y}N$.

Samples with high crystalline quality reveal thickness fringes in the XRD peaks which allow the calculation of the layer thicknesses. However, usually surface profiling and photoreflexion measurements are used to determine layer thicknesses.

Electrical Characterization

For determination of the free carrier concentrations and mobilities we use a standard Hall technique with a van der Pauw setup for conductivity measurements. Ohmic contacts for the Hall

measurements are formed on the layer surface by tempering In pellets under N_2 atmosphere for 10 s at 400 °C.

The depth profile of *p*-(Mg) and *n*-(Si) dopants are investigated with a mercury CV profiler.

3. Results and Discussion

The investigated samples are grown by MOVPE and GSMBE using c-oriented α sapphire as substrate material. The epitaxial growth of GaN on sapphire substrates leads to a wurtzite structure of the layers. Due to the high lattice mismatch, the layers are completely relaxed at growth temperatures. However, the post-growth cooling from approx. 1000 °C down to room temperature causes strain (which is obviously visible by the curvature of the wafer) due to the different thermal expansion coefficients ($\approx$ 27 % in a-direction). Large numbers of dislocations ($\approx 10^{10}\mathrm{cm}^{-2}$) are formed to reduce the resulting strain [7].

The dislocations are scattering centers for carriers. If they occur at high densities they can affect electron Hall mobilities which should decrease with increasing dislocation densities. Indeed, we found a correlation between the electron mobilities and the linewidth of the measured x-ray rocking curves as shown in Fig. 2 (free carrier concentration $n \approx 1 \times 10^{18}$ cm^{-3}). Therefore we assume that the rocking curve linewidths of our samples are principally broadened by dislocations and residual strain.

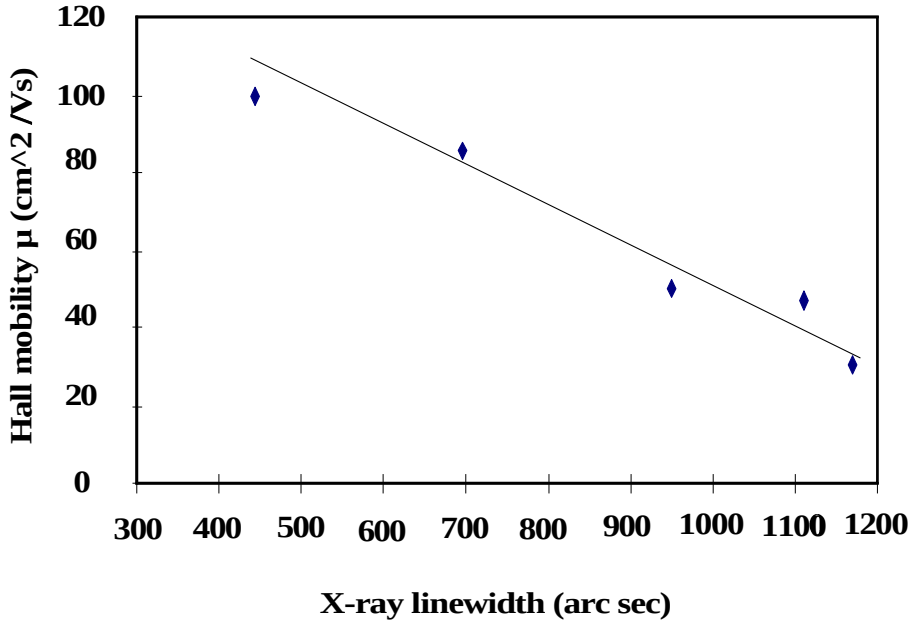

Fig. 2: Correlation between x-ray linewidths and hall mobilities for GSMBE-grown GaN

Due to the high concentration of native defects high unintentional background carrier concentrations in the range between $n = 10^{16}\mathrm{cm}^{-3}$ and $n = 10^{17}\mathrm{cm}^{-3}$ dependent on the growth technique are still common. As widely accepted, the background carrier concentration is attributed to nitrogen vacancies (V_N) [8].

This unintentionally "doping" is measured using a Hall-setup and the CV-profiler. The measured background carrier concentrations vary from 1×10^{15} cm^{-3} to 8×10^{18} cm^{-3} for GSMBE grown GaN samples and 1×10^{17}cm^{-3} to 1×10^{19} cm^{-3} for MOVPE grown GaN samples. Fig. 3 shows a viewgraph of theoretical Hall mobilities versus free electron concentration by Rode [2]. The curves are calculated by iteratively solving the Boltzmann equation with Fermi statistic. The topmost curve assumes a compensation ratio ($\frac{N_A}{N_D}$) of 0, the curves below correspond to 0.2, 0.4, 0.6, 0.8 downwards. Fig. 4 shows a comparison of our measured mobilities with the experimental data measured by many authors on intentionally and unintentionally doped MOVPE and GSMBE samples [2]. As one can see our data are in good agreement with that of other authors but measured mobility at $n = 10^{17}$cm^{-3} is about three to four times lower than the theoretical values for low compensation. This could be due to following reason.

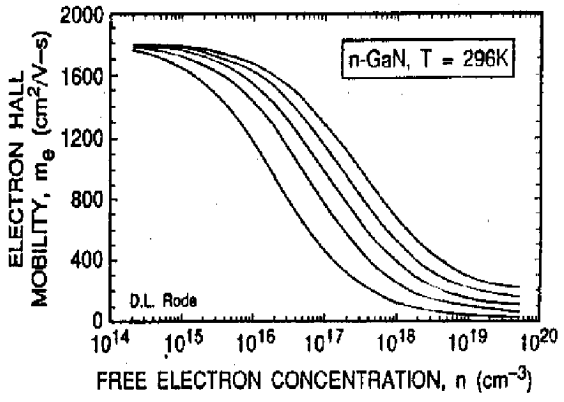

Fig. 3: Theoretical Hall mobility versus free electron concentration calculated by Rode [2].

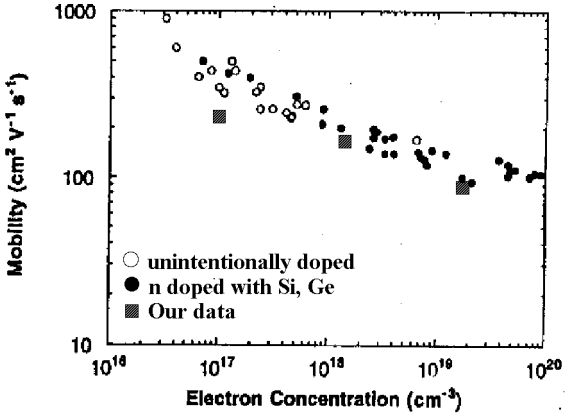

Fig. 4: 300 K Hall mobilities versus free electron concentration for GaN from various groups using both MOVPE and MBE for the growth [2]. The filled squares show our measured results for GaN.

The calculations do not take into account that the carrier mobility is limited by scattering at crystal defects. Therefore, we assume that the measured lower mobilities are limited by high dislocation densities, grain boundaries and stacking faults in the examined GaN material. Fig. 5 shows a transmission electron micrograph (TEM) of a MOVPE-grown GaN layer at the interface. Many plane defects perpendicular to the sample surface can be observed which underpins the above mentioned assumption.

The comparison of CV measurements and Hall measurements show that for most of the samples grown by both techniques the unintentionally doping is homogeneous in the whole layer thickness. Therefore we assume that the dislocations do not form significant amounts of deep traps or electron donors despite their high density at the interface.

The two ways of growing finally involve that the surfaces and also the size of growing islands differ. MBE leads to quite smooth surface and almost equal sized islands, whereas MOVPE yields a rough, completely nonperiodic one. Figs. 6 and 7 are a comparison of two atomic force micrographs (AFM) of GaN samples grown by GSMBE and MOVPE.

Fig. 5: TEM micrograph of MOVPE grown GaN at the interface.

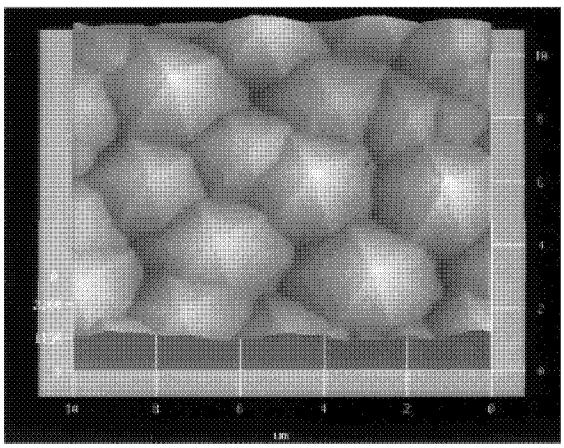

Fig. 6: AFM micrograph of a GSMBE grown GaN sample. The examined area on the surface is 5 μm $\times$ 5 μm. The RMS roughness is 127 Å.

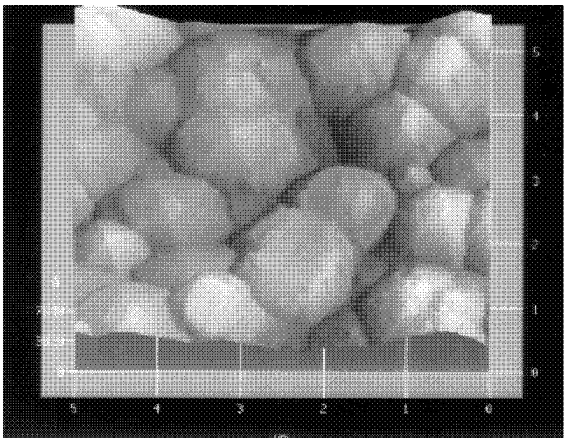

Fig. 7: AFM micrograph of a MOVPE grown GaN sample. The examined area on the surface is 5 μm $\times$ 5 μm. The RMS roughness is 646 Å.

The aim of our GaN growth optimization is to decrease the unintentional background carrier concentration and to increase the crystalline and optical quality. Fig. 8 shows a rocking curve of a MOVPE sample after optimization. The very small linewidth is an indication to the good crystalline quality of the layer. Pendellösung fringes are clearly resolved in the rocking curve. They can be used to calculate the layer thickness which is about 224 nm.

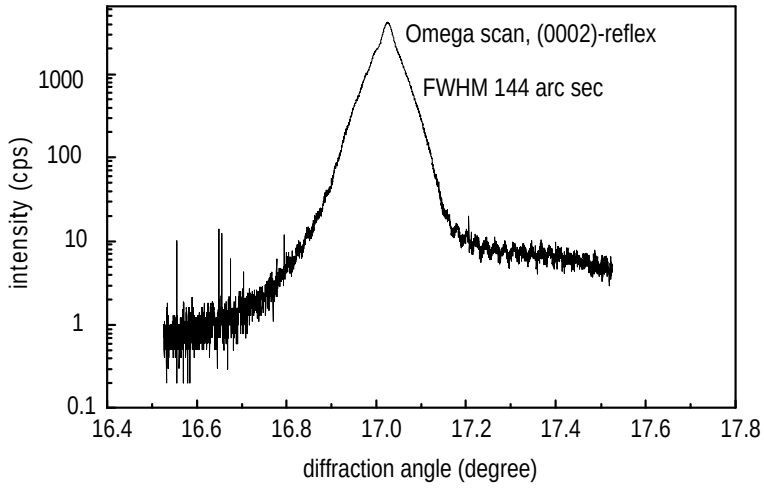

Fig. 8: Rocking curve of a MOVPE-grown GaN sample. Thickness fringes can clearly be seen in the viewgraph. The calculated thickness of the layer is 224 nm.

PL also marks high density of vacancies, visible through a wide middle bandgap transition. Aiming to decrease this yellow luminescence, normally centered at about 2.3 eV (approx. 540 nm) with variable width from 300 to 700 meV, and improvement of the signal output of the near bandgap transitions, the different growth techniques yielded results illustrated in the viewgraphs of Fig. 9 and Fig. 10.

Investigation of the temperature dependent photoluminescence in the near bandgap energy region of wurtzite GaN is compared with a Varshni-Fit of the bandgap energy [5]:

$$E_g(T) = 3.503 + \frac{5.08 \times 10^{-4} T^2}{T - 996} eV$$

The viewgraph in Fig. 11 shows the peak positions of a GSMBE sample compared to the Varshni fit of the GaN bandgap.

As one can see, our values differ from the Varshni fit by a average term of about 36.8 meV. The constant difference between the bandgap energy and the measured near bandgap transitions should equal to excitonic binding energies. These energies can be calculated using effective mass theory. In literature we found values varying between 20 and 25 meV for the binding energy of the free exciton. The difference between the excitonic binding energy (20 - 25 meV) and our measured value (36 meV) can be caused by residual strain in the layer due to different thermal expansion coefficients between layer and sapphire substrate as well as strain fields around dislocations and plane defects.

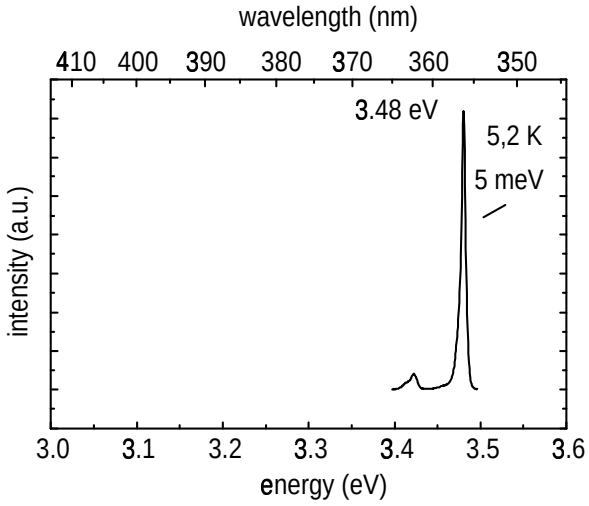

Fig. 9: Photoluminescence of a GSMBE-grown GaN sample at 5 K

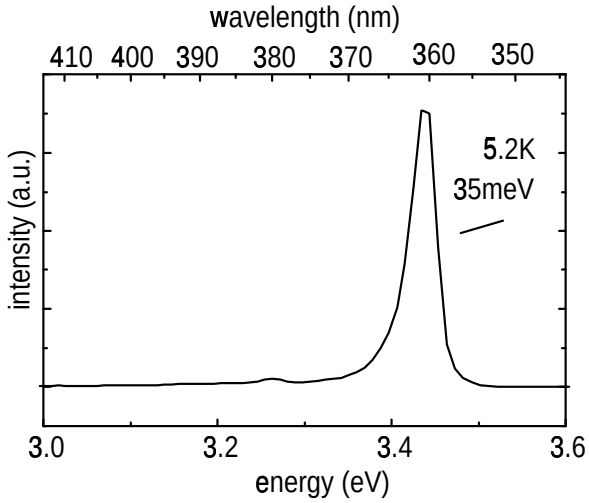

Fig. 10: Photoluminescence of a MOVPE-grown GaN sample at 5 K

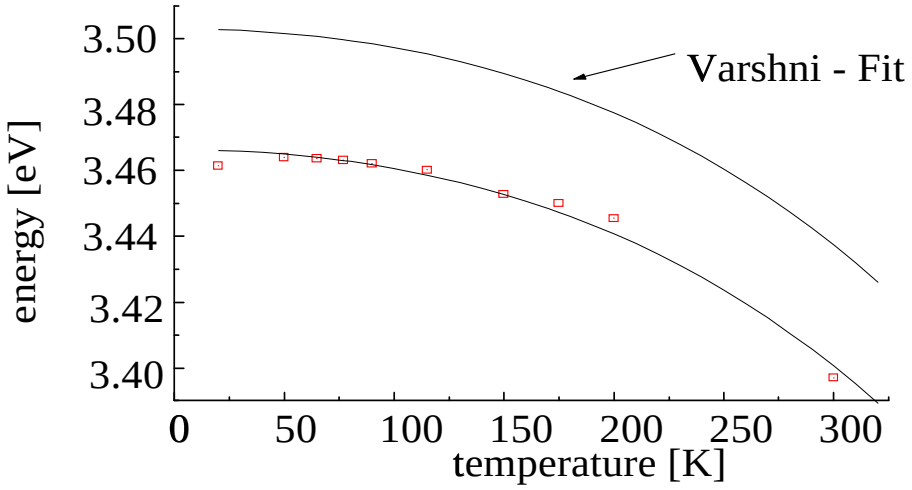

Fig. 11: Varshni - fit of GaN compared with data measured on a GSMBE sample.

Strain not only modifies the bandgap, it might also separate the originally degenerated valence bands of light and heavy holes (lh/hh) and thus increases the number of possible radiative transitions e.g. A-exciton (transition from Γ_{9v}), B/C-exciton (transition from upper/lower Γ_{7v}), DBE (donor bound exciton), ABE (acceptor bound exciton) and phonon replicas etc. Using various substrates and layer thicknesses different data are found in the literature so that a classification of the peaks is not simple. Moreover at low temperatures ($< 50\,\mathrm{K}$) up to 5, in single cases 6 or 7 peaks are reported in the near bandgap region.

4. Summary

Characterization of group III nitrides is carried out using temperature dependent photoluminescence, Hall and CV measurements and x-ray diffraction. These characterization methods yield a feedback for optimization of the semiconductor materials. We find a correlation between the measured Hall mobilities and the linewidths of the x-ray (0002)-reflex for our GaN. Samples with increasing x-ray linewidth show decreasing Hall mobilities. Therefore, we assume that the dislocation density in our samples reduces the free carrier mobility.

Finally AFM measurements show strong differences in surface topography depending on the growth technique.

Temperature dependent near bandgap photoluminescence shows transitions which are shifted for a few meV compared to excitonic lines. The reason for this could be due to the residual strain caused by postgrowth cooling.

5. Acknowledgements

The authors wish to thank H. Sternschulte and M. Mundbrod (Dept. of Semiconductor Physics, University of Ulm) for PL measurements in the temperature range below 10 K, S. Christiansen and W. Dorsch (Dept. of Microcharacterization, University of Erlangen) for AFM and TEM measurements and the German Minister of Education, Science, Research and Technology (BMBF) for the financial support.

References

[1] S. Nakamura, M. Senoh, T. Mukai, "Candela-class high-brightness InGaN/AlGaN double-heterostructure blue-light-emitting diodes," *Appl. Phys. Lett.*, vol. 64, no. 13, pp. 1687-1689, 1994.

[2] D.K. Gaskill, L.B. Rowland, K. Doverspike, "Electrical transport properties of AlN, GaN and AlGaN," *Properties of Group III Nitrides*, EMIS Datareviews Series, vol. 11, pp. 222-230, 1994.

[3] M. Kamp, M. Mayer, A. Pelzmann, A. Thies, H.Y. Chung, H. Sternschulte, O. Marti, K.J. Ebeling, "NH_3 as nitrogen source in MBE growth of GaN," *Proceedings of Topical Workshop on III–V Nitrides (TWN 95)*, Nagoya, Japan, 1995.

[4] M. Kamp, M. Mayer, A. Pelzmann, S. Menzel, H.Y. Chung, H. Sternschulte, K.J. Ebeling, "Thermally cracked NH_3 for MBE growth of GaN," accepted for publication, *Materials Research Society (MRS), Fall Meeting 1995*, Boston, USA, 1995.

[5] I. Akasaki, H. Amano, "Basic optical properties, photoluminescence and cathodoluminescence of GaN and AlGaN," *Properties of Group III Nitrides*, EMIS Datareviews Series, vol. 11, pp. 222-230, 1994.

[6] J.E. Ayers, "The measurement of threading dislocation densities in semiconductor crystals by X-ray diffraction," *J. Crystal Growth*, vol. 135, pp. 71-77, 1994.

[7] S.C. Strite, "Extended structural defects in heteroepitaxial group III nitride films," *Properties of Group III Nitrides*, EMIS Datareviews Series, vol. 11, pp. 258-261, 1994.

[8] S.C. Strite, "Native defects in the group III nitrides," *Properties of Group III Nitrides*, EMIS Datareviews Series, vol. 11, pp. 268-271, 1994.

Gas-Source Molecular Beam Epitaxy of Semiconductor Structures on the Base of InGaAs(P)/InP

Hin Yiu Chung, Dirck Sowada, Torsten Wipiejewski

We investigated the Gas-Source Molecular Beam Epitaxy (GSMBE) growth of InGaAs(P) layers and heterostructures on InP substrates. X-ray and Photoluminesence(PL) measurements indicate that our InGaAs(P) epilayers are of good device quality. InGaAs/InP MQWs structures with 6 meV PL-Full Width Half Maximum (FWHM) measured at 10 K have been also successfully grown. Laser diodes with compressively strained InGaAs/InGaAsP Multiple Quantum Wells (MQWs) as active layers have been grown, fabricated and tested. Under pulsed condition, the laser diodes exibit a theshold current density j_{th} of 1.2 kAcm^{-2}.

1. Introduction

Impressive progress has taken place in the past few years in the development of optical interconnects and optical fiber communication systems. The driving force of these new technologies is the availability of high quality semiconductor laser diodes and photodectors working in the long wavelength regime. Laser diodes on the base of InGaAs(P)/InP with an emission wavelength of 1.5 μm therefore enjoy particular interest in industries as optical sources for low-loss optical fiber communications. The gas source molecular beam epitaxy (GSMBE) technology is well suited for the growth of sophisticated and complex laser structures on the base of InGaAs(P)/InP, owning to its low growth temperature, the possibility of achieving abrupt interfaces, the use of apropriate dopants such as Be and Si, the low system memory effect and the ability of achieving delta dopings. In this article we describe our first results on the growth of InGaAs(P), InGaAs/InP MQWs and laser diodes with strained InGaAs/InGaAsP MQWs as active layer by GSMBE.

2. Epitaxial Procedure

The growth of InGaAs, InGaAsP and InP layers has been carried out in a modified Riber 32 CBE system. The background pressure of the growth chamber lays in the upper 10^{-10} Torr region. Elemental In, Ga and Al served as the group-III sources, while precracked AsH_3 and PH_3 were used as the group-V precursors. Both AsH_3 and PH_3 supplies are regulated by pressure control loops. The cracking of the group-V precursors was carried out at a temperature of 1000 °C in two seperate low pressure gas injectors. Be and Si are used as dopants. All layers have been grown on (100) oriented n^+-InP substrates. The substrates have been either pre-etched with H_2O: H_2O_2 : H_2SO_4 = 1:1:3 etchant before growth or are of epi-ready quality. During nearly all the epitaxial growths, the temperature of the substrates is maintained at 500 °C and is measured by a pyrometer. The growth rates of InP, InGaAs and InGaAsP were 700 nms^{-1}, 1400 nms^{-1} and 970 nms^{-1} respectively. The chamber pressure during growth was in the mid 10^{-5} Torr region.

The crystal quality of the epilayers have been investigated by high resolution x-ray diffraction. Photoluminesence (PL) and Hall measurements were carried out to characterize the optical and electrical properties of the layers.

3. Results

X-ray diffraction measurements have been carried out regularly to control the reproducibility of our epilayers. In the case of the InGaAs layers grown on InP substrates, a lattice matching of around 5×10^{-4} could be routinely achieved. The FWHM of the (004) reflex of all the InGaAs layers are around 23 sec. . Room temperature Hall mobilities of the InGaAs layers are around 10000 $cm^2V^{-1}s^{-1}$ which indicates the high purity of the epilayers. 10 K PL spectra showed a single peak at 1.56 μm with a FWHM of 8 meV. InGaAsP($\lambda_{gap} = 1.3$ μm) layers have also been successfully grown on InP substrates. A lattice matching of down to 4×10^{-4} has been achieved. PL measurements on the samples at 300 K show a single peak at 1.3 μm with a FWHM of around 32 meV and the corresponding FWHMs at 10 K are around 15 meV.

Besides single epilayers, multiple quantum well (MQW) structures were also successfully grown. In Fig.1 the x-ray rocking curve of a InGaAs/InP-MQW structure is shown. The MQW structure consists of four periods of lattice matched 8 nm InGaAs-well/10 nm InP-barrier layers. The cap layer of the structure is a 250 nm thick InP layer. In the rocking curve, a large number of fringes appear on both sides of the (004) reflex of the InP substrate . These fringes were identified to be generated by multiple reflections of the incident x-ray beam between the lower and upper interfaces of the InP cap layer. This observation shows the high crystal quality of the InP cap layer. Furthermore, high order satelite peaks can also be observed on both sides of the substrate reflex which indicate the good crystal quality of the MQWs. PL measurements of the MQW structure is shown in Fig.2. At 300 K a single peak centered at 1.55 μm with a FWHM of 36 meV has been observed. At 10 K the FWHM of the PL peak is reduced to 6 meV. These results show that the optical property of the MQW structure is of good device quality.

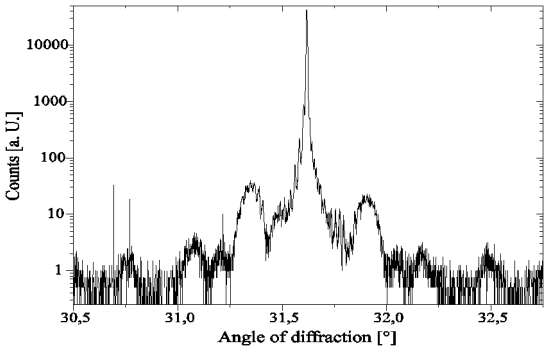

Fig. 1: X-ray rocking curve corresponding to a 4×(8 nm InGaAs/10 nm InP) MQW structure grown lattice matched to InP.

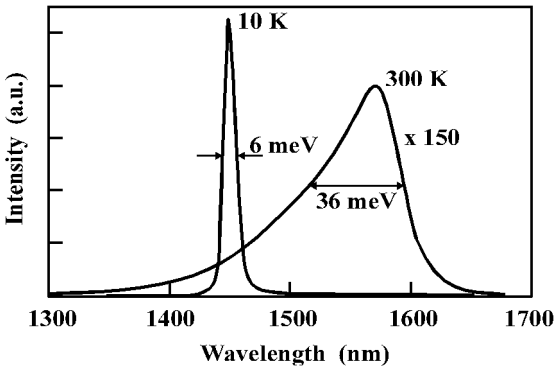

Fig. 2: PL spectra of a 4×(8 nm InGaAs/10 nm InP) MQW structure measured at 10 K and 300 K.

4. Laser Diodes with Compressively Strained MQW Active Layer

Laser structures with three compressively strained $In_{0.72}Ga_{0.28}As$/InGaAsP (λ= 1.3 μm) MQWs as active layer have been grown for the further investigation on the reliability of the GSMBE system as a device manufacturing tool. In Fig. 3 the epilayer structure of the laser diodes is shown. Laser bars with a width of 20 μm and the length of 420 μm have been fabricated from these epilayers and tested. Under pulsed operation, our lasers yield a theshold current density j_{th} of 1.2 $kAcm^{-2}$. The emission wavelengths of the devices are around 1.6 μm. In Fig.4, the output power of a laser bar is shown as a function of the driving current.

Fig. 3: Layer structure of a laser diode with compressively strained InGaAs/InGaAsP MQWs active layer

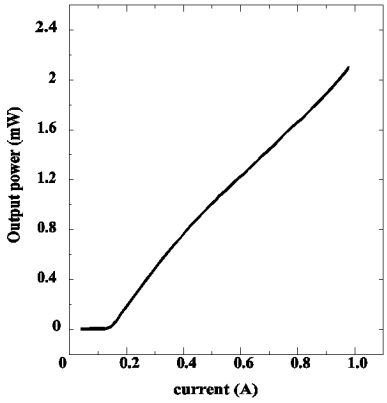

Fig. 4: Typical L-I characteristic of a laser diode with a width of 20 μm and a length 420 μm.

5. Summary

We have successfully grown InGaAs and InGaAsP epilayers by GSMBE. X-ray and PL mesurements indicate that our epilayers are of good device quality. InGaAs/InP MQW structures with 10 K PL-FWHM at 6 meV have also been successfully achieved. To further investigate the reliability of the GSMBE system, laser structures with compressively strained InGaAs/InGaAsP MQWs active layer have been grown and tested. Under pulsed condition, our laser diodes exibit a threshold current density j_{th} of 1.2 kAcm^{-2}

6. Acknowledgments

The authors wish to thank Prof. H. Heinecke (Dept. of Semconductor Physics, University of Ulm) and K. Panzlaff (Bosch Telecom, Backnag) for helpful discussions, B. Henle, M. Kohler and R. Rösch for technical support.

Growth of VCSELs with GaAs Quantum Wells

Gernot Reiner

This report deals with the growth, and the structure design of a vertical-cavity surface-emitting laser (VCSEL) with GaAs quantum wells. VCSELs with AlGaAs/AlGaAs top p-doped mirrors have threshold voltages around 2 V while those with AlAs-AlGaAs mirrors have threshold voltages around 6 V. The maximum wall-plug efficiency for a 4 µm device is 26 %. Using As_2 instead of As_4 as the arsenic species allows the growth of high quality material at growth temperatures below 680 °C.

1. Introduction

Short wavelength vertical-cavity surface-emitting lasers are attractive light sources for optical interconnects. During the last year, there has been a tremendous improvement in the operation characteristics of these devices due to lateral current confinement by selective oxidation. VCSELs with $In_{0.2}Ga_{0.8}As$ quantum wells now have wall-plug efficiencies of more than 50 % [1] [3]. On the other hand VCSELs emitting around 850 nm are prefered in optical interconnects since they allow the use of Si or GaAs photodetectors. This makes it necessary to replace the $In_{0.2}Ga_{0.8}As$ quantum wells by GaAs quantum wells or even more sophisticated InAlGaAs quantum wells. Growth experiments and structure design of VCSELs with GaAs quantum wells are discussed in detail in this report..

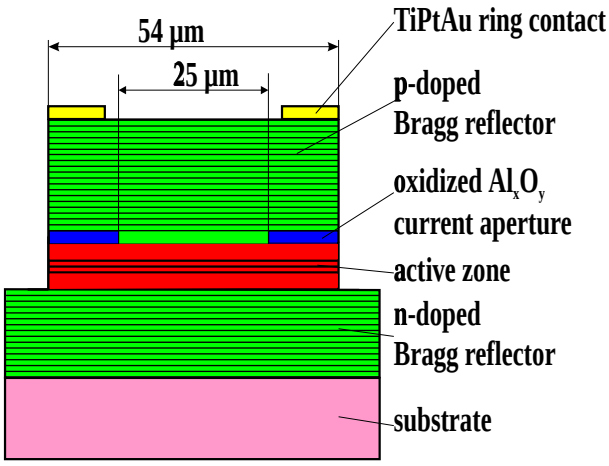

Fig. 1: Structure of an oxidized VCSEL.

The VCSEL structure investigated is sketched in Fig. 1. The active region contains three 8 nm thick GaAs quantum wells with $Al_{0.2}Ga_{0.8}As$ barriers embedded in $Al_{0.5}Ga_{0.5}As$ spacer layers. The lower mirror consists of AlAs-$Al_{0.2}Ga_{0.8}As$ quarter-wavelength layers. However, the last four mirror pairs close to the active region are composed of $Al_{0.9}Ga_{0.1}As$-$Al_{0.2}Ga_{0.8}As$ to prevent the oxidation of layers in the lower mirror in the following step of selective oxidation. The upper mirror is composed of $Al_{0.9}Ga_{0.1}As$- $Al_{0.2}Ga_{0.8}As$ quarter-wavelength layers. Between the high and low index layers 5 nm thick $Al_{0.5}Ga_{0.5}As$ layers reduce the electrical series resistance of the

distributed Bragg reflector. A 30 nm thick AlAs layer is placed in the first low index layer of the upper Bragg reflector for current confinement by selective oxidation. After the chemical etching of mesas, this AlAs layer is oxidized and top TiPtAu ring contacts and broad area bottom AuGeNi n-type contacts are deposited.

2. Growth of the Active GaAs Quantum Wells

GaAs quantum wells have to be grown at relatively high growth temperatures to achieve good material quality. When As_4 is used as the arsenic species, the temperature range from 630 °C to 670 °C has to be avoided since in this temperature range only arsenic deficient layers can be obtained. Growing at high temperatures however, one has to cope with the desorption of gallium from the growing surface.

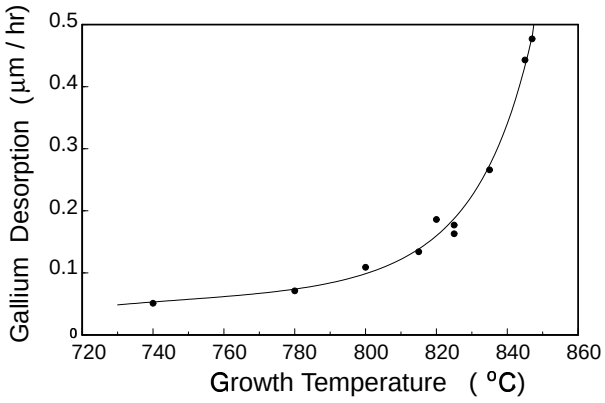

Fig. 2: Gallium desorption as a function of growth temperature.

Fig. 2 shows the onset of gallium desorption with increasing growth temperature taken from [2]. The desorption of gallium does not only change the net growth velocity but also results in composition changes if ternary alloys like AlGaAs have to be grown.

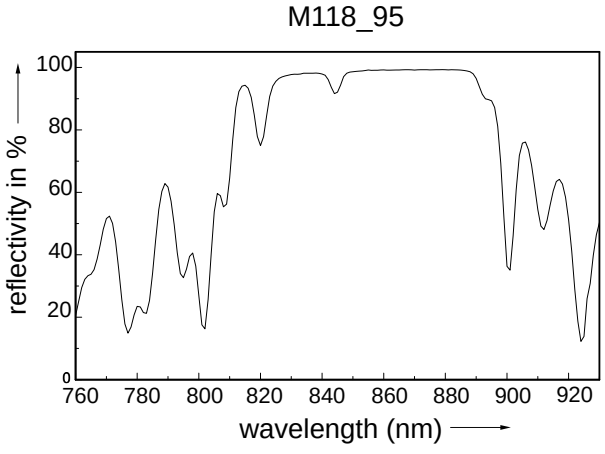

Fig. 3: Reflectivity spectrum of a GaAs QW VCSEL.

Fig. 3 shows a typical reflectivity spectrum of a GaAs VCSEL where no complete compensation for the Gallium desorption has taken place. The inner cavity has been grown at a temperature of 680 °C and growth rates have been compensated for a gallium desorption of 50 nm/h. The cavity mode is shifted towards the short wavelength edge of the stopband. Not only the cavity mode is shifted by the onset of gallium desorption but also the gain maximum of the quantum

wells is shifted since quantum well thickness as well as barrier height depend on growth temperature. Therefore it is more difficult to adjust cavity mode and gain maximum at these relatively high growth temperatures. To weaken the problems arising from growing under high gallium desorption a arsenic valved cracker cell has been installed in the MBE-System. This source allows to use As_2 for the growth of GaAs and related compounds. Using As_2, it is possible to grow in the temperature range from 630 °C to 670 °C with good surface morphologies. Fig. 4 shows the output characteristics of a 25 μm device grown at a substrate temperature of 650 °C. Although gain maximum and cavity resonance are strongly detuned the device reaches a maximum output power of 2 mW. This shows the potential of growing high-quality material at rather low substrate temperatures. Fig. 5 shows the output characteristics of a 4 μm device with the very same structure fabricated from sample M118/95 grown at 680 °C. In this structure, gain maximum and cavity resonance are aligned much better. This results in devices with wall-plug efficiencies up to 26 %.

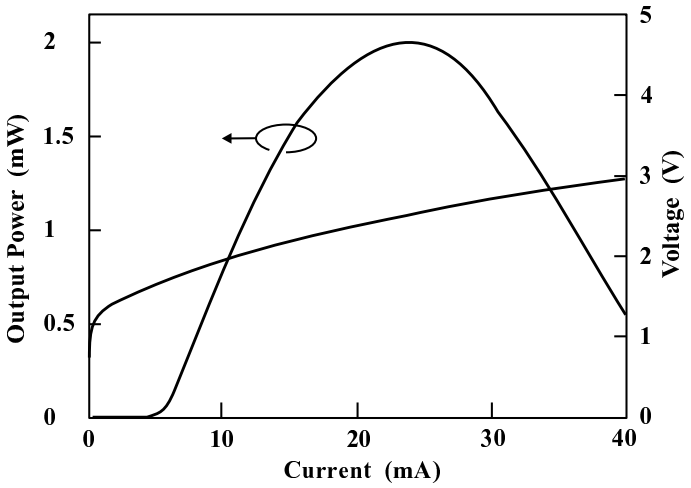

Fig. 4: 25 μm VCSEL device from sample M117/95 grown at $T_{Substr.} = 650$ °C.

3. Carbon Doping of AlGaAs Heterostructures

A significant reduction in the series resistance of the p-doped Bragg reflector has already been achieved by replacing an AlAs-$Al_{0.2}Ga_{0.8}As$ mirror by an $Al_{0.9}Ga_{0.1}As$-$Al_{0.2}Ga_{0.8}As$ mirror. Threshold voltages of VCSELs with the first mirror design are in the range of 5-6 V [4]. Threshold voltages for VCSELs with the second mirror design are in the range of 2 V. However a further reduction in threshold voltage and serie resistance could probably only be achieved with carbon as the p-type dopant. Among the serveral possible carbon sources available best results were achieved using carbontetrabromide (CBr_4) as dopant gas [5] [6]. CBr_4 is a white cristalline solid which has a relatively high vapor pressure of around 0.9 Torr at 300 K. This allows the direct injection of CBr_4 vapor into the growth chamber without any carrier gas. Fig. 5 shows the system that is built up for carbon doping using CBr_4.

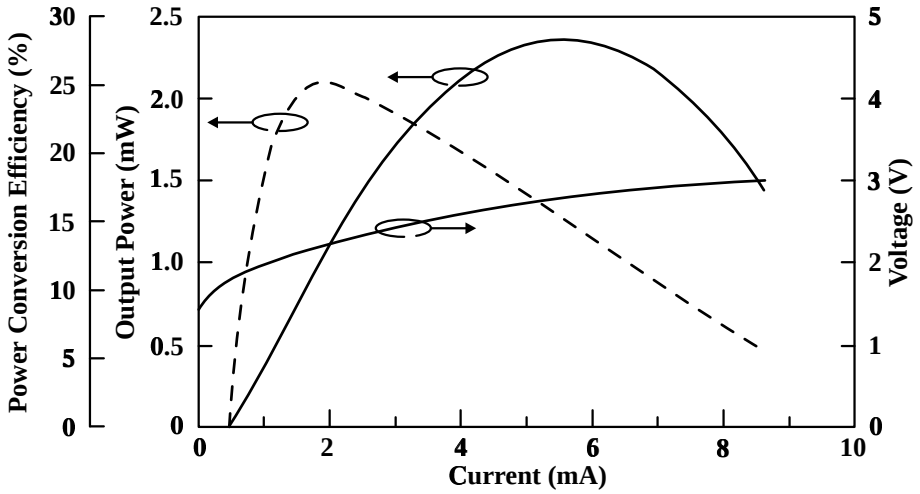

Fig. 5: 4 μm VCSEL device from sample M118/95 grown at $T_{Subst.} = 680\,°C$.

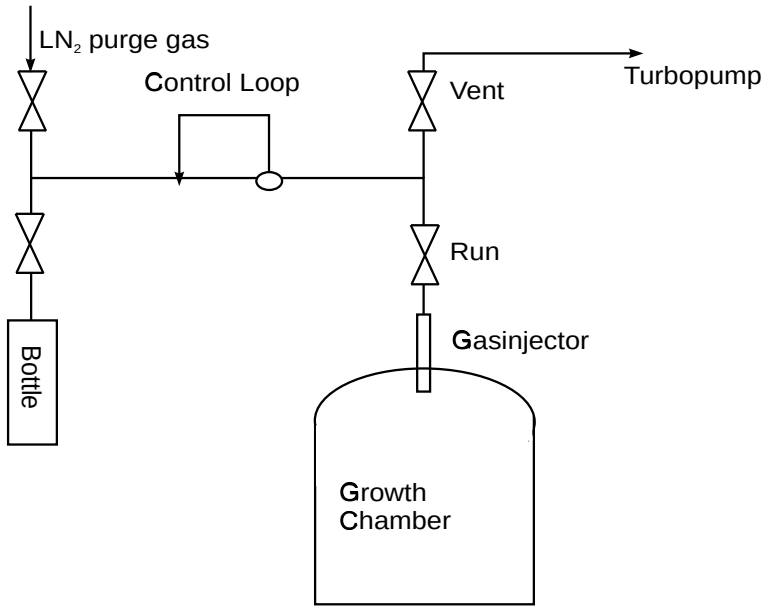

Fig. 6: Schematic of the system for carbon doping with CBr_4

4. Conclusion

VCSELs with emission wavelengths of around 850 nm have been realized containing GaAs quantum wells. Samples grown at temperatures of 680 °C reach wall-plug efficiencies of up to 26 %. The driving voltages of the devices are below 3 V. It has been shown that the use of As_2 instead of As_4 allows the growth of high quality material at reduced substrate temperatures. A system for carbon doping with CBr_4 has been set up. This gives the prospect for a further reduction in the series resistance of the devices and therefore improved device characteristics.

References

[1] K.L. Lear, K.D. Choquette, R.P. Schneider, Jr., S.P. Kilcoyne, K.M. Geib, "Selectively oxidised vertical cavity surface emitting lasers with 50 % power conversion efficiency," *Electron. Lett.*, vol. 31, no. 3, pp. 208-209, February 1995.

[2] S.V. Iyer, H.P. Meier, S. Ovadia, C. Parks, "Role of substrate temperature in molecular-beam epitaxial growth of high-power GaAs/AlGaAs layers," *Appl. Phys. Lett*, vol. 60, no. 4, pp. 416-418, January 1992.

[3] B. Weigl, G. Reiner, M. Grabherr, K.J. Ebeling, "High power selectively oxidized vertical-cavity surface-emitting lasers," *submitted to CLEO'96*

[4] B. Weigl, "VCSELs with active GaAs QW," *Annual Report 1994, Department of Optoelectronics, University of Ulm*, pp. 18-21, January 1994.

[5] Y.M. Houng, S.D. Lester, D.E. Mars, J.N. Miller, "Growth of high-quality p-type GaAs epitaxial layers using carbon tetrabromide by gas source molecular-beam epitaxy and molecular-beam epitaxy," *J. Vac. Sci. Technol. B*, vol. 11, no. 3, pp. 915-918, May/Jun 1993.

[6] W.E. Hoke, D.G. Weir, P.J. Lemonias, H.T. Hendriks, "Carbon tetrabromide carbon doping of molecular beam epitaxial GaAs films," *App. Phys. Lett.*, vol. 64, no. 2, pp. 202-204, January 1994.

Selective Oxidation of AlGaAs Layers

Martin Grabherr, Bernhard Weigl

Recently, it has been shown that the use of selectively oxidized AlGaAs layers for current confinement can improve the performance of semiconductor lasers [1] [2]. Therefore, an experimental setup for the oxidation process has been established and detailed investigations on process parameters have been carried out.

1. Oxidation Setup

The selective oxidation process is usually done in an N_2/H_2O atmosphere at temperatures from 380 °C to 550 °C [3]. Fig. 1 shows a schematic sketch of the oxidation setup. It generally consists of two main parts, a bubbler system and an oxidation furnace.

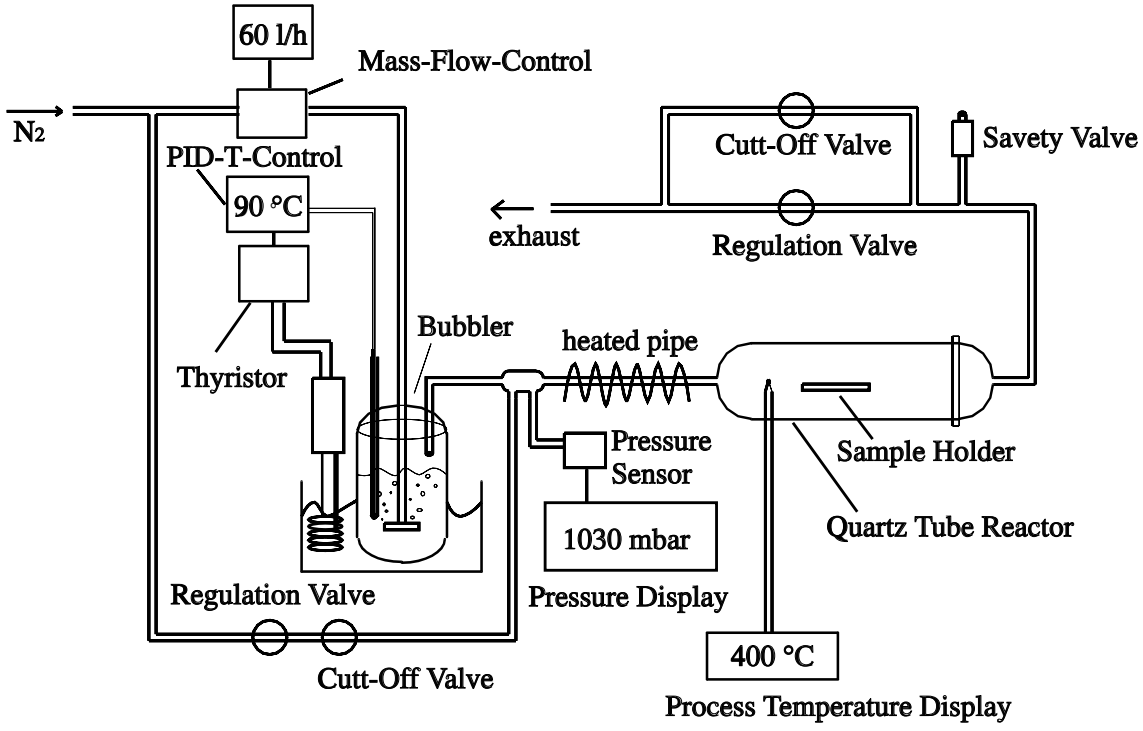

Fig. 1: Schematic structure of the oxidation system

To obtain a reproducible loading of the N_2 gas with water vapor, nitrogen flow, temperature of the deionized water in the bubbler, and system pressure have to be controlled. The supplying gas lines are heated to 120 °C to avoid any recondensation and thereby reduction of the water vapor concentration in the carrier gas before being injected into the furnace. A three zone furnace

with a relatively long reactor oven offers a stable and precisely adjustable process temperature in the quartz glas tube. Pressure control is done by a regulation valve in the exhaust pipe. Two bypass pipes are included to flood the reactor with cold and dry nitrogen in order to stop the chemical reaction.

2. Oxidation Process

For a calibration of the oxidation rates for different materials and process parameters, some tests have been done. In order to obtain reproducible oxidation rates, the supply of water vapor which is set by the two parameters, gas flow and bubbler temperature, has to be higher than it is necessary for a reaction-rate limited oxidation process. Oxidation tests at this conditions, we call it saturation, show maximum oxidation rates for fixed process temperatures and the oxide depth then grows linear with time. As we could see, oxidation rates are then determined by Al concentration, process temperature, and layer thickness.

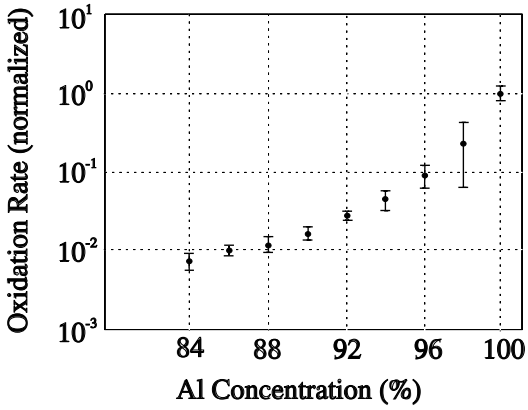

Fig. 2: Oxidation rate versus Al concentration.

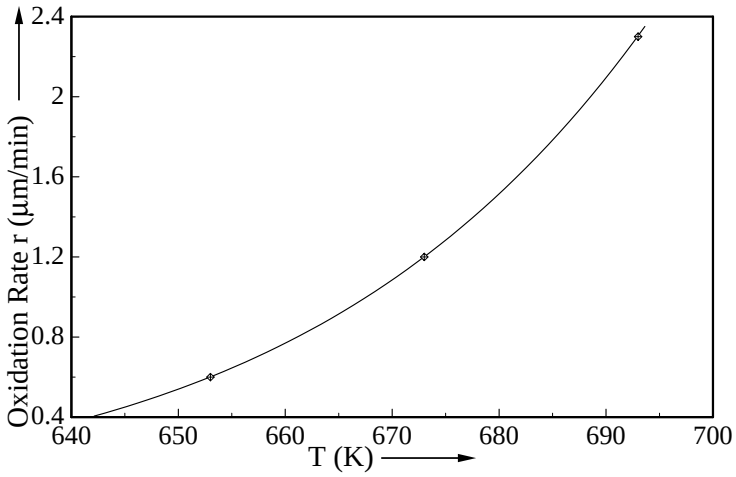

Fig. 3: Oxidation rate versus process temperature for a 27-nm-thick AlAs layer.

The dependency of the oxidation rate on the Al concentration is depicted in Fig. 2 [2]. The logarithmic plot shows a strong selectivity especially for high Al concentrations. The oxidation rate of $Al_{0.88}Ga_{0.12}As$ for example is reduced by a factor of 100 compared to that of pure AlAs. Fig. 3 shows the temperature dependence of the oxidation process for a 27 nm AlAs layer. The rate plotted in the temperature range from 380 °C to 420 °C varies from 0.6 μm/min to 2.3 μm/min and can be fitted by an exponential law.

$$r(T) = r_0 \cdot \exp\left(\frac{-E_a}{kT}\right) = 7.75 \cdot 10^9 \frac{\mu\text{m}}{\text{min}} \cdot \exp\left(\frac{-1.31\text{eV}}{kT}\right)$$

For this very thin layer, a dependency of the oxidation rate on the layer thickness can be seen. A more detailed examination with specially-prepared samples is presented in Fig. 4.

Even for extreme oxidation depth and aspect ratios of oxide thickness to depth (more than 1 : 2000), a stable oxidation rate of 1.2 μm/min for this 27-nm-thick AlAs layer at a process temperature of 400 °C is detected, which is shown in Fig. 5.

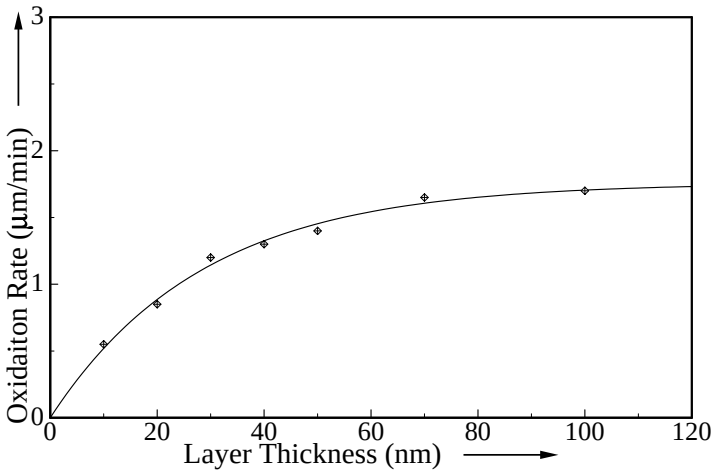

Fig. 4: Oxidation rate for different AlAs layer thicknesses.

3. Summary

The investigations on the oxidation process showed that it is a very advantageous tool in laser processing. The high selectivity forms thin oxide layers, that work as effective current apertures in laser structures. The reduced refractive index of the oxide ($n = 1.55$) can induce an optical index guiding. Process temperature can be chosen low enough to avoid diffusion in the AlGaAs system and processing time is short. Linearity in time allows easy scaling for different device geometries. Used substances are as cheap and harmless as possible.

Very good characteristics of VCSELs (vertical-cavity surface-emitting lasers) oxidized by using the presented system [4] [5] confirm the application in laser processing. A little more should be

known about the chemistry of the process and long time stability of the manufactured devices. But it seems that selective oxidation will be one of the favorite processing tools for future laser device technology.

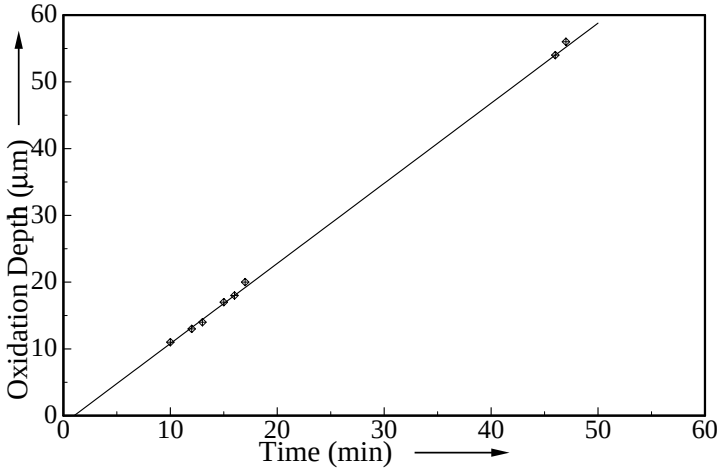

Fig. 5: Oxidation depth of a 27-nm-thick AlAs layer versus time at a process temperature of 400 °C

References

[1] K.L. Lear, K.D. Choquette, R.P. Schneider, Jr., S.P. Kilcoyne, K.M. Geib, "Selectively oxidized vertical cavity surface emitting lasers with 50% power conversion efficiency," *Electron. Lett.*, vol. 31, no. 3, pp. 208-209, 1995.

[2] K.D. Choquette, R.P. Schneider, Jr., K.L. Lear, K.M. Geib, "Low treshold voltage vertical-cavity lasers fabricated by selective oxidation," *Electron. Lett.*, vol. 24, no. 30, pp. 2043-2044, 1994.

[3] H. Nickel, "A detailed experimental study of wet oxidation kinetics of $Al_xGa_{1-x}As$ layers," *J. Appl. Phys.*, vol. 78, no. 8, pp. 5201-5203, 1995.

[4] B. Weigl, M. Grabherr, G. Reiner, K.J. Ebeling, "High efficiency selectively oxidized MBE grown vertical-cavity surface-emitting lasers," submitted to *Electron. Lett.*, October 1995.

[5] B. Weigl, G. Reiner, M. Grabherr, K.J. Ebeling, "High-Power Selectively-Oxidized Vertical-Cavity Surface-Emitting Lasers",
submitted to *CLEO, Anaheim, California*, June 1996.

Sputter Etching of GaAs and GaN

Franz Eberhard, Markus Schauler

1. Introduction

Currently available exposure tools and highly sensitive resist materials allow the generation of sub–micrometer pattern sizes. However, the reproducible and controllable transfer of pattern dimensions in the range below 1 μm is impossible with wet chemical etching due to the adhesion of etch solution and the isotropic behaviour. Plasma etching has demonstrated viable solutions to most of the problems encountered with wet etching, with the possible exception of selectivity. Therefore, plasma etching has become the dominant technique for pattering thin films in microelectronics manufacturing.

2. Mechanism of Dry Etching

The chemical part in plasma etching mechanism can be broken down into six steps, as shown in Fig. 1. First, reactive species like atoms, molecules or ions must be generated by electron-molecule collisions. This step is vital in plasma etching because many of the gases used do not or only very slowly react with the substrate. Etchant species diffuse to the surface of the material and adsorb onto a surface site. The sticking coefficient of free radicals in general is large, though there is a high concentration of etchants on the surface. In addition free radicals will chemisorb and react with the solid surface. Product desorption is a critical step in the etch process. A free radical can react rapidly with a solid surface, but unless the product species has a reasonable vapor pressure so that desorption occurs, no etching takes place. If any of these individual processes does not occur, the overall etch cycle terminates.

A second point, which must be considered in dry etching is the bombardment of the surfaces by ions. This ion bombardment can break surface bonds, thereby creating adsorption sites as well as assisting reaction or product desorption. Energetic ions can also eject surface atoms by momentum transfer. This bombardment gives rise to the anisotropic etch profiles.

The simplest etching system is the barrel reactor. This configuration generally uses a cylindrical chamber with RF power applied to external electrodes. The wafer is placed on a holder within the chamber. A metal cage confines the glow region and shields the substrates from energetic ions and electrons in the plasma. Because of this shielding, only radicals can reach the substrates and perform the etching. In this case, the reaction is purely chemical, resulting in an isotropic etch profile. The main application for barrel systems is resist stripping.

Sputter etching is an etching technique, where the removal of surface atoms is only performed physically. In such systems, a chemically inert gas such as argon is used. Positive argon ions are generated in a glow discharge and are accelerated through an electric field to the substrate. When they strike the substrate, they transfer their momentum to the material. If the ion energy is sufficient, substrate atoms, molecules and ions are ejected and the material is etched.

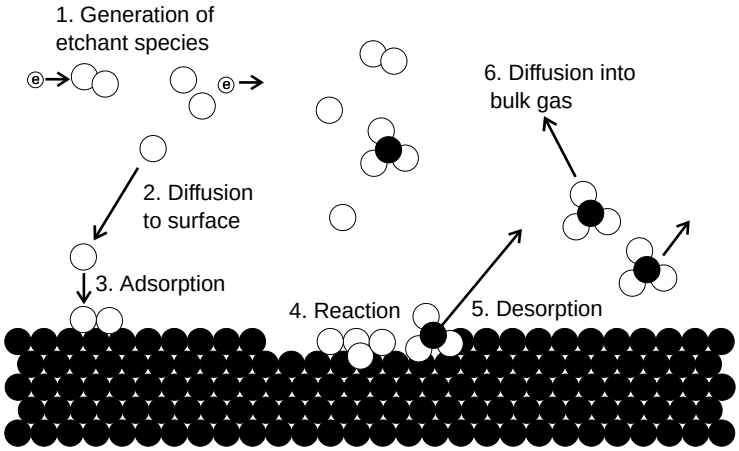

Fig. 1: Chemistry of plasma etching.

Unfortunable, there are some serious drawbacks with sputter etching. The first one is the formation of an sputter trench. High energy argon ions eject secondary ions which can etch the substrate, too. If the pattern to be etched is very narrow the ejected material redeposits on the sidewalls. This can be seen in Fig. 2. Another important effect is the erosion of the mask material exposed to the beam. As a result the sidewalls are tapered.

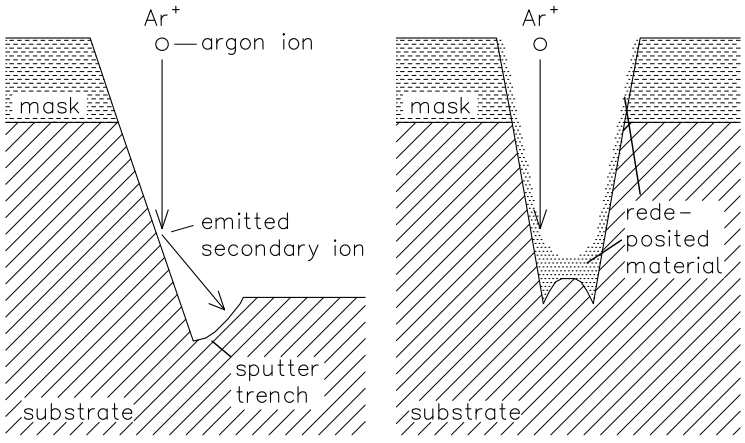

Fig. 2: Trench formation and redeposition.

A combination of chemical etching and sputter etching has some advantages. An enhanced profile control can be achieved, compensating the effects of redeposition and mask erosion. Furthermore, the etch rate is increased drastically compared to physical bombardment only.

The most common type of reactor is the reactive ion etching (RIE) system. In this configuration the wafers lie on the powered electrode within the plasma, so that they are exposed to energetic radiation. The plasma is sustained between the two electrodes, which can have equal or

different areas. The ratio of the areas affects the potential distribution in the plasma. The RIE configuration generally causes the wafers to be subjected to a high–energy ion bombardment. A major limiting feature of the RIE reactor is that ion bombardment flux and energy cannot be controlled independently from each other and from the plasma chemistry. For example, an attempt to increase the ion flux by increasing the rf power causes an increase in sheath potential and in extent gas dissociation in the plasma.

The strong coupling between the internal properties of the plasma has led to new reactor designs where this coupling is reduced. One example is a chemically-assisted ion-beam etcher (CAIBE) shown in Fig. 3. The basic components of this system are the electron-cyclotron-resonance (ECR) ion-beam source which produce argon ions and accelerate them towards the substrate, a substrate holder which can be tilted and rotated, turbo and backing pumps to maintain reduced pressures in the chambers, and a gas mixing system. The transfer gate valve, the transfer rod and a load lock is used to put the substrate into the process chamber without the need of exposing it to air. In addition, a Meissner–trap reduces the water vapor pressure in the process chamber, which is essential for etching Al–containing films. Because the substrate temperature is very important for etch rate and surface morphology, the substrate holder can be heated or cooled in the range of $-20\,^{\circ}\mathrm{C}$ to $120\,^{\circ}\mathrm{C}$. The gas feeding ring supplies this CAIBE system with the echant.

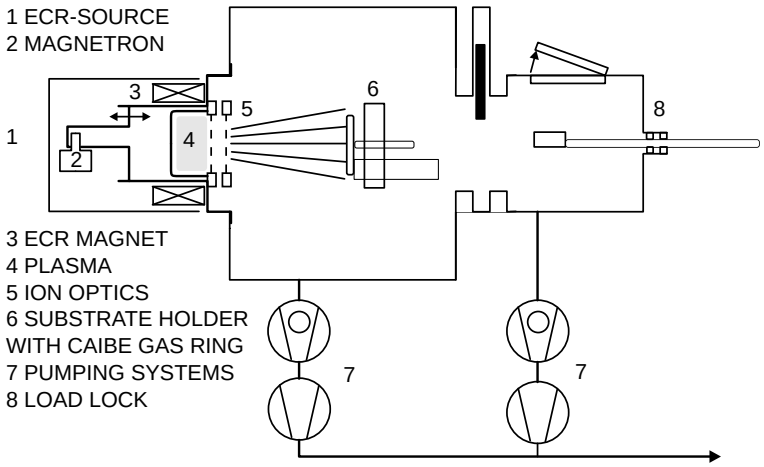

Fig. 3: CAIBE system.

The plasma in the ECR source is sustained by coupling microwave energy to the electrons in the presence of a static magnetic field such that the microwave frequency is in resonance with the electron cyclotron frequency $w = eB/m$, where B is the magnetic field and e and m is the electron charge and mass, respectively. For 2.45 GHz microwaves, the field required to fullfill this equation is $B = 87.5\,\mathrm{mT}$. Electrons gain energy from the microwave electric field as they rotate in phase with the wave.

Two graphite grids enable the ions to be accelerated and collimate the ion beam. In our system, a gas handling system is established, which allowes the control of Ar, BCl_3, and Cl_2 flows. It is well known that with this gases etching of AlGaAs and group–III nitrides is possible.

Supplying the ion-beam source with the etchant, an other dry etch technique, reactive ion-beam etching (RIBE), is possible. This technique is carried out in an manner analogous to ion beam-milling, except that a plasma is established with a chemically reactive gas. The ion source supplies both, the ions and the reactive radicals.

Fig. 4: GaAs sample with large amount of redeposition and rough sidewalls. The photoresist has been removed.

3. Etching Results

Using our CAIBE as a sputter–etching system, we have been able to reproduce the theoretically-expected etch profiles (Fig. 2). Fig. 4 shows a cross-sectional view of a sputter–etched GaAs sample, where the large sputter trench at the base of the sidewall can be seen. The photoresist mask has been removed after the process. A large amount of material is redeposited on the surface. The etch roughness of this sample is far away from being acceptable for optoelectronic applications. Optimization of the sputter process leads to structures shown in Fig. 5, where the sidewalls are much smoother. A small sputter trench can be observed inhibits the forming of etching trenches, but also generates redeposition on the sample surface.

First experiments have been performed on gallium nitride (GaN) samples Fig. 6 shows a sputter-etched GaN struture with a sidewall angle of approximately 45°. This kind of profile is favourable for devices with mesa structures where a good side-wall coverage with a metallization or passivation layer is needed.

Fig. 5: GaAs sample etched with opimized process. The sidewalls are almost steep. A small sputter trench can be observed.

Fig. 6: Sputter-etchted GaN sample with a sidwall angle of approximately 45°.

References

[1] J.A. Mucha, D.W. Hess, E.S. Aydil, "Plasma Etching," in "Introduction to Microlithography, 2nd. edition" edited by L.F. Thompson, C.G. Wilson, M.J. Bowden, *American Chemical Society*, pp. 377-507, 1994.

[2] J. Daleiden, K. Eisele, R.E. Sah, H.K. Schmidt, J.D. Ralston, "Chemical analysis of a $Cl_2/BCl_3/IBr_3$ chemically assisted ion–beam etching process for GaAs and InP laser–mirror fabrication under cryo–pumped ultraghigh vacuum conditions," *J. Vac. Sci. Technol. B.*, vol. 13, no. 5, pp. 2022-2024, 1995.

[3] I. Adesina, A.T. Ping, C. Youtsey, T. Dow, M. Asif Khan, D.T. Olson, J.N. Kuznia, "Characteristics of chemically assisted ion beam etching of gallium nitride," *Appl. Phys. Lett.*, vol. 65, no. 7, pp. 889-891, 1994.

High-Efficiency Selectively-Oxidized MBE-Grown Vertical-Cavitiy Surface-Emitting Lasers

Bernhard Weigl

Performance of Vertical-Cavity Surface-Emitting Laser Diodes (VCSELs) has drastically improved using selective oxidation [1] instead of proton implantation for lateral current confinement. The modified layer structure, the laser processing, and the output characteristics of the new devices are presented. A maximum output power of 47 mW and a maximum power conversion efficiency of 47 % have been achieved for devices with an active diameter of 25 μm and 20 μm in a non heatsinked configuration.

1. Layer Structure

A schematic cross-section of the VCSEL structure under investigation is shown in Fig.1. Growth is done by solid source MBE. The active region contains 3 strained $In_{0.2}Ga_{0.8}As$ quantum wells with GaAs barriers surrounded by $Al_{0.33}Ga_{0.67}As$ layers for efficient carrier confinement. The bottom Bragg reflector consists of 32 n-type Si doped AlAs/GaAs quarter wavelength layer pairs. The 26 pair $Al_{0.67}Ga_{0.33}As$/GaAs p-type Be doped top reflector has an optimized doping profile [2] to reduce the electrical series resistance. A single 30-nm-thick AlAs layer is introduced as the lowest layer in the p-type mirror next to the active region to be used for selective oxidation.

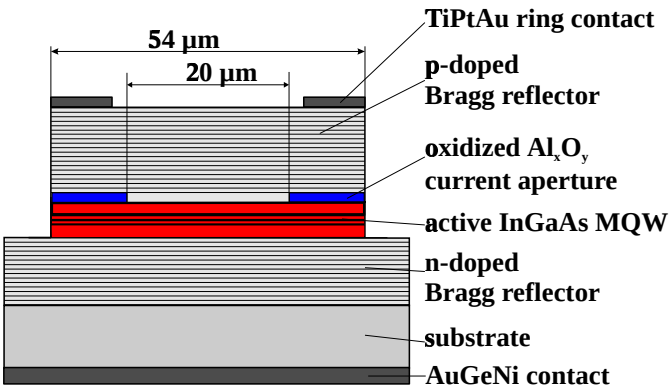

Fig. 1: Schematic drawing of a selectively oxidized InGaAs/AlGaAs VCSEL

Mesas with diameters from 38 to 59 μm have been structured by wet chemical etching using a positive resist mask. Etching has to be stopped immediately after removing the p-doped AlAs layer outside the mesa within an accuracy of $\pm$ 100 nm. This can be achieved using in situ optical monitoring of the etching depth. Subsequent lateral selective oxidation is of the AlAs layer is performed in an N_2/H_2O atmosphere at a temperature of 400 °C [3]. With an oxidation rate of 1.2 μm/min, an oxidation depth of 17 μm is achieved within 15 min of processing time.

This current aperture reduces the active diameters of the devices to 4-25 μm. TiPtAu p-type ring contacts and n-type GeNiAu are deposited to complete the structure.

2. Devices and Measurements

The thin Al_xO_y layer formed by selective oxidation is found to provide excellent current confinement for the injected carriers. Losses caused by nonradiative recombinations, absorption and defraction at the perimeter of the aperture are considerably smaller than in proton implanted devices allowing even small-single mode lasers and enhancing the efficiency of broad-area devices. The refractive index of the oxide is $n = 1.6$ and therefore much smaller than in the semiconductor material. The resonator is detuned in the partially oxidized areas inducing an optical wave guiding that can be described by an effective index method [4]. Theoretical analysis [5] gives an index reduction of $\Delta n_{eff} = 6.5 \cdot 10^{-2}$ for the outer regions. In contrast to proton implanted lasers, optical guiding is well defined and can be adjusted to the device characteristics desired.

Fig.3 shows top side output power, driving voltage, and wallplug efficiency as a function of injection current for a 20 μm active diameter VCSEL. Threshold current and threshold voltage are 3 mA and 1.65 V, respectively. Due to the differential resistance of less than 40 Ω under lasing conditions, driving voltage remains below 3.5 V up to the maximum output power of 40 mW which is limited by thermal rollover in the non heat sinked device. Optical output power is measured using a Newport 835 optical power meter with calibrated wavelength selective detector. Maximum wallplug efficiency of 47 % is observed for a driving current of 10 mA at an output power of 10.2 mW. The high power conversion efficiency is mainly due to high optical gain represented by a top side differential quantum efficiency of about 90 %. Losses are estimated to be caused by series resistance and leakage current (41 %), bottom emission (5 %) as well as residual non-radiative recombination and internal absorption in mirrors and active region (7 %).

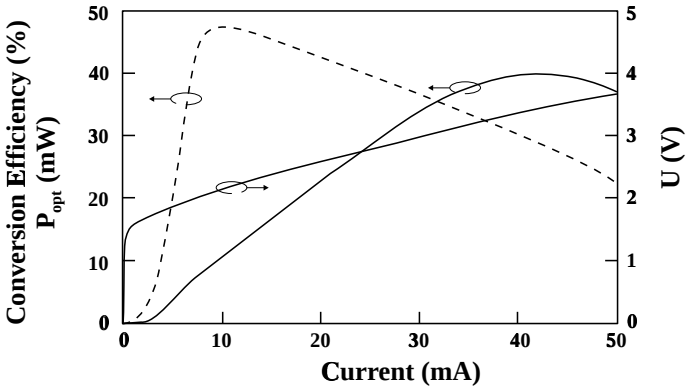

Fig. 2: Output power P_{opt}, conversion efficiency (dashed), and voltage U as function of driving current for a VCSEL of 20 μm diameter

The emission spectrum in Fig. 3 recorded at 15 mA driving current centered at 983 nm wavelength is relatively broad. The appearance of several transverse modes oscillating simultaneously is typical for an index guided VCSELs.

We believe that the high conversion efficiency observed in 20 μm diameter devices is due to very efficient optimum index guiding provided by the 30-nm-thick oxidized layer. VCSELs

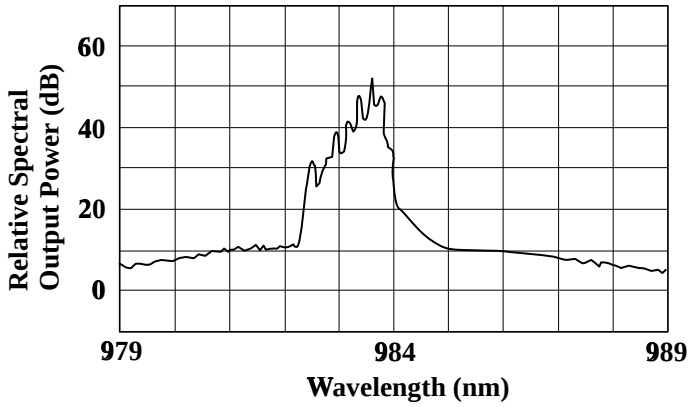

Fig. 3: Emission spectrum of 20 μm VCSEL at 15 mA driving current

of larger active sizes of 25 μm show larger maximum output powers of 50 mW with slightly reduced conversion efficiencies due to current crowding effects at the edges. Generally it is found that selectively-oxidized devices are about three times as efficient as proton implanted devices produced from the very same wafer.

3. Conclusion

We have demonstrated that extremely efficient VCSELs can be fabricated using conventional solid source MBE with Be p-type dopant for wafer growth,a simple wet etching and subsequent lateral AlAs single layer oxidation. The maximum wallplug efficiency is as high as 47 % at 10 mW output power while maximum output power is above 40 mW in devices with an aperture diameter of 20 μm. High efficiency combined with high output power is favorable for producing high-power densely-packed two-dimensional arrays.

References

[1] K.L. Lear, K.D. Choquette, R.P. Schneider, Jr., S.P. Kilcoyne, K.M. Geib, "Selectively oxidized vertical cavity surface emitting lasers with 50 % power conversion efficiency," *Electron. Lett.*, vol. 31, no. 24, pp. 208-209, 1995.

[2] G. Reiner, E. Zeeb, B. Möller, M. Ries, K.J. Ebeling, "Optimization of Planar Be-Doped InGaAs VCSELs with Two-Sided Output," *Photon. Technol. Lett.*, vol. 7, pp. 730-732, 1995.

[3] M. Grabherr, B. Weigl, "Selective Oxidation of AlGaAs Layers," *Annual report*, Department of Optoelectronics, University of Ulm, 1995.

[4] G.R. Hadley, "Effective index model for vertical-cavity surface-emitting lasers," *Optic Letters*, vol. 20, no. 13, pp. 1483-1485, 1995.

[5] R. Michalzik, "Simple Understanding of Waveguiding in Oxidized VCSELs," *Annual report*, Department of Optoelectronics, University of Ulm, 1995.

Ph.D. Theses

1. E. Zeeb, *Planar Vertical Cavity Laser Diodes and Two-Dimensional Laser Diode Arrays for Optical Interconnects*, Ph.D. Thesis, Dept of Optoelectronics, University of Ulm, 1995.

2. B. Möller, *Emission Properties and High Frequency Behavior of Vertical Cavity Laser Diodes for Optical Interconnects*, Ph.D. Thesis, Dept of Optoelectronics, University of Ulm, 1995.

3. A. Fricke, *Waveguide Integrated-Metal-Semiconductor-Metal Photodiodes and Modulators in InAlGaAs on InP Substrate for Optical Communications*, Ph.D. Thesis, Dept of Optoelectronics, University of Ulm, 1995.

4. C. Rompf, *Optoelectronic Devices Based on Organic Semiconductors*, Ph.D. Thesis, Dept of Optoelectronics, University of Ulm, 1995.

Diploma Theses and Semester Projects

1. Böhler, Achim, *Untersuchungen der elektrischen und optischen Eigenschaften von organischen Heterostrukturen*, Diploma Thesis, Dept. of Optoelectronics, University of Ulm, 1994.

2. Ries, Manfred, *Einzeln adressierbare oberflächenemittierende Laserdiodenmatrizen*, Diploma Thesis, Dept. of Optoelectronics, University of Ulm, 1995.

3. Schauler, Markus, *Untersuchung schneller Ladungstransportvorgänge in Halbleiterstrukturen auf GaAs- und InP-Basis*, Diploma Thesis, Dept. of Optoelectronics, University of Ulm, 1995.

4. Zitzler, Rainer, *Untersuchungen zur Dynamik des Ladungsträgertransports in anorganisch-organischen Heterostrukturen*, Diploma Thesis, Dept. of Optoelectronics, University of Ulm, 1995.

5. Busin, Rainer, *Untersuchungen der elektrischen und optischen Eigenschaften von AlGaAs Braggreflektoren oberflächenemittierender Laserdioden*, Diploma Thesis, Dept. of Optoelectronics, University of Ulm, 1995.

6. Schmid, Volker, *Charakterisierung von oberflächenemittierenden Laserdoden mit AlGaAs/AlAs Bragg-Reflektoren*, Diploma Thesis, Dept. of Optoelectronics, University of Ulm, 1995.

7. Mayer, Markus, *Wachstum und Charakterisierung von verspannten GaAsP/InGaAs Heterostrukturen mit Gasquellen-Molekularstrahlexpitaxie*, Diploma Thesis, Dept. of Optoelectronics, University of Ulm, 1995.

8. Wiegand, Christian Walter, *Untersuchungen der "Spannungskompensation" in InGaP Qauntentöpfen auf GaAs für Laseranwendungen*, Diploma Thesis, Dept. of Optoelectronics, University of Ulm, 1995.

9. Schnitzer, Peter, *Untersuchung der spektralen Eigenschaften von AlGaAs/InGaAs Halbleiternlaser mit Vertikalresonator unter externer optischer Rückwirkung*, Diploma Thesis, Dept. of Optoelectronics, University of Ulm, 1995.

10. Klauer, Detlef, *Kopplung von Laserdioden*, Diploma Thesis, Dept. of Optoelectronics, University of Ulm, 1995.

11. Morgott, Stefan, *Untersuchung von Quantenfilmstrukturen für Hochleistungslaserverstärker im Materialsystem InAlGaAs-GaAs*, Diploma Thesis, Dept. of Optoelectronics, University of Ulm, 1995.

12. Lehmann, Bernd, *Programmierung eines komputergesteuerten Meßplatzes mit mehrkanaliger Datenerfassung zur Charakterisierung von Vertikallaserdioden*, Semester Project, Dept. of Optoelectronics, University of Ulm, 1995.

13. Doser, Wolfgang, *Charakterisierung organisch-anorganischer Heterostruktur-Photodioden*, Semester Project, Dept. of Optoelectronics, University of Ulm, 1995.

14. Wiedenmann, Dieter, *Untersuchung der dynamischen Eigenschaften von Halbleiterlasern mit Vertikalresonoator*, Diploma Thesis, Dept. of Optoelectronics, University of Ulm, 1995.

    Steidle, Thomas, *Aufbau eines Meßplatzes zur Untersuchung temperaturabhängiger Größen bei Breitstreifenlaserstrukturen*, Semester Project, Dept. of Optoelectronics, University of Ulm, 1995.

15. Grabherr, Martin, *Herstellung eines Vertikallaserelementes mit Faseranschluß*, Semester Project, Dept. of Optoelectronics, University of Ulm, 1995.

16. Buck, Martin, *Entwicklung und Aufbau einer computergesteuerten Zeilenkamera*, Semester Project, Dept. of Optoelectronics, University of Ulm, 1995.

17. Schmid, Wolfgang, *Berechung und Messung der Fernfelder von oberflächenemittierenden Laserdioden*, Semester Project, Dept. of Optoelectronics, University of Ulm, 1995.

18. Joos, Jürgen, *Aufbau eines rechnergesteuerten, hochauflösenden Gitterspektrometers zur Charakterisierung von Halbleiterlaserdioden*, Semester Project, Dept. of Optoelectronics, University of Ulm, 1995.

19. Ellinger, Frank, *Untersuchung des Modenrauschens in faseroptischen Übertragungssystemen mit oberflächenemittierenden Laserdioden*, Semester Project, Dept. of Optoelectronics, University of Ulm, 1995.

20. Richter, Thomas, *Aufbau und Charakterisierung eines Einkoppelmeßplatzes für Halbleiterlaserdiodenverstärker*, Semester Project, Dept. of Optoelectronics, University of Ulm, 1995.

21. Roger, King, *Charakterisierung eines optischen Übertragungssystems mit Vertikallaserdioden*, Semester Project, Dept. of Optoelectronics, University of Ulm, 1995.

Talks, Seminars

1. B. Weigl, E. Zeeb, G. Reiner, V. Schmid, "Vertikallaserdioden mit aktiven GaAs Quantenfilmen," Würzburg, DFG-Kolloquium 95 Optische Signalverarbeitung, 6.-7. März 1995.

2. B. Weigl, "Vertikal emittierende Laser (VCSEL)," Neu-Perlach, Siemens ZFE, 20. Dez. 1995.

3. B. Weigl, "Laserdioden mit Vertikalresonator - Strukturierung und Emissionseigenschaften," Ulm, Daimler Benz Forschungszentrum F2H, 21. Dez. 1995.

4. B. Weigl, G. Reiner, M. Grabherr, K.J. Ebeling, "High-Power Selectively Oxidized Vertical-Cavity Surface-Emitting Lasers," Anaheim, California, CLEO 96, 2.-7. Juni 1995.

5. H.Y.A. Chung, D. Sowada, T. Wipiejewski, G. Stareev, K.J. Ebeling, "Wachstum und Resultate von InGaAsP-und InGaAs-Schichten mit Gas-Source MBE," Jülich, 10. Treffen des DGKK Arbeitskreises Epitaxie von III/V-Halbleitern, 7.-8. December 1995.

6. K.J. Ebeling, "Blau und grün emittierende Leuchtdioden auf der Basis von GaN," *Vertikale Laserdioden*, Temic Heilbronn, 13.2.1995.

7. K.J. Ebeling, "Vertical Cavity Surface Emitting Laser Diodes," International Symposium ,*Heterostructures in Science and Technology*, Universität Würzburg, 14.3.1995.

8. K.J. Ebeling, "Sendeelemente für die optische Verbindungstechnik: Trends und Perspektiven," *Diskussionstagung Integrierte Optik*, Fraunhofer-Einrichtung für Angewandte Optik und Feinmechanik, Jena, 18.5.1995.

9. K.J. Ebeling, "Physics of Semiconductor Lasers: Basics of Edge Emitting Laser Diodes," Les Houches Spring School *Quantum Optics of Confined Systems*, Les Houches, France, 25.5.1995.

10. K.J. Ebeling, "Physics of Semiconductor Lasers: Vertical Cavity Laser Diodes," Les Houches Spring School, *Qauntum Optics of Confined Systems*, Les Houches, France, 27.5.1995.

11. K.J. Ebeling, "Laserdioden mit Vertikalresonoator für die optische Verbindungstechnik," TU Berlin, Fachbereich Elektrotechnik, 14.6.1995.

12. K.J. Ebeling, "Vertical-cavity surface emitting laser diode arrays for efficient coupling into optical fibers," Laser 95, München 21.6.1995.

13. K.J. Ebeling, "Hardware für optische Datenautobahnen," Tag der Forschung, Universität Ulm, 7.7.1995.

14. K.J. Ebeling, "Optical Interconnects and Data Links with VCSELs," 21st European Conference on Optical Communication, ECOC'95, Brussels, 21.9.1995.

15. K.J. Ebeling, "Design and Characteristics of highly efficient InGaAs/AlGaAs vertical cavity microlasers," Italian-German Symposium on Light-Emitting Nanostructures, Menaggio, 25.9.1995.

16. K.J. Ebeling, "Optimierung von Laserdioden mit Vertikalresonator für 10 Gbit/s - Übertragung und konversionseffizienten Betrieb," Phontonik-Symposium der Volkswagen-Stiftung, Braunschweig, 6.10.1995.

17. K.J. Ebeling, "Grundlagen und Anwendungen von Laserdioden mit Vertikalresonator," Brandenburgische Technologietage, Teltow, 23.11.1995.

18. K.J. Ebeling, "Halbleiterlaser mit Vertikalresonator," Physikalisches Kolloquium, Universität Marburg, 8.12.1995.

19. K.J. Ebeling, "High performance VCSELs for optical interconnects," 13th Semiconductor Laser Symposium (International), Tokyo Institute of Technology, Yokohama, Japan, 8.3.1996.

20. K.J. Ebeling, "Progress of vertical cavity laser diodes," Special Seminar, University of Tokyo, 9.3.1996.

21. K. J. Ebeling, "Vertikalstrukturierte Halbleiterlaser höchster Effizienz," Jungius-Kolloquium, Universität Hamburg, 2.5.1996.

22. P. Unger, "Nanostrukturierung," Physikalisches Kolloquium der Universität Ulm, 30.1.1995.

23. P. Unger, "Herstellung von Halbleiter–Laserdioden," Seminar des Zentrums für Lasermeßtechnik und Diagnostik der Universität Kaiserslautern, 16.2.1995.

24. P. Unger, "Hochleistungsdiodenlaserverstärker auf der Basis von InAlGaAs / GaAs," 1. Jahrestagung für Hochleistungsdiodenlaser und diodengepumpte Festkörperlaser, Freiburg i.Br., 28.3.1995.

25. P. Unger, "Herstellung von rot emittierenden Halbleiterlaserdioden," Elektrotechnisches Kolloquium der Technischen Universität Braunschweig, 18.4.1995.

Publications and Conference Contributions

1. R. Michalzik, K.J. Ebeling, "Generalized BV Diagrams for Higher Order Transverse Modes in Planar Vertical-Cavity Laser Diodes," *IEEE J. Quant. Electron.*, vol. 31, 1371-1379, 1995.

2. K.J. Ebeling, U. Fiedler, R. Michalzik, B. Möller, K. Panzlaff, G. Reiner, B. Weigl, T. Wipiejewski, E. Zeeb, "Application of Vertical-Cavity Lasr Diodes to Optical Interconnects," in *Proc. OEC, Chiba*, Japan, pp. 284-285, 1994.

3. U. Fiedler, E. Zeeb, K. Panzlaff, C. Jung, K.J. Ebeling, "Modelocking of low threshold VCSEL with pigtailed fiber resonator," *Proc. 14th IEEE Int. Semiconductor Laser Conf.*, Maui, Hawaii, USA, pp. 115-116, Sept. 1994.

4. U. Fiedler, E. Zeeb, G. Reiner, G. Jost, K.J. Ebeling, "Feedback power penalty in 1 Gbit/s single-mode fiber transmission with butt coupled VCSEL source," *Electron. Lett.*,vol. 30, pp. 1698-1700, 1994.

5. B. Möller, E. Zeeb, T. Hackbarth, K.J. Ebeling, "Optimization of gain and mode field overlap for efficient proton implanted broad area vertical-cavity laser diodes," *Proc. 14th IEEE Int. Semiconductor Laser Conference*, Maui, Hawaii, USA, pp. 143-144, Sept. 1994.

6. E. Zeeb, B. Möller, G. Reiner, M. Ries, T. Hackbarth, K.J. Ebeling, "6 GHz modulation of fiber coupled VCSEL arrays," *Proc. 14th IEEE Int. Semiconductor Laser Conference*, Maui, Hawaii, USA, pp. 175-176, Sept. 1994.

7. G. Stareev, A. Fricke, D. Sowada, T. Kummetz, J. Mähnss, W. Kowalsky, K.J. Ebeling, "Nearly-ideal Au/Pt-n-(p+n-) Al0.48In0.52As Schottky contacts with a barrier height of 1.09 eV for high-speed photodetectors and transistors," *Proc. CLEO/Europe'94, Conference on Lasers and Electrooptics Europe*, Amsterdam, Netherlands, Aug. 1994, pp. 218-219, Aug. 1994.

8. U. Fiedler, R. Busin, P. Schnitzer, K.J. Ebeling, "Rückwirkungsuntersuchungen an Halbleiterlasern mit Vertikalresonator im AlGaAs/InGaAs Materialsystem," *VDE-ITG Fachtagung Meßverfahren der optischen Nachrichtentechnik*, März 1995, Reisensburg, März 1995.

9. U. Fiedler, C. Jung, B. Möller, G. Reiner, E. Zeeb, R. Busin, P. Schnitzer, K.J. Ebeling, "Halbleiterlaser mit Vertikalresonator für optische Kurzstreckenverbindungen," *ITG-VDE Diskussionssitzung*, Dresden, März 1995.

10. E. Zeeb, G. Reiner, M. Ries, K.J. Ebeling, "Planar Be-doped VCSELs with high wall-plug efficiencies," *Electron. Lett.*, vol. 31, pp. 1160-1611, 1995.

11. E. Zeeb, B. Möller, G. Reiner, M. Ries, T. Hackbarth, K.J. Ebeling, "Planar proton implanted VCSELs and fiber coupled 2D VCSEL arrays," *IEEE J. Selected Topics Quantum Electron.*, vol. 1, pp. 616-623, 1995.

12. U. Fiedler, K.J. Ebeling, "Design of VCSELs for feedback insensitive data transmission and external cavity active mode-locking," *IEEE Selected Topics Quantum Electron.*, vol. 1, pp. 442-450, 1995.

13. U. Fiedler, E. Zeeb, G. Reiner, K.J. Ebeling, "1 Gbit/s single-mode fiber transmission with individually addressable elements of 10 x 10 VCSEL arrays," *Proc. OFC*, San Diego, USA, pp. 105-106, 1995.

14. E. Zeeb, G. Reiner, M. Ries, B. Möller, K.J. Ebeling, "VCSELs with extremely low linewidth and linewidth-power-product," *Proc. CLEO'95*, Baltimore, MA, USA, p. 171.

15. R. Michalzik, K.J. Ebeling, "Quasi-3D modeling of vertical-cavity surface emitting laser operation," *Proc. SPIE'95, Feb. 1995*, San Jose, California, USA, Vol. 2399, pp. 360-371.

16. G. Reiner, E. Zeeb, B. Möller, M. Ries, K.J. Ebeling, "Optimization of planar Be-doped VCSELs with two-sided output," *Photon. Technol. Lett.*, vol. 7, pp. 730-732, 1995.

17. U. Fiedler, B. Möller, E. Zeeb, G. Reiner, K.J. Ebeling, "Design of Top-Emitting VCSELs for Transmission at 3 Gbit/s Data Rates," *Proc. 21st European Conference on Optical Communication ECOC'95*, Brussels, Belgium, vol. 2, pp. 871-874, Sept. 1995.

18. A.T. Meney, E.P. O'Reilly, K.J. Ebeling, "Polarisation selectivity in ordered GaInP2 vertical cavity surface-emitting lasers," *Electron. Lett.*, vol. 31, pp. 461-462, 1995.

19. K. J. Ebeling, "Physics of Semiconductor Lasers," Invited, *Proc. Summer School on Quantum Optics of Confined Systems*, Les Houches, France, May 23 - June 2, 1995, in press.

20. T. Wipiejewski, M.G. Peters, L.A. Coldren, "Vertical-Cavity Surface-Emitting Laser Diodes with Post-Growth Wavelength Adjustment," *Proc. IEEE LEOS Annual Meeting*, paper SL 5.4, Boston, MA, Nov. 1994.

21. K. J. Ebeling, B. Möller, G. Reiner, U. Fiedler, R. Michalzik, B. Weigl. C. Jung, E. Zeeb, "Vertical cavity laser diodes and arrays for efficient fiber coupling and high speed data transmission in optical interconnects," *Proc. Laser 95*, Invited, München, June 1995, in press.

22. K.J. Ebeling, "Optical Interconnects and Data Links with VCSELs," Tutorial, *Proc. 21st European Conference on Optical Communication ECOC'95*, Brussels, Belgium, vol. 4, pp. 111-146, Sept. 1995.

23. U. Fiedler, B. Möller, G. Reiner, P. Schnitzer, K.J. Ebeling, "10 Gbit/s data transmission using top emitting VCSELs with high sidemode suppression," *Electron. Lett.*, vol. 31, pp. 1664-1665, 1995.

24. B. Weigl, G. Reiner, M. Grabherr, K.J. Ebeling, "High Power Selectively Oxidized Vertical-Cavity Surface-Emitting Lasers," subm. to *CLEO'96*.

25. U. Fiedler, G. Reiner, P. Schnitzer, K.J. Ebeling, "10 Gbit/s Data Transmission with Nearly Single-Mode Top-Emitting VCSELs," *Proc. 8th Annual Meeting LEOS 1995*, Post-deadline paper PD 2.3, San Francisco, USA, 1995.

26. U. Fiedler, G. Reiner, P. Schitzer, K.J. Ebeling, "Polarzation dependent emission behavior of VCSELs at 3 Gbit/s data rate transmission," *Proc. 8th Annual Meeting LEOS*, San Francisco, USA, pp. 429-430, 1995.

27. D. Wiedenmann, B. Moeller, R. Michalzik, K.J. Ebeling, "Performance Characteristics of Vertical-Cavity Semiconductor Laser Amplifiers," submitted to *Electron. Lett.*

28. U. Fiedler, G. Reiner, P. Schnitzer, K.J. Ebeling, "Top Surface-Emitting Vertical-Cavity Laser Diodes for 10 Gbit/s Data Transmission," submitted to *IEEE Photon. Technol. Lett.*

29. M. Kamp M. Mayer, A. Pelzmann, S. Menzel, C. Kirchner, H.Y.A. Chung, H. Sternschulte, K.J. Ebeling, "Thermally cracked NH3 for MBE growth of GaN," *Proc. Topical Workshop on III-V Nitrides* Nagoya, Japan, Paper P-42, Sept. 1995.

30. D. Wiedenmann, R. Michalzik, B. Moeller, K.J. Ebeling, "Static and dynamic characteristics of vertical-cavity semiconductor laser amplifiers ," submitted to *CLEO'96*, Anaheim, California, USA.

31. Z. Dai, R. Michalzik, P.Unger, K.J. Ebeling, "Impact of the Residual Facet Reflectivity on Beam Profile Filamentation in Semiconductor Laser Amplifiers," submitted to *CLEO'96*, Anaheim, California, USA.

32. M. Kamp, M. Mayer, A. Pelzmann, S. Menzel, H.Y.A. Chung, H. Sternschulte, O. Marti, K.J. Ebeling, "NH_3 as nitrogen source in MBE growth of GaN," *Proc. Mat. Res. Soc. Meeting*, Boston, Massachusetts, USA, Nov. 1995, in press.

33. P. Michler, W.W. Rühle, G. Reiner, K.J. Ebeling, A. Moritz, "Time-bandwidth product of gain-switched In0.2Ga0.8As/GaAs microcavity lasers," *Appl. Phys. Lett.*, vol. 67, no. 1-3, 1995.

34. T. Wipiejewski, M.G. Peters, B.J. Thibeault, D.B. Young, L.A. Coldren, "Qutput Characteristics of Donut Shape Vertical-Cavity Surfache-Emitting lasers," *Proc. IEEE LEOS Annual Meeting*, paper SCL 15.3, San Jose, CA, Nov. 1995.

35. T. Wipiejweski, M.G. Peters, B.J. Thibeault, D.B. Young, L.A. Coldren, "High Power Highly Efficient Vertical-Cavity Surface-Emitting Laser Diodes with a Au-Plated Heat Spreading Layer," *Proc. OSA Topical Meeting on Semiconductor Lasers*, paper TuD5-1, Keystone, CO, Aug. 1995.

36. T. Wipiejewski, M.G. Peters, E.R. Hegblom, L.A. Coldren, "High Performance Vertical-Cavity Surface-Emitting Laser Diodes with Au-Plated Heat Spreading Layer," *Proc. 45th ECTC*, Las Vegas, NV, May 1995.

37. T. Wipiejweski, D.B. Young, M.G. Peters, B.J. Thibeault, L.A. Coldren, "Etched-Pillar Vertical-Cavity Surface-Emitting laser Diodes with Submilliamp Threshold Currents and High Output Power," *Proc. CLEO*, paper CTuB3, Baltimore, MD, May 1995.

38. T. Wipiejweski, D.B. Young, M.G. Ppeters, B.J. Thibeault, L.A. Coldren, "Improved Performance of Vertical-Cavity Surface-Emitting Laser Diodes with Au-Plated Heat Spreading Layer," *Electron. Lett.*, vol. 31, pp. 279-281, 1995.

39. U. Prank, M. Mikulla, W. Kowalsky, "Metal-Semiconductor-Metal Photodetektor with Integrated Fabry-Perot Resonator for Wavelength Demultiplexing High Bandwidth Receivers," *Appl. Phys. Lett.*, vol. 62, pp. 129-130, 1993.

40. W. Kowalsky, C. Rompf, "Crystalline Organic Semiconductors: A New Class of Materials for Photonic Devices," in: W. Ehrfeld, G. Wegner, W. Karthe, H.-D. Bauer, O. Moser (Hrsg.): *Integrated Optics and Micro-Optics with Polymers*, Teubner Texte zur Physik, Band 27, Teubner Verlag, Stuttgart, pp. 76-88.

41. W. Kowalsky, U. Prank, "Wavelength Selective Metal-Semiconductor-Metal Photodetector with Integrated Fabry-Perot Resonator for High Bandwidth Receivers," *Jap. J. Appl. Phys.*, vol. 32, pp. 574-577, 1993.

42. W. Kowalsky, U. Prank, "Planar MSM-Modulators and Photodetectors with Integrated Fabry-Perot Resonator for Arrayed Configurations in High-Bandwidth Optical Interconnects," *SPIE's Int. Symp. on Optoelectronic Packaging and Interconnects* (Vol. 1849: Optoelectronic Interconnects), Los Angeles, USA, pp. 252-259, 1993.

43. M. Sickmöller, P. Urbach, W. Kowalsky, "Optimization of MSM-Photodetectors: Characterization of Carrier Transport by Correlation Technique," *19th European Conference on Optical Communication*, Vol. 2 (Regular Papers), Montreux, Schweiz, pp. 273-276, 1993.

44. C. Rompf, B. Hilmer, W. Kowalsky, "Organic-on-Inorganic Semiconductor Heterostructures: Photonic Devices and Application to OEICs," *19th European Conference on Optical Communication*, Vol. 2 (Regular Papers), Montreux, Schweiz, pp. 341-344, 1993.

45. W. Kowalsky, M. Sickmöller, P. Urbach, "Charakterization of Dynamic Behaviour of MSM-Photodetectors by Correlation Technique," *1993 Int. Conf. on Solid State Devices and Materials*, Chiba, Japan, pp. 663-665, 1993.

46. W. Kowalsky, C. Rompf, B. Hilmer, "Heterostructures of Crystalline Organic and Inorganic Semiconductors and Applications in OEICs," *1993 Int. Conf. on Solid State Devices and Materials*, Chiba, Japan, pp. 1053-1055, 1993.

47. W. Kowalsky, C. Rompf, B. Hilmer, "Integrated Optoelectronic Heterostructure Devices Composed of Crystalline Organic and Inorganic Semiconductors," *ACS/OSA Topical Meeting: Organic Thin Films for Photonic Applications*, Toronto, Kanada, pp. 310-313.

48. M. Sickmöller, P. Urbach, W. Kowalsky, "Characterization of Dynamic Behaviour of Metal-Semicooductor-Metal Photodetectors by Correlation Technique," *Jpn.J. Appl. Phys.*, vol. 33, pp. 844-847, 1994.

49. C. Rompf, B. Hilmer, W. Kowalsky, "Heterostructures of Crystalline Organic and Inorganic Semiconductors for Applications in Optoelectronic Integrated Circuits," *Jpn.J. Appl. Phys.*, vol. 33, pp. 832-835, 1994.

50. D. Ammermann, C. Rompf, W. Kowalsky "A Novel Concept for Optical Interconnects Based on Organic Semiconductors and Heterostructures" (eingeladener Vortrag), *European Conference on Lasers and Electro-Optics/European Quantum Electronics Conference*, Amsterdam, Niederlande, p.33, 1994.

51. M. Sickmöller, W. Kowalsky, "On the Influence on Material Properties on High Speed Behavior of Metal-Semiconductor-Metal Photodetectors," *European Conference on Lasers and Electro-Optics/European Quantum Electronic Conference*, Amsterdam, Niederlande, pp. 89-90, 1994.

52. T. Kummetz, A. Fricke, D. Sowada, J. Mähnß, W. Kowalsky, "AlGaInAs Metal-Semiconductor-Metal Photodetectors and Modulators for GBit/s Systems," *European Conference on Lasers and Electro-Optics/European Quantum Electronics Conference*, Amsterdam, Niederlande, p. 163, 1994.

53. G. Stareev, A. Fricke, D. Sowada, T. Kummetz, J. Mähnß, W. Kowalsky, K. J. Ebeling, "Nearly-Ideal Au/Pt-n-(p+n) Al0.48In0.52As Schottky Contacts with a Barrier Height of 1.09eV for High Speed Photodetectors and Transistors," *European Conference on Lasers and Electro-Optics/European Quantum Electronics Conference*, Amsterdam, Niederlande, pp. 218-219, 1994.

54. W. Kowalsky, C. Rompf, D. Ammermann, "Photonic Devices Based on Crystalline Organic Semiconductors for Optoelektronic Integrated Circuits," *1994 Int. Conf. on Solid State Devices ans Materials*, Yokohama, Japan, pp. 145-147, 1994.

55. W. Kowalsky, M. Sickmöller, "Material Characterization and Optimization for Ultra High Speed MSM-Photodetectors," *1994 Int. Conf. on Solid State Devices and Materials*, Yokohama, Japan, pp. 235-237, 1994.

56. T. Kummetz, M. Sickmöller, A. Fricke, D. Sowada, J. Mähnß, W. Kowalsky, "MSM-Photodetectors and -Modulators for Long Wavelength Applications: Optimization of Solid Source MBE Growth of AlInAs/(AI)GaInAs-Heterostructures," *1994 Int. Conf. on Solid State Devices and Materials*, Yokohama, Japan, pp. 232-234, 1994.

57. C. Rompf, D. Ammermann, W. Kowalsky, "Crystalline Organic Semiconductors for Photonic Applications in Optical Interconnects," *20th European Conference on Optical Communication*, Florenz, Italien, pp. 201-204, 1994.

58. T. Kummetz, M. Sickmöller, A. Fricke, D. Sowada, J. Mähnß und W. Kowalsky, "Optimization of AlInAs/AlGaInAs Heterostructures for Low Noise Metal-Semiconductor-Metal Photodetectors and Electooptical Switches," *20th European Conference on Optical Communication*, Florenz, Italien, pp. 387-390, 1994.

59. D. Ammermann, C. Rompf, W. Kowalsky, "Deposition and Charaterization of Crystalline Organic Semiconductors for Photonic and Electronic Devices," *1st Int. Conf. on Materials for Microelectronics*, Barcelona, Spanien, pp. 208-209, 1994.

60. T. Kummetz, M. Sickmöller, A. Fricke, D. Sowada, J. Mähnß und W. Kowalsky, "Influence of AlInAs Schotty Barrier Enhancement Layer Thickness on AlInAs/GaInAs Metal-Semiconductor Metal Photodetectors in the Time and in the Freyuency Domain," *1st Int. Conf. on Materials for Microelectronics*, Barcelona, Spanien, pp. 89-90, 1994.

61. T. Kummetz, K. Panzlaff, D. Sowada, J. Mähnß, K. J. Ebeling und W. Kowalsky, "AlGaInAs/InP Photodetectors and Electrooptical Modulators for Applications in OEICs and Optical Interconnects," *IEEE J. Lightwave Technol.*, in press.

62. A. Fricke, G. Stareev, T. Kummetz, D. Sowada, J. Mähnß, W. Kowalsky, K. J. Ebeling, "1.09 eV Schottky Barrier Height of Nearly-Ideal Pt/Au Contacts Directly Deposited on n- and p+n-Al0.48In0.52As Layers," *Appl. Phys. Lett.*, vol. 65, pp. 755-757, 1994.

63. T. Kummetz, S. Dirr, M. Sickmöller, A. Herrmann, W. Kowalsky, "Metal Semiconductor Metal Photodetectors for Long Wavelength Applications: Optimization of Solid Source Molecular Beam Epitaxy of AlInAs/(Al)GaInAs-Heterostructures," *Jpn. J. Appl. Phys.*, vol. 34, pp. 1303-1308, 1995.

64. D. Ammermann, C. Rompf, W. Kowalsky, "Photonic Devices Based on Crystalline Organic Semiconductors for Optoelectronic Integrated Circuits," *Jpn. J. Appl. Phys.*, vol. 34, pp. 1293-1297, 1995.

65. C. Rompf, D. Ammermann, A. Böhler, W. Kowalsky, "Growth and Characterization of Organic Semiconductor Devices: Photodetectors and Light Emitting Diodes (OLED)," *Int. Conf. on Solid State Devices and Materials*, Osaka, Japan, pp. 455-457, 1995.

66. P. Urbach, C. Rompf, D. Ammermann, W. Kowlaksy, "Optimization of Current-Voltage Characteristics of Organic-on-Inorganic Heterostructure Diodes," *Int. Conf. on Solid State Devices and Materials*, Osaka, Japan, pp. 401-403, 1995.

67. D. Ammermann, A. Böhler, C. Rompf, W. Kowalsky, "Characterization and Optimization of High Brightness Organic Light Emitting Diodes (OLEDs)," *IEEE/LEOS Summer Topical Meeting on Flat Panel Display Technology*, Keystone, Colorado, USA, pp. 31-32, 1995.

68. D. Ammermann, A. Böhler, C. Rompf, W. Kowalsky, "Double Heterostructure and Multiple Quantum Well Organic Light Emitting Diodes for Flat Panel Displays," *Proc. OSA/ACS Topical Meeting on Organic Thin Films for Photonic Applications*, Portland, USA, pp. 221-224, 1995.

69. C. Rompf, D. Ammermann, W. Kowalsky, "Deposition and Characterization of Crystalline Organic Semiconductors for Photonic Devices," *Materials Science and Technology*, vol. 11, pp. 845-848, 1995.

70. K.J. Ebeling, "Integrated Optoelectronics," *Springer-Verlag*, 540 pages, Berlin 1993.

71. W. Kowalsky, "Dielektrische Werkstoffe der Elektronik und Photonik," *Teubner-Verlag*, Stuttgart 1994.

72. M. Kamp, G. Mörsch, V.Frese, H.Lüth, "TMGa / TEGa interactions in metalorganic molecular beam epitaxy," *Appl. Phys. Lett.*, vol. 66, no. 3, pp. 367-369, 1995.

73. L.R. Brovelli, I.D. Jung, D. Kopf, M. Kamp, M. Moser, F.X. Kärtner, U.Keller, "Self starting soliton modelocked Ti:Sapphire laser using a thin semiconductor saturable absorber," *Electronic Lett.*, vol. 31, pp. 287-289, 1995.

74. F.X. Kärtner, L.R. Brovelli, D. Kopf, M. Kamp, I. Calasso, U.Keller, "Control of solid state laser dymanics by semiconductor devices," *Optical Engineering*, vol. 34, no. 7, pp.2024-2036, 1995.

75. I.D. Jung, F.X. Kärtner, L.R. Brovelli, M. Kamp, U.Keller, "em Experimental verification of soliton mode locking using only a slow saturable absorber," *Optical Letters*, vol. 20, no. 18, pp. 1892-1894, 1995.

76. S. Strite, M. Kamp, H.P. Meier, "Reliable substrate temperature measurements for high temperature AlGaAs molecular-beam epitaxy growth," *J. Vac. Sci. Technol.*, B 13, no. 2, pp. 290-292, 1995.

77. D. Kopf, K.J. Weingarten, L.R. Brovelli, M. Kamp, U.Keller, "Sub-50-fs diode pumped mode-locked Cr:LiSAF with an A-FPSA", *International Conference on Lasers, Electro-Optics, CLEO 1995*, Baltimore USA, paper CWM2, 1995.

78. I.D. Jung, L.R. Brovelli, M. Kamp, U.Keller, M.Moser, "Scaling of the A-FPSA design toward a thin saturable absorber", *Optics Letters*, vol.20, pp.1559-1561, 1995.

79. I.D. Jung, F.X. Kärtner, L.R. Brovelli, M. Kamp, M.Moser, U.Keller, "Self-starting sub-20 fs passively modelocked Ti:sapphire laser using an A-FPSA", *International Conference on Lasers and Electro-Optics, CLEO 1995*, Baltimore USA, 1995.

80. F.X. Kärtner, I.D. Jung, D. Kopf, L.R. Brovelli, M. Kamp, U. Keller, M. Moser, "Soliton modelocking with slow saturable absorbers and its implications for ultrashort pulse generation," *OSA Annual Meeting 1995*, Portland, Oregon USA, paper MMM3, 1995.

81. Z. Dai, R. Michalzik, P. Unger, K. J. Ebeling, "Operating Characteristics simulation of high-power broad stripe quantum well semiconductor traveling wave amplifiers," *OSA Technical Digest Series*, pp. 95-97, 1995.

82. Z. Dai, R. Michalzik, P. Unger, K. J. Ebeling, "Influences of gain coefficient nonlinearity on the operating characteristics of semiconductor traveling wave amplifiers," *IEEE Lasers and Electro-Optics Society 1995 Annual Meeting*, pp. 299-300, 1995.

83. Z. Dai, R. Michalzik, P. Unger, K.J. Ebeling, "Modeling of high-power semiconductor laser amplifiers with residual reflectivity," accepted by *Progress in Electromagnetics Research Symposium*, Innsbruck, Austria, 1996.

84. Z. Dai, P. Unger, "Beam profile filamentation in high power semiconductor amplifiers," submitted to *Conference on Laser and Electro-Optics/Europe 1996*, 1996.

85. Z. Dai, P. Unger, K.J. Ebeling, "Thermal analysis of high power InAlGaAs/GaAs Lasers," submitted to *1996 international conference on simulation of semiconductor processes and devices*, 1996.

86. P. Michler, A. Lohner, G. Reiner, W.W. Rühle, "Transient pulse response of $In_{0.2}Ga_{0.8}As$/GaAs microcavity lasers," *Appl. Phys. Lett.*, vol. 66, no. 13, pp 1599-1601, March 1995.

87. G. Reiner, E. Zeeb, K.J. Ebeling, "High performance top surface-emitting vertical-cavity laser diodes," *Proceedings ESSDERC '95*, pp. 451-454, September 1995.

88. P. Michler, A. Lohner, G. Reiner, W.W. Rühle, "Transient pulse response of $In_{0.2}Ga_{0.8}As$/GaAs microcavity lasers," *Technical Digest QELS '95*, May 1995.